Effect of Photoacoustic Radar Chirp Parameters on Profilometric Information

A thesis submitted to
the Faculty of Engineering
in partial fulfillment of the requirements for the
degree of Master of Applied Science in
Mechanical Engineering

by

Zuwen Sun

Ottawa-Carleton Institute for Mechanical and Aerospace Engineering
University of Ottawa
Ottawa, Ontario, Canada, K1N 6N5
January 2018

Abstract

Photoacoustic imaging for biomedical application has attracted much research in recent years. To date, most of the work has focused on pulsed photoacoustics. Recent developments have seen the implementation of a radar pulse compression methodology into continuous wave photoacoustic modality, however very little theory has been developed in support of this approach. In this thesis, the one-dimensional theory of radar photoacoustics for pulse compressed linear frequency modulated continuous sinusoidal laser photoacoustics is developed. The effect of the chirp parameters on the corresponding photoacoustic signal is investigated, and guidelines for choosing the chirp parameters for absorber profilometric detection are given based on the developed theory and simulations. Simulated results are also compared to available experimental results and show a good agreement.

Key words: Photoacoustic, Pulse compression, Autocorrelation, photoacoustic radar.

Acknowledgements

My deep appreciation is presented to Dr. Natalie Baddour, who is my supervisor, for her patient help and professional advice during my study, as well as her financial support which made my life in Canada easier. I would also like to appreciate Dr. Liang Ming, who first gave me the opportunity to study at the University of Ottawa. At last, my grateful thanks to my parents, parents in law, and my uncle and aunt for their endless help and support.

Table of Contents

List of Figures

Nomenclature

l Thickness of absorber.

c_s Speed of sound.

a Light decay factor.

μ_a Absorber optical absorption coefficient.

β Absorber thermo-expansion coefficient.

p_0 Initial pressure of acoustic wave.

T Input waveform duration.

Δ Chirp bandwidth.

f_0 Chirp center frequency.

$I(t)$ Input waveform in time domain.

$\tilde{I}(\omega)$ Input waveform in frequency domain.

$r(t)$ Receiver-filter impulse response in time domain.

$\tilde{R}(\omega)$ Receiver-filter transfer function in frequency domain.

$g(z,\mathrm{t})$ Absorber impulse response in time domain.

$\tilde{G}(z,\omega)$ Absorber transfer function in frequency domain.

$R_{ff}(t)$ Autocorrelation of a function $f(t)$

$S_{ff}(\omega)$ Energy spectral density of a signal.

$p(z,t)$ Pressure response.

$n(t)$ Noise.

$A(z)$ Absorber shape in space.

$\hat{A}(\omega_z)$ Spatial Fourier transform of $A(z)$

$Q(t)$ Integral of $I(t)$, $Q(t)=\int_{-\infty}^{t} I(\tau)\,d\tau$.

$R_{II}(t)$ Envelope of the autocorrelation of a finite-duration chirp.

$R_{II}^{approx}(t)$ Approximation of $R_{II}(t)$.

$R_{II\_\cos}(t)$ Autocorrelated cosine chirp waveform.

$R_{II\_\cos}^{approx}(t)$ Approximation of $R_{II\_\cos}(t)$

1 Introduction

1.1 Background: Introduction to Photoacoustic Imaging

Photoacoustic phenomenon (also called optoacoustic phenomenon) was discovered more than a century ago [1]. However, the application of this phenomenon to biomedical imaging started only around several decades ago [2], [3]. Presently, the intended purpose of using this imaging method in biomedical engineering is mainly for early cancer detection.

X-ray radiography (mammography), magnetic resonance imaging (MRI), and ultrasound are the three prevailing imaging techniques that are currently available for breast cancer detection. All these techniques have their own advantages of detecting cancers, but they also have limitations.

The main advantage of photoacoustic imaging (also called photoacoustic tomography, PAT) is that it combines the advantages of both optical and acoustical methods: sensitive optical absorption contrast and low acoustic scattering in soft tissue. Using safe illumination sources, the photoacoustic effect can be applied to biological tissues. In addition, optical absorption is highly related to molecular constitution and formation. Thus, photoacoustic signals contain functional and molecular information [4].

The governing physical principles behind PAT are straight forward.

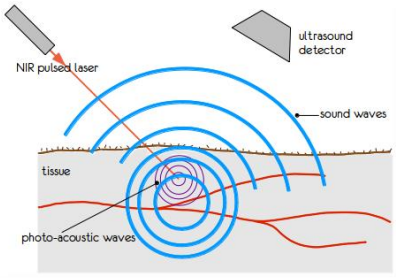

Figure 1 Photoacoustic tomography

As shown in Figure 1, the absorbing material is irradiated by a modulated electromagnetic wave. Some of the energy of the incident wave will be absorbed by the absorber which then causes a heating effect. In turn, this heating will cause a thermoelastic expansion which leads to the generation of an ultrasonic wave. The ultrasonic wave is then detected by a transducer and analyzed by different signal processing methods. Since the ultrasonic wave is generated because of the absorption of the incident electromagnetic wave, the PAT methodology is actually detecting differences between tissue absorption coefficients. The time delayed profile of the ultrasonic wave detected by the transducer thus carries tissue absorption coefficient profilometric information. As there is a large difference in optical absorption between blood and surrounding tissue, the ultrasound wave induced by the electromagnetic irradiation carries information about the optical absorption property of the tissue and can be used for imaging of the microvascular system or tissue characterization.

There are presently two different approaches of excitation, or in other words, two different light sources that can be sent to the target tissue. The most common excitation source used in past decades has been a pulsed laser source, which utilizes an extremely short duration and high intensity laser pulse as the excitation source. The other source that has also recently attracted researchers' attention is a longer duration continuous wave laser beam that has a lower intensity.

1.2 Motivation

Much research has been done to advance the science of photoacoustic imaging. However, most of the work to date has focused on pulsed laser excitation. This approach uses powerful nanosecond electromagnetic wave pulses to generate the acoustic transients, as seen in the work of Kruger [5], [6] and Wang [7]–[9]. This modality allows one to find the distribution of heat sources directly from the shape of the photoacoustic signal [10]. However, the pulsed laser modality has disadvantages

mainly due to the hard-to-control depth localization of the absorber, as well as the fact that the incident energy level is limited by safety standards for in-vivo tissue imaging [11]. Furthermore, the laser source in this modality is expensive and larger in size compared to a continuous wave diode laser source. An alternative excitation source must be developed in order to avoid the disadvantages of pulsed laser photoacoustics.

The alternative continuous wave excitation modality which has recently attracted researchers' attention uses a linear frequency modulated sinusoidal laser waveform rather than a simple short pulse. The intensity of the incident laser beam is modulated into a linearly modulated sinusoidal wave form and pulse compression techniques from radar are implemented. This kind of incident waveform is usually referred to as a "Chirp" in traditional radar technology. Mandelis and his team originally developed this modality [11], [13]–[18], which they refer to as photoacoustic radar. The idea is that pulse compression techniques are implemented in the imaging modality in order to achieve a better signal to noise ratio (SNR) and better resolution [18]. However, the effects of the laser chirp parameters on the corresponding PA signal are still not well understood. The received signal does not appear to carry sufficient absorber profilometric information. In order to obtain acceptable absorber profilometric information, a theory of photoacoustic radar needs to be developed and the effect of the parameters of the chirp on the resulting photoacoustic signal needs to be investigated.

1.3 Objectives

The goal of this thesis is to develop a one-dimensional theory of linear frequency modulated sinusoidal laser chirp photoacoustic imaging, and to investigate the chirp parameters' effects on corresponding photoacoustic signals through simulation. Subsequently, the goal is to develop guidelines for choosing the chirp parameters to obtain a photoacoustic signal which carries acceptable absorber profilometric

information. The effect of the chirp parameters on the photoacoustic signal to noise ratio is also investigated.

In this thesis, the photoacoustic radar theory will be developed in one dimension. The model representing the absorbing and surrounding tissue will be considered as a three layer model as shown in Figure 2.

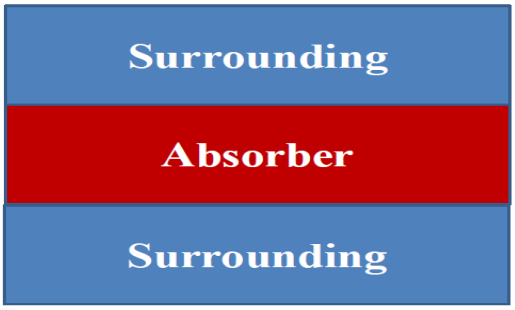

Figure 2 Absorbing system model

Two different absorber profiles will be considered. The first one is where the absorber is modelled as a square function in space, which implies that the intensity of the incident laser light does not decay as it passes through the absorber. The second case considered is where the laser intensity will decay in the absorber and the decay is modelled as being exponential. The mathematical expressions of the photoacoustic signals will be developed for these two different cases and then simulated with symbolic computer algebra software (Maple). Subsequently, the effect of the different chirp parameters will be investigated via simulation.

1.4 Contributions of the thesis

The contributions of this thesis are shown as follows:

1. Two different absorber profiles have been proposed and their corresponding mathematical models have been developed in closed form.

2. Mathematical expressions of the pulse-compressed photoacoustic signal response of two different types of absorber under illumination by a linear frequency modulated laser chirp have been developed.

3. Mathematical expressions of the Signal-to-Noise Ratio (SNR) for a bandlimited absorber and square absorber have been developed.

4. The effect of the chirp parameters on the corresponding photoacoustic signals are investigated.

5. Guidelines on how to choose the parameters of the chirp in order to obtain a photoacoustic signal with acceptable absorber profilometric information are proposed.

6. The effect of the different chirp parameters on the photoacoustic SNR is determined through development of closed-form expressions and simulations.

7. Simulations are performed using the chirp parameters used in available experimental results [19], and compared with the experimental results. The comparison shows that the guidelines developed in this thesis for choosing chirp parameters predict a similar result to that obtained in the experiments.

1.5 Outline of the thesis

The thesis is organized as follows. Chapter 2 presents the literature review, which gives an overview of historical and current research. In Chapter 3, closed-form photoacoustic signal responses for a square absorber and exponential decay absorber are developed and illustrated. In Chapter 4, the closed form expressions of SNR for bandlimited and square absorbers are developed and investigated. Several simulations

are performed in Chapter 5 to illustrate the chirp parameters' effects on the photoacoustic signal, and guidelines on how to choose the parameters to receive acceptable absorber profilometric information are presented. In Chapter 6, a comparison between the simulations with parameters used in experimental results and the obtained experimental results carried out. Conclusions are drawn in Chapter 6, in which future research directions are also suggested.

2 Literature Review

2.1 A Brief History of Photoacoustics

In 1880, Alexander Graham Bell and Sumner Tainter first reported the photoacoustic phenomenon [20]. A year later, Bell found that sonorousness, under the influence of intermittent light, is a property common to all matter [1]. However, interest in the photoacoustic field did not last long. Interest was revived later in 1938 when Veingerov followed by Pfund and Luft used the photoacoustic effect for nondispersive infrared gas analysis [21]. In 1970, Kreuzer first introduced the laser-excited photoacoustic effect when analyzing gas concentrations [22]. The utilization of a laser as the light source increased the sensitivity by several orders of magnitude. In 1975, the photoacoustic effect was first introduced in the biomedical field by Maugh [23].

2.2 Breast Cancer Detection Methods

X-ray radiography (mammography), magnetic resonance imaging (MRI), and ultrasound are the three commonly used imaging techniques for breast cancer detection [2]. All these techniques have their own advantages but also limitations.

The main limitation of X-ray mammography is its incapability to detect lesions in radiologically dense breast. The minimal size of tumors detectable by mammography is about 5-10 mm if a tumor does not contain calcification [24]. Another disadvantage of X-ray mammography is it utilizes harmful ionizing radiation.

MRI is known for its good resolution. However, the sensitivity of MRI in many instances is not very good, and this technology is also very expensive [25].

Ultrasound is another modality that has been used for imaging and for detection of

tumors. The main advantage of ultrasound is that it provides a good resolution and larger depth penetration. However, ultrasound imaging is incapable of producing high contrast image [26]. The detection of tumors in many cases is difficult because of the low contrast in acoustic properties between the tumors and normal tissues.

Photoacoustic imaging combines the advantages of the optical and acoustical imaging methods. It has the advantage of both sensitive optical absorption contrast [27] and low acoustic scattering in soft tissue [26]. Using safe non-ionizing illumination sources, the photoacoustic effect can be applied to biological tissues. In addition, optical absorption is highly related to molecular constitution and formation. Thus, photoacoustic signals contain functional and molecular information [4].

Photoacoustic imaging has drawn attention during the past several decades. Much progress in many different techniques has been made to apply the photoacoustic phenomenon to imaging application [2], [3], [14], [15], [17]. One way to categorize the different techniques is by their excitation sources. The two most general categories of photoacoustics use pulsed laser excitation sources and continuous wave laser excitation sources.

2.3 Pulsed Laser Excitation Photoacoustics

The most common excitation source for photoacoustic applications has been a pulsed electromagnetic wave. This method uses powerful nanosecond electromagnetic wave pulses to generate the acoustic transients. Kruger [5], [6], Wang [4], [7], [9], [29]–[33] worked in the pulsed laser excitation modality. The excitation waves most commonly used are radio frequency electromagnetic wave pulses, microwave pulses and infra-red laser pulses.

The main reason for using pulsed laser light is that it allows one to find the

distribution of heat sources directly from the shape of the photoacoustic signal [10]. However, the pulsed laser modality has disadvantages mainly due to the hard-to-control depth localization of the absorber, as well as the limitations on the incident energy level because of safety standards for in-vivo tissue imaging [11]. A pulse with extremely high intensity cannot be used as it may cause damage to the tissue.

Much progress has been made in trying to find other methods that do not need the high intensity laser pulse but also do not lose the high signal amplitude generated by a high intensity pulse. Liu et al. [28] found that instead of using one single high intensity short pulse, using multiple low-energy picoseconds pulses excitation may solve this problem. They also found the signal to noise ratio increased when the number of pulses increased.

From one single high intensity pulse to multiple low intensity pulses was an improvement in the approach. This suggested another approach, what if many more pulses with lower energy in the same time interval were added, until they became a continuous wave?

2.4 Continuous Wave Laser Excitation Photoacoustics

The above leads to the alternative excitation modality, continuous wave laser excitation. Much research has been done to apply a continuous wave to photoacoustic tomography [13], [15], [17]–[19]. This modality commonly uses a continuous laser wave instead of short duration pulses as the incident light source.

Continuous wave photoacoustics was first introduced by Mandelis' research group using a frequency sweep (chirp) laser source with heterodyne modulation [11], [17]. The results showed this method can be more precisely controlled in depth imaging

comparing to pulsed laser modality. However, the photoacoustic signal peak is broadened due to the extended exposure time. Therefore, the major merit of pulsed laser modality, which allows one to find the distribution of heat sources directly from the shape of the photoacoustic signal, is gone.

Another signal processing method is matched-filtering. The received photoacoustic signal is cross-correlated with a modulated incident wave form by the matched-filter. The merits of using a matched-filter are detailed in many radar or signal processing books [33], [34].

2.5 Pulse Compression

The main reason that linear frequency modulated sinusoidal chirps are used with a matched-filter is the pulse compression phenomenon, which is commonly used in traditional radar techniques [24], [33], [35], [36]. The matched filter was shown to be the complex conjugate of the transmitted signal [24], [37]. When a received photoacoustic signal is cross-correlated with a transmitted wave form, the energy of the output signal will be concentrated in a much narrower time interval (the signal has been compressed) [35], [36].

Telenkov, Lashkari and Mandelis performed many investigations on continuous wave photoacoustic radar [12]–[16], [19], [38], [39], which they refer to as Frequency Domain Photoacoustics (FD-PA). The first attempt at using cross-correlation signal processing method in FD-PA was introduced in 2006 [40]. In this study, the algorithm of FD-PA was introduced and an experimental device was built. Testing results for turbid phantoms and ex-vivo chicken breast specimens showed clear peaks which carries the inhomogeneity (absorber) information.

Further study [41] showed that although acoustic pressure waves induced by an

intensity modulated continuous wave laser have much lower amplitude than those generated by high peak-power nanosecond pulses, the signal to noise ratio (SNR) can be increased dramatically via specific modulation coding and coherent signal processing. A year later, investigation on SNR, axial resolution and detection depth was performed [12], [18]. The experimental results showed FD-PA can provide comparable or better depth sensitivity with millimeter-scale axial resolution due to superior SNR. These features imply that FD-PA is a competitive imaging method comparing to pulsed photoacoustic technique [12], [18].

Lashkari and Mandelis' further research on FD-PA gives detailed theoretical and experimental comparison between various key parameters of the pulsed photoacoustic modality and FD-PA imaging modality. The experimental results showed much smaller SNR difference between pulsed and FD photoacoustics [15]. The results also showed that increasing the chirp frequency bandwidth drastically reduces the SNR [15]. Hence, it was attempted to find the optimal chirp bandwidth which generates the best SNR [14]. It was shown that the optimal bandwidth generating the highest SNR for a low-frequency transducer is roughly centered at the peak frequency of the transducer, and for high-frequency transducer, the optimal bandwidth is centered on the lower frequencies [14]. However, the theory behind the SNR optimization is still not clear. Further study on the theory of FD-PA showed a more detailed view of chirp parameters' effects on SNR [38]. The results explained that the SNR of the filtered photoacoustic signal is proportional to the chirp duration. However, chirp duration is not the only parameter that controls SNR. Further study needs to be done in order to fully understand the controlling chirp parameters on SNR.

Furthermore, the experimental photoacoustic signal generated by linear frequency modulated chirp after cross-correlation signal processing [13], [19], [40], [41] did not give as much absorber profilometric information as obtained with the pulsed laser photoacoustic technique. This leads to the main motivation of this work, which is to reconstruct the approach for continuous wave linear frequency modulated laser

photoacoustics and to give guidelines on how to choose the parameters of the chirp to obtain sufficient absorber depth profilometric information and optimal SNR.

3 Photoacoustic Pressure Response

As discussed earlier, matched-filtering is implemented in continuous wave photoacoustic tomography. A linear frequency modulated sinusoidal waveform commonly used in radar technique has a property of pulse compression after matched-filtering. However, the theory behind this technology in photoacoustics is still not clear. In this chapter, the 1-D theory for two specific absorber models and their corresponding photoacoustic signal after receiver-filter are developed. The incident laser waveform is limited to be a linear frequency modulated cosine chirp. The absorber models considered are a square absorber and an exponential decay absorber which will be explained in detail later.

3.1 Fourier Transform and Autocorrelation Conventions

Fourier transform and autocorrelation have several different conventions which can be found in many sources [33], [42], [43]. In this thesis, the chosen convention for the temporal Fourier transform is the angular frequency, non-unitary convention for forward and inverse transforms given by

$$\tilde{f}(\omega) = \int_{-\infty}^{\infty} f(t) e^{-i\omega t} dt \quad \Leftrightarrow \quad f(t) = \frac{1}{2\pi} \int_{-\infty}^{\infty} \tilde{f}(\omega) e^{i\omega t} d\omega \tag{3.1}$$

where a tilde (~) over the variable has been used to denote a temporal Fourier transform, and assuming suitability of the function *f* for Fourier transformation. The spatial Fourier transform from regular space with spatial variable z to spatial frequency space with spatial frequency variables ω_z is defined as in (3.1), with z replacing t and ω_z replacing ω in (3.1). The spatial Fourier transform is denoted with an over hat over the variable, so that $f(z) \Leftrightarrow \hat{f}(\omega_z)$ denotes a Fourier transform pair with respect to the spatial variable.

The energy of a signal is defined as [42]

$$E_f = \int_{-\infty}^{\infty} \left| f(t) \right|^2 dt = \frac{1}{2\pi} \int_{-\infty}^{\infty} \left| \tilde{f}(\omega) \right|^2 d\omega \tag{3.2}$$

where the last equality in equation (3.2) follows from Parseval's theorem [33]. Since the integral on the right-hand side is the energy of the signal, the integrand $\left| \tilde{f}(\omega) \right|^2$ can be interpreted as an energy density function [44] describing the energy per unit frequency contained in the signal at frequency ω. In light of this, the energy spectral density of a signal $f(t)$ is defined as

$$S_{ff}(\omega) = \left| \tilde{f}(\omega) \right|^2 = \tilde{f}(\omega)\overline{\tilde{f}(\omega)} = \left| \int_{-\infty}^{\infty} f(t) e^{-i\omega t} dt \right|^2 \tag{3.3}$$

where the overbar indicates a complex conjugate. The energy spectral density is most suitable for transients—that is, pulse-like signals—having a finite total energy. Now consider the inverse Fourier transform of the energy spectral density:

$$\begin{aligned} \frac{1}{2\pi} \int_{-\infty}^{\infty} S_{ff}(\omega) e^{i\omega t} d\omega &= \frac{1}{2\pi} \int_{-\infty}^{\infty} \int_{-\infty}^{\infty} f(\tau) e^{-i\omega\tau} d\tau \int_{-\infty}^{\infty} \overline{f(\tau')} e^{+i\omega\tau'} d\tau' \, e^{i\omega t} d\omega \\ &= \int_{-\infty}^{\infty} \int_{-\infty}^{\infty} f(\tau)\overline{f(\tau')} \underbrace{\frac{1}{2\pi} \int_{-\infty}^{\infty} e^{+i\omega\tau'} e^{i\omega t} e^{-i\omega\tau} d\omega}_{=\delta(t+\tau'-\tau)} d\tau d\tau' \end{aligned} \tag{3.4}$$

Changing the order of integration as shown in (3.4) and using the definition of the inverse Fourier transform of the delta function gives

$$\begin{aligned} \frac{1}{2\pi} \int_{-\infty}^{\infty} S_{ff}(\omega) e^{i\omega t} d\omega &= \int_{-\infty}^{\infty} \int_{-\infty}^{\infty} f(\tau)\overline{f(\tau')}\, \delta(t+\tau'-\tau)\, d\tau d\tau' \\ &= \int_{-\infty}^{\infty} f(t+\tau')\overline{f(\tau')}\, d\tau' \end{aligned} \tag{3.5}$$

The last integral in equation (3.5) is exactly the auto-correlation of the function $f(t)$, traditionally defined as

$$R_{ff}(t) = \int_{-\infty}^{\infty} f(t+\tau')\overline{f(\tau')}\, d\tau' \tag{3.6}$$

Hence, it follows that the autocorrelation of a function and its energy spectral density are a Fourier transform pair $R_{ff}(t) \Leftrightarrow S_{ff}(\omega)$.

The autocorrelation of a periodic function $f(t)$ is defined as an average power over one waveform as

$$R_{ff}(t)=\frac{1}{T}\int_{t_0}^{t_0+T}\overline{f(\tau)}f(t+\tau)d\tau, \tag{3.7}$$

where t_0 is any arbitrary value, and T is the period of the function.

3.2 System Layout

For a one-dimensional system, the absorbing material surrounded with the scattering medium is considered to have the simple layout shown in Figure 3.

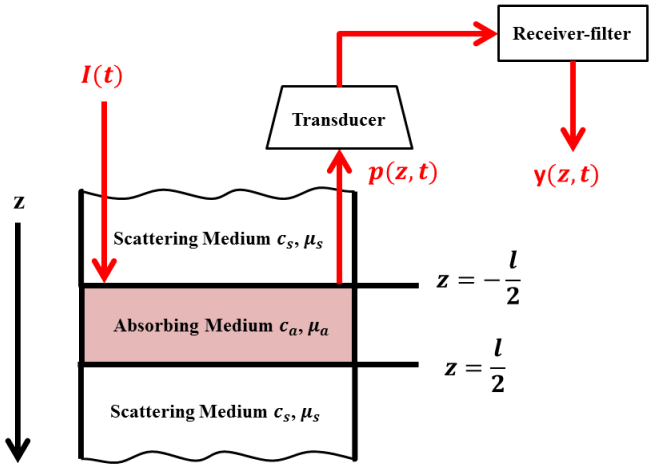

Figure 3 Model of absorber and surroundings

In Figure 3, the origin of the *z*-axis is placed at the center of absorber. The absorber is considered as an infinite sheet with a thickness l. The surrounding scattering medium on negative side of z axis is considered as an infinite layer from $-\infty$ to $-\frac{l}{2}$. The surrounding scattering medium on positive side of z axis is considered as an infinite

layer from $\frac{l}{2}$ to ∞.The speeds of sound c_s is considered to be the same in all three layers. C_p is the specific heat, μ_a is the optical absorption coefficient of the chromophore absorber that has been heated by an optical pulse with fluence *F*. The incident laser waveform $I(t)$ is transmitted from the negative side of *z* axis, outside of the absorber. The absorber absorbs energy from the incident laser and generates a sound wave (or in other words, pressure response) denoted by $p(z,t)$. The pressure response is then detected by a transducer and be sent to a receiver-filter. The output of the receiver-filter $y(z,t)$ is the final photoacoustic signal.

3.3 Equation for Pressure

Diebold [45] gives a concise explanation of the governing equation for the pressure that results from launching a photoacoustic wave. When light pulses are delivered to biological tissue, the tissue absorbs the light and converts it to heat, generating an initial pressure rise due to the thermoelastic expansion. The initial pressure gives rise to the acoustic wave, which is then detected by a transducer. The governing equation is given by:

$$\left[\nabla^2 - \frac{1}{c_s^2}\frac{\partial^2}{\partial t^2}\right] p\left(\vec{r},t\right) = -\frac{\beta}{C_p}\frac{\partial H(\vec{r},t)}{\partial t} \tag{3.8}$$

where β is the thermal expansion coefficient, c_s is the speed of sound, C_p is the specific heat, $H(\vec{r},t)$ is the energy per unit volume and time deposited by the optical radiation beam, and $p(\vec{r},t)$ is the pressure of the acoustic wave, a function of space and time.

In this work, it is assumed that the heating function $H(\vec{r},t)$, results from a

chromophore absorber that is optically thin with an optical absorption coefficient μ_a that is heated by an optical pulse with a fluence of F. We assume that $H(\vec{r},t)$ is a separable function of space and time so that the preceding assumptions imply that $H(\vec{r},t) = \mu_a F A(\vec{r}) I(t)$. $A(\vec{r})$ is a function of space that describes the geometry of the absorber and $I(t)$ is a function that describes the time dependence of the incident optical wave, as shown schematically in Figure 3.

Taking the temporal Fourier transform of equation (3.8) and assuming one dimensional Cartesian coordinates so that absorber geometry is a function of the depth variable z only, $\vec{r} = z$, then

$$\frac{d^2}{dz^2}\tilde{p}(z,\omega) + k^2\tilde{p}(z,\omega) = -\frac{ik\beta c_s \mu_a F}{C_p}\tilde{I}(\omega)A(z) \tag{3.9}$$

where $k = \omega / c_s$ is the wavenumber. We now take a spatial Fourier transform (denoted with an overhat) in the spatial variable z, and then equation (3.9) becomes

$$\begin{aligned} -\omega_z^2\hat{\tilde{p}}(\omega_z,\omega) + k^2\hat{\tilde{p}}(\omega_z,\omega) &= -\frac{ik\beta c_s \mu_a F}{C_p}\tilde{I}(\omega)\hat{A}(\omega_z) \\ \hat{\tilde{p}}(\omega_z,\omega) &= \frac{ik\beta c_s \mu_a F}{C_p}\tilde{I}(\omega)\frac{\hat{A}(\omega_z)}{\omega_z^2 - k^2} \\ \hat{\tilde{p}}(\omega_z,\omega) &= \frac{ikp_0}{c_s}\tilde{I}(\omega)\frac{\hat{A}(\omega_z)}{\omega_z^2 - k^2} \end{aligned} \tag{3.10}$$

where p_0 is the initial pressure, μ_a is the absorption coefficient of tissue, and *F* is the local light fluence. Here we can introduce the Grüneisen parameter, which is a constitutive parameter used in photoacoustics. The Grüneisen parameter Γ of tissue, relates the initial pressure p_0 to the light absorption by the following expression [29]:

$$p_0 = \Gamma \mu_a F \tag{3.11}$$

In general, it is necessary to directly measure the Grüneisen parameter of tissue. However, it can also be estimated in terms of the isobaric volume expansion

coefficient β, the specific heat C_p, and the speed of sound c_s in tissue using

$$\Gamma = \frac{\beta c_s^2}{C_p} \tag{3.12}$$

The Grüneisen parameter varies between different types of tissue. For example, the Grüneisen parameter of fat tissue is estimated to be between 0.7 and 0.9. A more accurate value should be obtained by direct measurement.

3.4 Transfer Function and Impulse Response

When viewing the system shown in Figure 3 as an input/output problem, as shown in Figure 4, the transfer function concept is very useful.

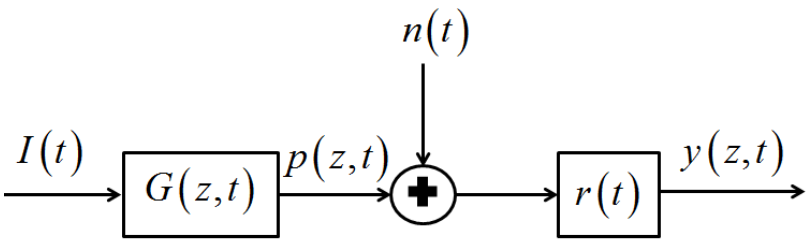

Figure 4 Block diagram of photoacoustic model

The incident laser waveform $I(t)$ is absorbed by the absorber which has the impulse response denoted by $G(z,t)$. The energy in the incident wave is then converted to acoustic energy and generates an acoustic pressure wave $p(z,t)$. The acoustic pressure wave received by a transducer is then transmitted to a receiver-filter which has an impulse response $r(t)$. The signal received at the receiver-filter also contains noise $n(t)$. In this thesis, we assume the noise to be a zero-mean additive Gaussian white noise [24] which has a double-sided power spectral density of $\tilde{S}_{nn}(\omega)$. Furthermore, the noise is assumed to be statistically independent of both the

transmitted input waveform $I(t)$ and the absorber impulse response $G(z,t)$. The output of receiver-filter $y(z,t)$ contains the photoacoustic signal $y_s(z,t)$ and the noise signal $y_n(z,t)$.

Based on this concept, we can write the equation (3.10) as

$$\hat{\tilde{p}}(\omega_z,\omega)=\frac{p_0}{c_s}\frac{ik}{\omega_z^2-k^2}\tilde{I}(\omega)\hat{A}(\omega_z)=\hat{\tilde{G}}(\omega_z,k)\tilde{I}(\omega) \tag{3.13}$$

where

$$\hat{\tilde{G}}(\omega_z,k)=\frac{p_0}{c_s}\frac{ik}{\omega_z^2-k^2}\hat{A}(\omega_z)=\frac{\beta c_s\mu_a F}{C_p}\frac{ik}{\omega_z^2-k^2}\hat{A}(\omega_z) \tag{3.14}$$

is the transfer function. The notation $\hat{\tilde{G}}(\omega_z,k)$, with the overhat and tilde, is used as a reminder that this function is operating in both the spatial and temporal Fourier domain. Furthermore, it is clear from equation (3.14) that $\hat{\tilde{G}}(\omega_z,k)$ is only a function of ω_z and k, along with the assumed constant parameters β,c_s,C_p,μ_a,F.

Taking the inverse spatial Fourier transform of the transfer function $\hat{\tilde{G}}(\omega_z,k)$,

$$\tilde{G}(z,k)=\frac{1}{2\pi}\int_{-\infty}^{\infty}\hat{\tilde{G}}(\omega_z,k)e^{i\omega_z z}d\omega_z=\frac{p_0 ik}{c_s}\int_{-\infty}^{\infty}\frac{1}{\omega_z^2-k^2}\hat{A}(\omega_z)e^{i\omega_z z}d\omega_z \tag{3.15}$$

Theorem 5 from [46] states that the following result holds true:

$$I=\frac{1}{2\pi}\int_{-\infty}^{\infty}\frac{\phi(\rho)}{\rho^2-k^2}e^{i\rho z}\,d\rho=\begin{cases}\dfrac{i}{4k_s}\left[\phi(k)e^{ikz}-\phi(-k)e^{-ikz}\right] & z>0\\ -\dfrac{i}{4k_s}\left[\phi(k)e^{ikz}-\phi(-k)e^{-ikz}\right] & z<0\end{cases} \tag{3.16}$$

or

$$I=\begin{cases}\dfrac{i}{2k}\phi(k)e^{ikz} & z>0\\ \dfrac{i}{2k}\phi(-k)e^{-ikz} & z<0\end{cases} \tag{3.17}$$

or

$$I = \begin{cases} \frac{1}{2ik}\phi(-k)e^{-ikz} & z > 0 \\ \frac{1}{2ik}\phi(k)e^{ikz} & z < 0 \end{cases} \tag{3.18}$$

Here, ϕ is an analytic function defined on the positive real line that remains bounded as *x* goes to infinity (has no poles). The different solutions in (3.16) to (3.18) represent inward, outward propagating waves or standing waves, therefore the physics of the problem governs the choice between equations (3.16) to (3.18). Given the definition of the Fourier transform that is being currently used, the presented result in (3.18) satisfies the Sommerfeld radiation condition, ensuring an outwardly propagating wave.

Given this result, and assuming $\hat{A}(\omega_z)$ has no poles and remains bounded, it follows that

$$\begin{aligned} \tilde{G}(z,k) &= \frac{p_0 ik}{c_s}\int_{-\infty}^{\infty}\frac{1}{\omega_z^2 - k^2}\hat{A}(\omega_z)e^{i\omega_z z}d\omega_z \\ &= \frac{p_0 ik}{c_s}\begin{cases} \frac{1}{2ik}\hat{A}(-k)e^{-ikz} & z > 0 \\ \frac{1}{2ik}\hat{A}(k)e^{ikz} & z < 0 \end{cases} \\ &= \frac{p_0}{2c_s}\begin{cases} \hat{A}(-k)e^{-ikz} & z > 0 \\ \hat{A}(k)e^{ikz} & z < 0 \end{cases} \end{aligned} \tag{3.19}$$

where $k = \frac{\omega}{c_s}$ is the wave number. Temporal inverse Fourier transformation of equation (3.19) gives the system impulse response in the time and space domain as

$$
\begin{aligned}
G(z,t) &= \frac{1}{2\pi}\int_{-\infty}^{\infty}\tilde{G}(z,k)e^{i\omega t}d\omega \\
&= \frac{p_0}{4\pi c_s}\begin{cases}\int_{-\infty}^{\infty}\hat{A}\left(-\frac{\omega}{c_s}\right)e^{-i\omega\frac{z}{c_s}}e^{i\omega t}d\omega & z>0 \\ \int_{-\infty}^{\infty}\hat{A}\left(\frac{\omega}{c_s}\right)e^{i\omega\frac{z}{c_s}}e^{i\omega t}d\omega & z<0\end{cases} \\
&= \frac{p_0}{2c_s}\begin{cases}A(z-c_s t) & z>0 \\ A(z+c_s t) & z<0\end{cases}
\end{aligned}
\tag{3.20}
$$

Equation (3.20) shows that the impulse response of the absorber has exactly the same spatial shape of the inhomogeneity, although it is a function in time whereas the shape of the absorber is a function of space. The speed of sound is the converting factor that relates distances in space to durations in time. Now, the field of pulsed photoacoustics involves the measurement and analysis of photoacoustic responses to input pulses that are sufficiently short so as to be modelled as Dirac-delta functions. Hence, pulsed photoacoustics can be considered the branch of photoacoustics where the primary goal is the direct measurement of the system impulse response and equation (3.20) makes it mathematically clear that in doing so the absorber profile is directly obtained. Furthermore, the 'time for acoustic wave to travel' can be used to estimate the location of the absorber.

3.5 Square Function Absorber in Space

Now consider the specific absorber which is considered a square function in space. Light propagation in this absorber is assumed to have no decay. That is, $A(z)$ is assumed to be given by

$$
A(z) = A_0\left(u\left(z+\frac{l}{2}\right)-u\left(z-\frac{l}{2}\right)\right) \tag{3.21}
$$

where $u(z)$ is a Heaviside unit step function, and A_0 is an arbitrary constant scaling factor. A plot of (3.21) with $l = 0.005(m), A_0 = 1$ is shown in Figure 5. The

thickness l of the absorber is always taken as $0.005(m)$ in other experimental researches [18], [19].

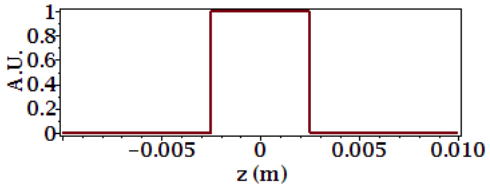

Figure 5 Square absorber model

The spatial Fourier transform of $A(z)$ is given by

$$\hat{A}(\omega_z) = \frac{2}{\omega_z}\sin\left(\frac{l\omega_z}{2}\right) = \frac{1}{i\omega_z}\left(e^{\frac{il\omega_z}{2}} - e^{\frac{-il\omega_z}{2}}\right) \tag{3.22}$$

Substituting equation (3.22) into equation (3.13) for the pressure in spatial and temporal Fourier domain gives

$$\begin{aligned}\hat{\tilde{p}}(\omega_z,\omega) &= \frac{p_0}{c_s}\frac{ik}{\omega_z^2 - k^2}\tilde{I}(\omega)\hat{A}(\omega_z) \\ &= \frac{p_0}{c_s}\frac{ik}{\omega_z^2 - k^2}\tilde{I}(\omega)\frac{1}{i\omega_z}\left(e^{\frac{il\omega_z}{2}} - e^{\frac{-il\omega_z}{2}}\right)\end{aligned} \tag{3.23}$$

There is a pole at zero here, so Theorem 5 in [46] cannot be used immediately. However, partial fractions can be used to separate the pole from the rest of the expression. Therefore, using partial fractions, equation (3.23) can be written as

$$\hat{\tilde{p}}(\omega_z,\omega) = \frac{p_0}{c_s k}\tilde{I}(\omega)\left(e^{\frac{il\omega_z}{2}} - e^{\frac{-il\omega_z}{2}}\right)\left(\frac{\omega_z}{\omega_z^2 - k^2} - \frac{1}{\omega_z}\right) \tag{3.24}$$

Now taking the inverse spatial Fourier transform gives

$$\begin{aligned}\tilde{p}(z,\omega) &= \frac{p_0}{2\pi c_s k}\tilde{I}(\omega)\left\{\int_{-\infty}^{\infty}\frac{\omega_z}{\omega_z^2 - k^2}\left(e^{\frac{il\omega_z}{2}} - e^{\frac{-il\omega_z}{2}}\right)e^{i\omega_z z}d\omega_z - \int_{-\infty}^{\infty}\frac{1}{\omega_z}\left(e^{\frac{il\omega_z}{2}} - e^{\frac{-il\omega_z}{2}}\right)e^{i\omega_z z}d\omega_z\right\} \\ &= \frac{p_0}{2\pi c_s k}\tilde{I}(\omega)\left\{\int_{-\infty}^{\infty}\frac{\omega_z}{\omega_z^2 - k^2}\left(e^{i\omega_z(z+l/2)} - e^{i\omega_z(z-l/2)}\right)d\omega_z - \int_{-\infty}^{\infty}\frac{1}{\omega_z}\left(e^{i\omega_z(z+l/2)} - e^{i\omega_z(z-l/2)}\right)d\omega_z\right\}\end{aligned} \tag{3.25}$$

Using theorem 5, equation (3.18), on the first term and standard integral tables on the second term gives

$$\tilde{p}(z,\omega)=\frac{p_0}{c_s k}\tilde{I}(\omega)\begin{Bmatrix}\dfrac{-ke^{-ik(z+l/2)}}{2ik} & z+l/2>0\\ \dfrac{ke^{ik(z+l/2)}}{2ik} & z+l/2<0\end{Bmatrix}$$
$$-\frac{p_0}{c_s k}\tilde{I}(\omega)\begin{Bmatrix}\dfrac{-ke^{-ik(z-l/2)}}{2ik} & z-l/2>0\\ \dfrac{ke^{ik(z-l/2)}}{2ik} & z-l/2<0\end{Bmatrix} \qquad (3.26)$$
$$+\frac{p_0}{c_s k}\tilde{I}(\omega)\left\{iu\left(z-\frac{l}{2}\right)-iu\left(z+\frac{l}{2}\right)\right\}$$

Cleaning up equation (3.26) gives

$$\tilde{p}(z,\omega)=\frac{p_0}{2c_s ik}\tilde{I}(\omega)\begin{Bmatrix}-e^{-ik(z+l/2)} & z>-l/2\\ e^{ik(z+l/2)} & z<-l/2\end{Bmatrix}$$
$$+\frac{p_0}{2c_s ik}\tilde{I}(\omega)\begin{Bmatrix}e^{-ik(z-l/2)} & z>l/2\\ -e^{ik(z-l/2)} & z<l/2\end{Bmatrix} \qquad (3.27)$$
$$+\frac{p_0}{2c_s ik}\tilde{I}(\omega)\left\{u\left(z+\frac{l}{2}\right)-u\left(z-\frac{l}{2}\right)\right\}$$

Putting it all together gives

$$\tilde{p}(z,\omega)=\frac{p_0}{2c_s ik}\tilde{I}(\omega)\begin{cases}e^{ik(z+l/2)}-e^{ik(z-l/2)} & z<-l/2\\ 2-e^{-ik(z+l/2)}-e^{ik(z-l/2)} & -l/2<z<l/2\\ -e^{-ik(z+l/2)}+e^{-ik(z-l/2)} & z>1/2\end{cases} \qquad (3.28)$$

Inverse (temporal) Fourier transforming equation (3.28) via

$$p(z,t)=\frac{1}{2\pi}\int_{-\infty}^{\infty}\tilde{p}(z,\omega)e^{i\omega t}d\omega \qquad (3.29)$$

Then,

$$p(z,t)=\frac{p_0}{4\pi}\begin{cases}\displaystyle\int_{-\infty}^{\infty}\frac{\tilde{I}(\omega)}{i\omega}\left(e^{i\omega\left(t+\frac{z}{c_s}+\frac{l}{2c_s}\right)}-e^{i\omega\left(t+\frac{z}{c_s}-\frac{l}{2c_s}\right)}\right)d\omega & z<-l/2\\ \displaystyle\int_{-\infty}^{\infty}\frac{\tilde{I}(\omega)}{i\omega}\left(2e^{i\omega t}-e^{i\omega\left(t-\frac{z}{c_s}-\frac{l}{2c_s}\right)}-e^{i\omega\left(t+\frac{z}{c_s}-\frac{l}{2c_s}\right)}\right)d\omega & -l/2<z<l/2\\ \displaystyle-\int_{-\infty}^{\infty}\frac{\tilde{I}(\omega)}{i\omega}\left(e^{i\omega\left(t-\frac{z}{c_s}-\frac{l}{2c_s}\right)}-e^{i\omega\left(t-\frac{z}{c_s}+\frac{l}{2c_s}\right)}\right)d\omega & z>1/2\end{cases}$$

(3.30)

Now it is a known property of Fourier transforms that dividing by $i\omega$ in the frequency domain is the same as integrating in time in the time domain so that

$$\frac{1}{2\pi}\int_{-\infty}^{\infty}\frac{\tilde{I}(\omega)}{i\omega}e^{i\omega t}d\omega=\int_{-\infty}^{t}I(\tau)\,d\tau=Q(t) \tag{3.31}$$

where we use $Q(t)$ to denote the integral of $I(t)$. Using equation (3.31), equation (3.30) can be written as

$$p(z,t)=\frac{p_0}{2}\begin{cases}Q\left(t-\dfrac{(-z-l/2)}{c_s}\right)-Q\left(t-\dfrac{(-z+l/2)}{c_s}\right) & z<-l/2\\ 2Q(t)-Q\left(t-\dfrac{(z+l/2)}{c_s}\right)-Q\left(t-\dfrac{(-z+l/2)}{c_s}\right) & -l/2<z<l/2\\ Q\left(t-\dfrac{(z-l/2)}{c_s}\right)-Q\left(t-\dfrac{(z+l/2)}{c_s}\right) & z>1/2\end{cases}$$

(3.32)

Equation (3.32) is derived by inverse temporal Fourier transform $\tilde{p}(z,\omega)$ shown by equation (3.28). However, the problem can easily be solved in the time domain. The pressure response $p(z,t)$ will be the convolution of the input waveform $I(t)$ and the absorber impulse response $G(z,t)$, which will be given by

$$p(z,t)=\int_{-\infty}^{\infty}I(\tau)G(z,t-\tau)\,d\tau \tag{3.33}$$

For a square absorber shown by equation (3.21), equation (3.33) becomes

$$p(z,t)=\frac{p_0}{2}\begin{cases}\displaystyle\int_{t+\frac{z}{c_s}-\frac{l}{2c_s}}^{t+\frac{z}{c_s}+\frac{l}{2c_s}}I(\tau)\,d\tau & z<0\\ \displaystyle\int_{t-\frac{z}{c_s}-\frac{l}{2c_s}}^{t-\frac{z}{c_s}+\frac{l}{2c_s}}I(\tau)\,d\tau & z>0\end{cases} \tag{3.34}$$

As verification of our prior result, if the input time function is a delta function, $I(t)=\delta(t)$, then its integral is the Heaviside step function $Q(t)=u(t)$, and for

$z > l/2$, equation (3.32) indicates a step function that turns on at time $\frac{(z - l/2)}{c_s}$ and turns off at $\frac{(z + l/2)}{c_s}$, or in other words a step that lasts for an amount of time l/c_s seconds. This is in keeping with our prior result that said that in response to a very short incident pulse in time, the pressure function has the same shape as the spatial shape of the inhomogeneity. The result here is more general as it is valid for any temporal function of input $I(t)$ and square wave absorber. Furthermore, the solution in (3.32) has three regions of validity. The middle region $-l/2 < z < l/2$ is actually inside the inhomogeneity and in practice a transducer would never be placed there.

3.6 Finite Length Step Exponential Absorber in Space

We now consider the response to the absorber spatial function

$$A(z) = e^{-az}u(z) - e^{-az}u(z - l) \tag{3.35}$$

where *a* is positive constant and $u(z)$ is the Heaviside step function. This absorber denotes a light decay when propagating inside the absorber. A plot of (3.35) with $a = 1, l = 0.005$ is shown in Figure 6.

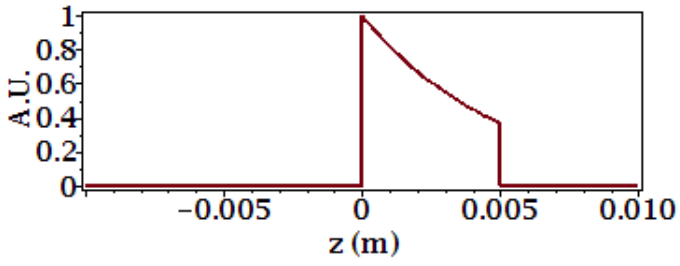

Figure 6 Finite exponential decay absorber model

The spatial Fourier transform of $A(z)$ is given by

$$\hat{A}(\omega_z) = \frac{1}{a+i\omega_z} - \frac{e^{-l(a+i\omega_z)}}{a+i\omega_z} \tag{3.36}$$

The pressure response in both spatial and temporal Fourier domains is given by

$$\begin{aligned}\hat{\tilde{p}}(\omega_z,\omega) &= \frac{p_0}{c_s}\frac{ik}{\omega_z^2-k^2}\tilde{I}(\omega)\hat{A}(\omega_z) \\ &= \frac{p_0}{c_s}\frac{ik}{\omega_z^2-k^2}\tilde{I}(\omega)\left\{\frac{1}{a+i\omega_z}\right\} - \frac{p_0}{c_s}\frac{ik}{\omega_z^2-k^2}\tilde{I}(\omega)\left\{\frac{e^{-l(a+i\omega_z)}}{a+i\omega_z}\right\}\end{aligned} \tag{3.37}$$

This can be written via partial fractions as

$$\hat{\tilde{p}}(\omega_z,\omega) = \frac{p_0}{c_s}\frac{\tilde{I}(\omega)}{\left(a^2+k^2\right)}\left[\frac{(ia+\omega_z)}{\left(\omega_z^2-k^2\right)} - \frac{(ia+\omega_z)e^{-l(a+i\omega_z)}}{\left(\omega_z^2-k^2\right)} + \frac{1}{(ia-\omega_z)} - \frac{e^{-l(a+i\omega_z)}}{(ia-\omega_z)}\right] \tag{3.38}$$

We consider the spatial inverse Fourier transform term by term. The first term in equation (3.38) is

$$\tilde{p}_1(z,\omega) = \frac{p_0}{2c_s}\frac{\tilde{I}(\omega)}{\left(a^2+k^2\right)}\begin{bmatrix}(a+ik)e^{-ikz} & z>0\\ (a-ik)e^{ikz} & z<0\end{bmatrix} \tag{3.39}$$

Second term in equation (3.38)

$$\tilde{p}_2(z,\omega) = -\frac{p_0}{2c_s}\frac{\tilde{I}(\omega)}{\left(a^2+k^2\right)}\begin{bmatrix}(a+ik)e^{-la}e^{-ik(z-l)} & z-l>0\\ (a-ik)e^{-la}e^{ik(z-l)} & z-l<0\end{bmatrix} \tag{3.40}$$

Last two terms in equation (3.38) give

$$\begin{aligned}\tilde{p}_{3,4}(z,\omega) &= \frac{p_0}{c_s}\frac{k\tilde{I}(\omega)}{\left(a^2+k^2\right)}\left[-ie^{-az}u(z)+ie^{-az}u(z-l)\right] \\ &= \frac{p_0}{c_s}\frac{\tilde{I}(\omega)ik}{\left(a^2+k^2\right)}\left[-e^{-az}u(z)+e^{-az}u(z-l)\right]\end{aligned} \tag{3.41}$$

Putting the terms all together

$$\tilde{p}(z,\omega) = \frac{p_0}{2c_s}\frac{\tilde{I}(\omega)}{\left(a^2+k^2\right)}\begin{cases}(a-ik)e^{ikz} - (a-ik)e^{-la}e^{ik(z-l)} & z<0\\ -2ike^{-az} + (a+ik)e^{-ikz} - (a-ik)e^{-la}e^{ik(z-l)} & 0<z<l\\ (a+ik)e^{-ikz} - (a+ik)e^{-la}e^{-ik(z-l)} & z>l\end{cases}$$

(3.42)

We note that the “particular solution”, a term proportional to e^{-az} only appears in the area $0<z<l$ (which is inside the absorber itself). Outside of this area, the response

consists of terms proportional to $\left(e^{\pm ikz}-e^{-la}e^{\pm ik(z-l)}\right)$ plus its time derivative (a multiplication by $i\omega$ in the frequency domain). The term $\left(e^{ikz}-e^{-la}e^{ik(z-l)}\right)$ is two propagating waves, with the second being attenuated by e^{-al} compared to the first. If we set $a=0$ in equation (3.42), it yields the same result as equation (3.28), which is for square function absorber.

Rearrange equation (3.42) gives

$$\tilde{p}(z,\omega)=\frac{p_0\tilde{I}(\omega)}{2\left(\omega^2-(ic_sa)^2\right)}\begin{cases} c_sa\left(e^{ikz}-e^{-la}e^{ik(z-l)}\right)-i\omega\left(e^{ikz}-e^{-la}e^{ik(z-l)}\right) & z<0 \\ -2i\omega e^{-az}+c_sa\left(e^{-ikz}-e^{-la}e^{+ik(z-l)}\right)+i\omega\left(e^{-ikz}+e^{-la}e^{ik(z-l)}\right) & 0<z<l \\ c_sa\left(e^{-ikz}-e^{-la}e^{-ik(z-l)}\right)+i\omega\left(e^{-ikz}-e^{-la}e^{-ik(z-l)}\right) & z>l \end{cases}$$

(3.43)

Although equation (3.43) looks complicated, we can make some interpretations. First consider the inverse temporal Fourier transform of the "leading term" and we define this function to be $L(t)$ and can be simplified using Theorem 5 from [47], given above in (3.18) as

$$L(t):=\frac{p_0}{4\pi}\int_{-\infty}^{\infty}\frac{\tilde{I}(\omega)}{\left(\omega^2-(ic_sa)^2\right)}e^{i\omega t}d\omega=\frac{p_0}{2}\begin{cases}\dfrac{i}{2c_sai}\tilde{I}(c_sai)e^{-c_sat} & t>0\\ \dfrac{i}{2c_sai}\tilde{I}(-c_sai)e^{+c_sat} & t<0\end{cases}$$

$$=\frac{p_0}{4c_sa}\begin{cases}\tilde{I}(c_sai)e^{-c_sat} & t>0\\ \tilde{I}(-c_sai)e^{+c_sat} & t<0\end{cases}$$

(3.44)

Equation (3.44) are decaying exponentials in time with amplitude controlled by $\tilde{I}(\pm c_sai)$. The general shape of (3.44) will be as shown in Figure 7 or Figure 8.

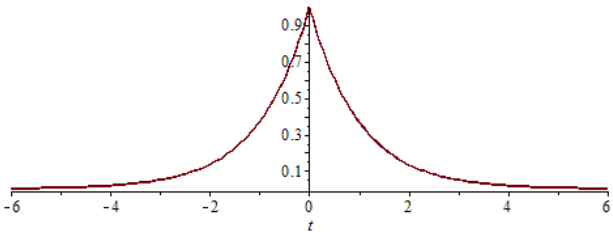

Figure 7 Form of L(t)

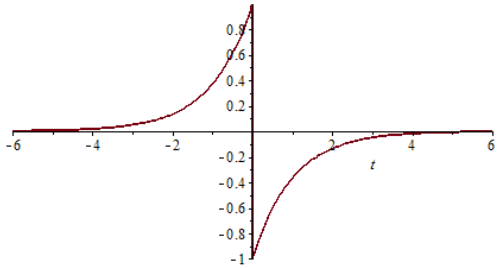

Figure 8 Another possible form of L(t)

The form of the time derivative of $L(t)$ is given by

$$L'(t) := \frac{p_0}{4}\begin{cases} -\tilde{I}(c_s ai)e^{-c_s at} & t > 0 \\ +\tilde{I}(-c_s ai)e^{+c_s at} & t < 0 \end{cases} \tag{3.45}$$

Clearly, from Figure 7, the derivative is not defined at 0, although the function itself is continuous at time zero. Having found closed-form expressions for $L(t)$ and its first time derivative, equation (3.43) can now be interpreted in the time domain as

$$p(z,t) = \begin{cases} c_s aL\left(t+\frac{z}{c_s}\right) - c_s ae^{-la}L\left(t+\frac{(z-l)}{c_s}\right) - L'\left(t+\frac{z}{c_s}\right) + e^{-la}L'\left(t+\frac{(z-l)}{c_s}\right) & z<0 \\ -2e^{-az}L'(t) + c_s aL\left(t-\frac{z}{c_s}\right) - c_s ae^{-la}L\left(t+\frac{(z-l)}{c_s}\right) + L'\left(t-\frac{z}{c_s}\right) + e^{-la}L'\left(t+\frac{(z-l)}{c_s}\right) & 0<z<l \\ c_s aL\left(t-\frac{z}{c_s}\right) - c_s ae^{-la}L\left(t-\frac{(z-l)}{c_s}\right) + L'\left(t-\frac{z}{c_s}\right) - e^{-la}L'\left(t-\frac{(z-l)}{c_s}\right) & z>l \end{cases}$$

(3.46)

Similar to the square absorber, the pressure response can be solved in time domain only using equation (3.33). The only difference is the absorber impulse response $G(z,t)$. As for the exponential decay absorber shown by equation (3.35). The expression for pressure response becomes

$$p(z,t)=\frac{p_0}{2}\begin{cases}\displaystyle\int_{t+\frac{z}{c_s}-\frac{l}{2c_s}}^{t+\frac{z}{c_s}+\frac{l}{2c_s}} I(\tau)e^{-ac_s(t-\tau)}d\tau & z<0\\ \displaystyle\int_{t-\frac{z}{c_s}-\frac{l}{2c_s}}^{t-\frac{z}{c_s}+\frac{l}{2c_s}} I(\tau)e^{-ac_s(t-\tau)}d\tau & z>0\end{cases} \tag{3.46}$$

3.7 The Chirp

In prior sections, the expressions for the pressure response $p(z,t)$ for two different absorbers with any incident wave form $I(t)$ have been derived. The expressions of the signal passed through receiver-filter $y_s(z,t)$ with an incident liner frequency modulated sinusoidal chirp will be demonstrated in the following sections.

The chirp is a commonly used waveform in many applications. For convenience in calculations, it is common to use the complex form of the chirp, but the actual signal is the real part of the complex chirp

$$I(t)=e^{i\pi Kt^2} \tag{3.47}$$

where K is the chirp parameter, a positive constant. It has the dimensions of (Hz)^2 so that Kt^2 is dimensionless. The real version of the signal is given as

$$I_{re}(t)=\cos\left(\pi Kt^2\right) \tag{3.48}$$

The plot of equation (3.48) is shown in Figure 9.

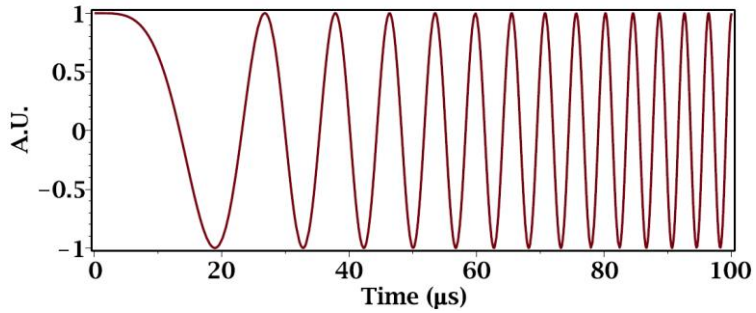

Figure 9 Real part of a complex chirp.

The chirp can be regarded as a signal with an instantaneous frequency defined as

$$\frac{d\left(\pi K t^2\right)}{dt} = 2\pi K t \ \text{ rad/s } = K t \ \text{ Hz} \tag{3.49}$$

It has been shown that the temporal Fourier transform of $I(t)$ is given by [44]

$$\tilde{I}(\omega) = \frac{1}{\sqrt{K}} e^{\frac{i\pi}{4}} e^{-\frac{i\omega^2}{4\pi K}} \tag{3.50}$$

Further, it has been shown that $I_{re}(t)$ has the Fourier transform given by

$$\tilde{I}_{re}(\omega) = \frac{1}{\sqrt{K}} \cos\left(\frac{\omega^2}{4\pi K} - \frac{\pi}{4}\right) \tag{3.51}$$

In practice, the chirp is truncated to be a finite duration pulse with a center frequency, f_0, which is often non-zero. The truncated complex chirp is given by

$$I_T(t) = \text{rect}\left(\frac{t}{T}\right) e^{2\pi i\left(f_0 t + \frac{K t^2}{2}\right)} = \text{rect}\left(\frac{t}{T}\right) e^{i\left(\omega_0 t + \frac{\beta t^2}{2}\right)} \tag{3.52}$$

The subscript *T* indicates the duration of the chirp and may be omitted if the meaning is clear. In equation (3.52), $\omega = 2\pi f$ is the standard conversion from *Hz* to radians per second and $\beta = 2\pi K$. The function $\text{rect}(z)$ is the rectangular function, introduced by Woodward [48], and defined as

$$\text{rect}(z) = \begin{cases} 1 & |z| < \frac{1}{2} \\ 0 & |z| > \frac{1}{2} \end{cases} \tag{3.53}$$

Figure 10 shows how the truncated chirp looks like in time domain.

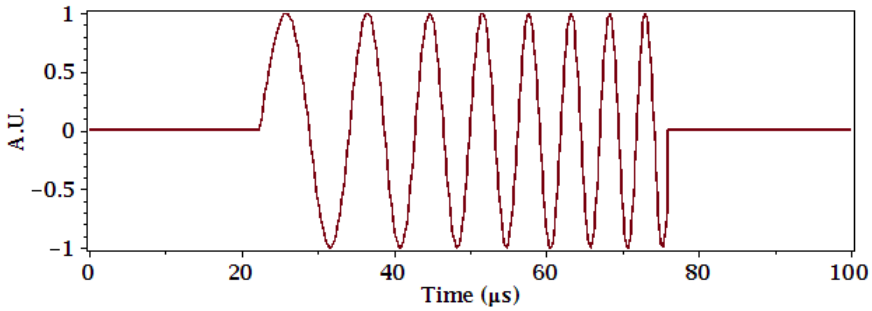

Figure 10 Truncated chirp waveform

As before, the complex chirp can be regarded as a signal with instantaneous frequency defined as

$$\frac{d\left(\omega_0 t+\frac{\beta t^2}{2}\right)}{dt}=\left(\omega_0+\beta t\right)\text{ rad/s }=\left(f_0+Kt\right)\text{ Hz} \tag{3.54}$$

Thus, during the T second interval of the pulse, the instantaneous frequency changes linearly from $\left(f_0-KT/2\right)$ Hz to $\left(f_0+KT/2\right)$ Hz. The frequency sweep, $\Delta=KT$ is then the difference in these two values. The product of duration and frequency sweep $T\Delta$ is then given by KT^2 and is called the time-bandwidth product of the chirp, $D=T\Delta=KT^2$. The time-bandwidth product (dimensionless) is also referred to as the Dispersion Factor in older papers, for example [49]. The function $I_T\left(t\right)$ as defined in equation (3.52) is an even function, therefore its Fourier transform is also even. In particular, $\left|\tilde{I}_T\left(\omega\right)\right|^2$ will be real and even so that the autocorrelation of a complex chirp $I_T\left(t\right)$ is also real and even.

3.8 Autocorrelation of a Finite-Duration Chirp

The auto-correlation of a finite duration chirp may be computed from

$$R_{II}(t) = \int_{-\infty}^{\infty} I_T(t+\tau)\overline{I_T(\tau)}\, d\tau \tag{3.55}$$

which has been shown to be given by [49]

$$R_{II}(t) = \frac{1}{\pi K|t|} e^{2\pi i f_0 t} \sin\left[\pi\left(\Delta|t| - Kt^2\right)\right] \tag{3.56}$$

The envelope of the auto-correlation of a finite-duration chirp is therefore given by

$$R_{II}(t) = \begin{cases} T\dfrac{\sin\left(\pi\,\Delta|t| - \pi K t^2\right)}{\Delta\pi|t|} & -T \le t \le T \\ 0 & \text{otherwise} \end{cases} \tag{3.57}$$

This can be written in an alternate form as

$$R_{II}(t) = \begin{cases} T\left(1-\dfrac{|t|}{T}\right)\dfrac{\sin\left[\Delta\pi t\left(1-\dfrac{|t|}{T}\right)\right]}{\Delta\pi t\left(1-\dfrac{|t|}{T}\right)} & -T \le t \le T \\ 0 & \text{otherwise} \end{cases} \tag{3.58}$$

For small values of time (especially for large time-bandwidth products), this is approximately given by the sinc function

$$R_{II}(t) \approx R_{II}^{approx}(t) = T\frac{\sin\left(\Delta\pi|t|\right)}{\Delta\pi|t|} \quad |t| \ll T \tag{3.59}$$

Therefore, we can define the approximation of $R_{II}(t)$ as $R_{II}^{approx}(t)$, given by the right hand side of equation (3.59).

The $R_{II}(t)$ and $R_{II}^{approx}(t)$ are envelopes of the autocorrelated chirp. A full expression of autocorrelated real cosine chirp is given by

$$R_{II\_\cos}(t) = \begin{cases} T\dfrac{\sin\left(\pi\,\Delta|t| - \pi K t^2\right)}{\Delta\pi|t|}\cos\left(2\pi f_0 t\right) & -T \le t \le T \\ 0 & \text{otherwise} \end{cases} \tag{3.60}$$

The approximation of $R_{II\_\cos}(t)$ is then given by

$$R_{II\_\cos}^{approx}(t)=\begin{cases} T\dfrac{\sin(\pi\,\Delta|t|)}{\Delta\pi|t|}\cos(2\pi f_0 t) & -T\le t\le T \\ 0 & \text{otherwise} \end{cases} \tag{3.61}$$

The plot of $R_{II}(t)$ and $R_{II}^{approx}(t)$ are shown in Figure 11. The chirp parameters used to draw the plots are as follows: $T=1\times10^{-3}(s)$, $\Delta=3\times10^{6}(Hz)$, $f_0=0$.

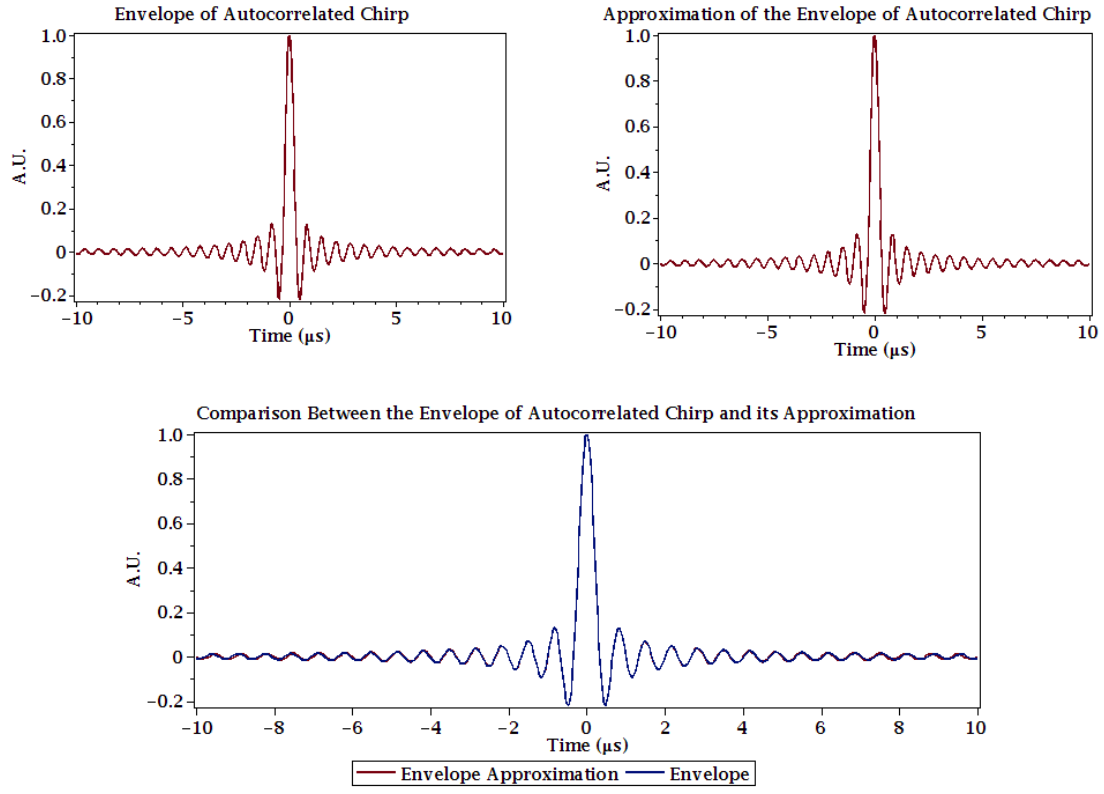

Figure 11 **plots of** $R_{II}(t)$ *and* $R_{II}^{approx}(t)$

For the plots in Figure 11, the first zero crossing of equation (3.59) is at $t=1/\Delta$ and the duration of the main lobe of the sinc function is $2/\Delta=2/(KT)$, which will be referred to as the "effective pulse duration". The important point is that the energy of the autocorrelation of the chirp is concentrated in a much narrower duration of time than the original chirp $I_T(t)$, which had a duration of *T*. The pulse compression ratio is then defined as the ratio of the duration of the original pulse $I_T(t)$ to the duration of the autocorrelation of the pulse, which is given by

$$CR = \frac{\text{duration of } I_T(t)}{\text{duration of } R_{II}(t)} = \frac{T}{2/\Delta} = \frac{\Delta T}{2} \tag{3.62}$$

Thus, we see that the pulse compression ratio is directly proportional to the time-bandwidth product, ΔT .

From Figure 11, since the first zero crossing of $R_{II}^{approx}(t)$ is at $t = 1/\Delta = 0.333\mu s$, 66 points have been sampled from 0.005 μs to 0.33 μs for calculation convenience, and found the maximum error is 3.38% using the equation

$$Error_{\max} = \max\left|\frac{R_{II}(t_i) - R_{II}^{approx}(t_i)}{R_{II}(t_i)}\right|, i = 1..66 \tag{3.63}$$

As shown in Figure 11 and the corresponding maximum error, the difference between $R_{II}(t)$ and $R_{II}^{approx}(t)$ could be ignored.

3.9 Real Laser Chirp Waveform

In previous sections, the chirp as shown in Figure 9 was being used. The magnitude of this chirp contains negative values, which does not make physical sense if the quantity being represented is an intensity value as in the case of laser intensity. The real laser chirp must oscillate above zero intensity. The shifted chirp (shifted up) has the wave form

$$I(t) = I_0 + \cos\left(\pi K t^2 + 2\pi f_0 t\right) \tag{3.64}$$

where I_0 is an arbitrary constant shift factor to ensure that the function always remains positive. A plot of equation (3.64) with $f_0 = 100(Hz), I_0 = 1$ is shown in Figure 12.

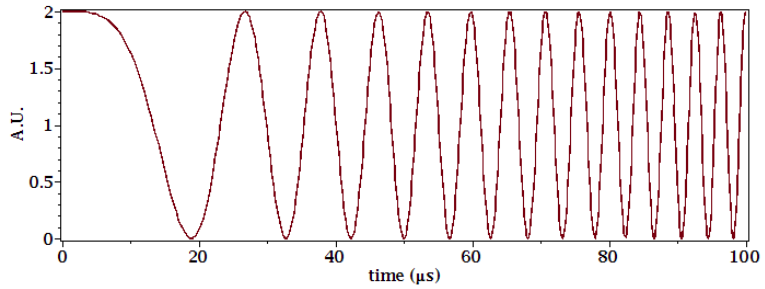

Figure 12 Shifted cosine chirp

The autocorrelation equation for the shifted chirp becomes extremely long and takes several pages, Therefore, it is shown in the appendix A. A plot of the autocorrelation with parameters $f_0 = 0, T = 1(ms), \Delta = 2.8\times10^6\,(Hz)$ is shown in Figure 13.

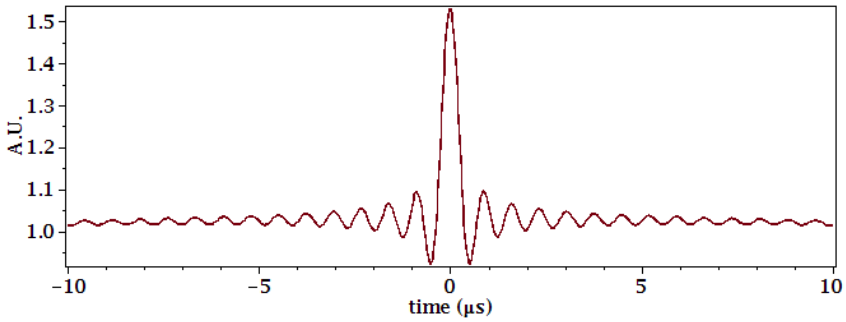

Figure 13 Autocorrelation of shifted cosine chirp

The plot of the unshifted cosine chirp shown in equation (3.61) with the same parameters except I_0 is shown in Figure 14.

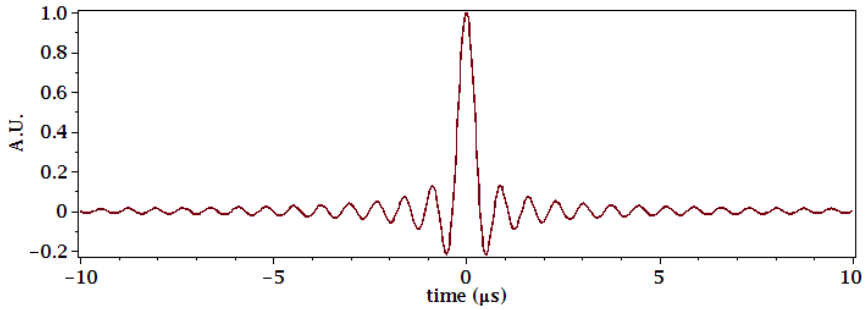

Figure 14 Autocorrelation of unshifted cosine chirp

Comparison between Figure 13 and Figure 14 shows that by shifting the chirp up, the autocorrelation of the chirp is also shifted by a factor. The shape does not change much, especially for the main lobe. Manipulations on shifted chirp autocorrelation have been made to investigate the difference.

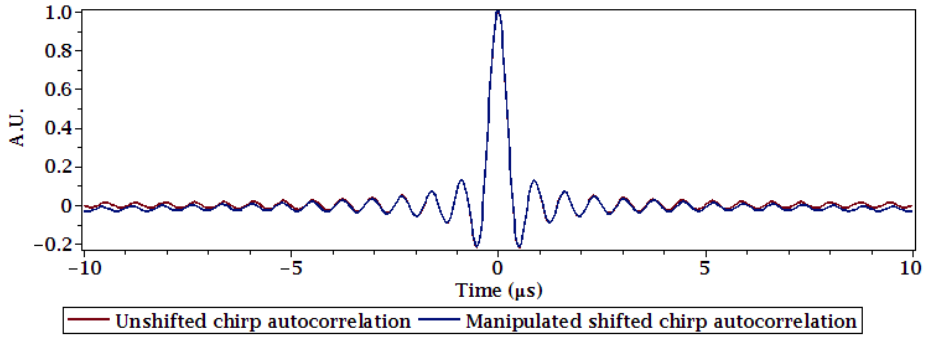

Figure 15 Comparison between unshifted chirp autocorrelation and manipulated shifted chirp autocorrelation

The manipulated autocorrelation of shifted chirp and the unshifted chirp autocorrelation are shown in Figure 15. The manipulation is done by multiplying the shifted chirp autocorrelation by a factor of 2 and subtracting 2.06. As shown in Figure 15, the difference is small. In order to quantify the error in the main lobe, 66 points in the time interval 0.005 μs to 0.33 μs with constant spacing have been sampled for unshifted chirp autocorrelation $R_{II}^{unshifted}(t)$ and manipulated shifted chirp autocorrelation $R_{II}^{shifted}(t)$. The maximum error in this time interval was calculated as

$$Error_{\max} = \max\left|\frac{R_{II}^{unshifted}(t_i) - R_{II}^{shifted}(t_i)}{R_{II}^{unshifted}(t_i)}\right| \qquad i = 1..N \qquad (3.65)$$

where N is the number of points, in this case 66. The maximum error between $R_{II}^{unshifted}(t)$ and $R_{II}^{shifted}(t)$ in Figure 15 is 2.97%. With this result, it is justifiable to use the simpler equation, $I(t) = \cos\left(\pi K t^2 + 2\pi f_0 t\right)$ in simulations and obtain results that are similar to those obtained with a shifted chirp, without unnecessary mathematical complications.

3.10 Pressure response – autocorrelated chirp and square absorber

In order to investigate the chirp parameters' effects on corresponding photoacoustic signal after the receiver-filter $y_s(z,t)$, the mathematical expressions of $y_s(z,t)$ for a square absorber are derived in this section.

3.10.1 Antiderivative approach

Previously, in equation (3.28), the temporal Fourier transform of the pressure response for a square function absorber was shown to be given by

$$\tilde{p}(z,\omega)=\frac{p_0}{2i\omega}\tilde{I}(\omega)\begin{cases} e^{ik(z+l/2)}-e^{ik(z-l/2)} & z<-l/2 \\ 2-e^{-ik(z+l/2)}-e^{ik(z-l/2)} & -l/2<z<l/2 \\ -e^{-ik(z+l/2)}+e^{-ik(z-l/2)} & z>l/2 \end{cases} \tag{3.66}$$

where $k=\omega/c$ is the wavenumber. Equation (3.66) then can be written in input/output form as

$$\tilde{p}(z,\omega)=\tilde{G}(z,\omega)\tilde{I}(\omega) \tag{3.67}$$

where $\tilde{G}(z,\omega)$ is the transfer function of the system at some measurement point z, and is given by

$$\tilde{G}(z,\omega)=\frac{p_0}{2i\omega}\begin{cases} e^{i\frac{\omega}{c}\left(z+\frac{l}{2}l\right)}-e^{i\frac{\omega}{c}\left(z-\frac{l}{2}l\right)} & z<-l/2 \ \text{(reflection)} \\ -e^{-i\frac{\omega}{c}\left(z+\frac{l}{2}l\right)}+e^{-i\frac{\omega}{c}\left(z-\frac{l}{2}l\right)} & z>l/2 \ \text{(transmission)} \end{cases} \tag{3.68}$$

It is noted that $\tilde{G}(z,\omega)$ possesses slightly different forms for measurements made in reflection (transducer on irradiated side of the sample) or transmission (transducer on the other side of the sample). Temporal inverse Fourier transforming equation (3.68) gives the system impulse response as

$$G(z,t)=\frac{p_0}{2}\begin{cases} u\left(t+\dfrac{z}{c_s}+\dfrac{l}{2c_s}\right)-u\left(t+\dfrac{z}{c_s}-\dfrac{l}{2c_s}\right) & z<-l/2 \text{ (reflection)} \\ u\left(t+\dfrac{z}{c_s}-\dfrac{l}{2c_s}\right)-u\left(t+\dfrac{z}{c_s}+\dfrac{l}{2c_s}\right) & z>l/2 \quad \text{(transmission)} \end{cases}$$

(3.69)

In equation (3.69), $u(t)$ is the Heaviside step function so that the shape of the impulse response is a square rectangle function in time at any fixed observation point z.

It was further demonstrated that inverse temporal Fourier transformation of (3.66) leads to

$$p(z,t)=\frac{p_0}{2}\begin{cases} Q\left(t+\dfrac{z}{c_s}+\dfrac{l}{2c_s}\right)-Q\left(t+\dfrac{z}{c_s}-\dfrac{l}{2c_s}\right) & z<-l/2 \\ 2Q(t)-Q\left(t-\dfrac{z}{c_s}-\dfrac{l}{2c_s}\right)-Q\left(t+\dfrac{z}{c_s}-\dfrac{l}{2c_s}\right) & -l/2<z<l/2 \\ -Q\left(t-\dfrac{z}{c_s}-\dfrac{l}{2c_s}\right)+Q\left(t-\dfrac{z}{c_s}+\dfrac{l}{2c_s}\right) & z>l/2 \end{cases}$$

(3.70)

where the function $Q(t)$ is the integral of the time function given by

$$Q(t)=\frac{1}{2\pi}\int_{-\infty}^{\infty}\frac{\tilde{I}(\omega)}{i\omega}e^{i\omega t}d\omega=\int_{-\infty}^{t}I(\tau)\,d\tau \tag{3.71}$$

In order to obtain the photoacoustic signal after the receiver-filter where the received filter is a matched filter to the input chip – that is the receiver filter is the complex conjugate of the input chirp, we need to replace $I(\tau)$ in equation (3.70) with $R_{II}^{approx}(\tau)$ (the autocorrelation of the input signal) in equation (3.71) so that

$$Q_{approx}(t)=\int_{-\infty}^{t}R_{II}^{approx}(\tau)\,d\tau \tag{3.72}$$

Via Maple, equation (3.72) can be found as

$$Q_{approx}\left(t\right)=\begin{cases}0 & t\le -\frac{1}{2}T\\ \frac{T(Si(\frac{1}{2}T\pi\Delta)+Si(t\pi\Delta))}{\pi\Delta} & -\frac{1}{2}T\le t\le\frac{1}{2}T\\ \frac{2Si(\frac{1}{2}T\pi\Delta)T}{\pi\Delta} & \frac{1}{2}T<t\end{cases} \tag{3.73}$$

where $Si(x)$ is the Sine Integral given by

$$Si(x)=\int_0^x\frac{\sin\left(t\right)}{t}dt \tag{3.74}$$

For the case of $z<-l/2$ (reflection), using equation (3.70) gives

$$y_s\left(z,t\right)=\frac{p_0}{2}\left(Q_{approx}\left(t+\frac{z}{c_s}+\frac{l}{2c_s}\right)-Q_{approx}\left(t+\frac{z}{c_s}-\frac{l}{2c_s}\right)\right) \tag{3.75}$$

Via Maple, this can be computed as

$$y_s\left(z,t\right)=\frac{p_0}{2}\left[\begin{cases}0 & t+\frac{l}{2c_s}+\frac{z}{c_s}\le-\frac{T}{2}\\ \frac{T(Si(\frac{1}{2}\frac{\Delta\pi\left(2c_st+l+2z\right)}{c_s})+Si(\frac{1}{2}T\pi\Delta))}{\pi\Delta} & -\frac{T}{2}\le t+\frac{l}{2c_s}+\frac{z}{c_s}\le\frac{1}{2}T\\ \frac{2Si(\frac{1}{2}T\pi\Delta)T}{\pi\Delta} & \frac{T}{2}<t+\frac{l}{2c_s}+\frac{z}{c_s}\end{cases}\right.$$
$$\left.-\begin{cases}0 & t-\frac{l}{2c_s}+\frac{z}{c_s}\le-\frac{1}{2}T\\ \frac{T(Si(\frac{1}{2}\frac{\Delta\pi\left(2c_st-l+2z\right)}{c_s})+Si(\frac{1}{2}T\pi\Delta))}{\pi\Delta} & -\frac{T}{2}\le t-\frac{l}{2c_s}+\frac{z}{c_s}\le\frac{1}{2}T\\ \frac{2Si(\frac{1}{2}T\pi\Delta)T}{\pi\Delta} & \frac{T}{2}<t-\frac{l}{2c_s}+\frac{z}{c_s}\end{cases}\right] \tag{3.76}$$

A plot of equation (3.76) is shown in Figure 16.

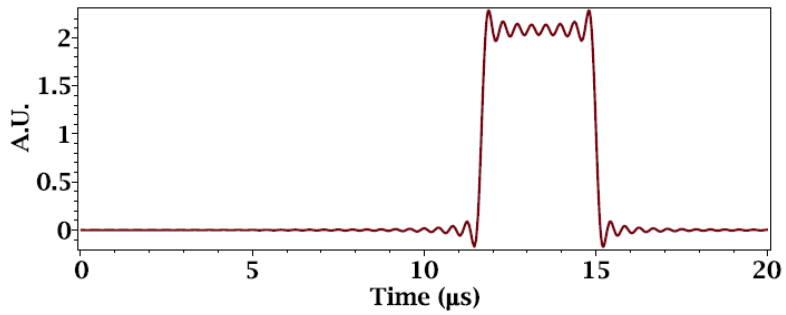

Figure 16 Photoacoustic Signal from Envelope of Autocorrelated Chirp

Figure 16 shows a "fake" square shape function with duration of approximately l/c_s, which is compatible to the previous statement that the process of auto-correlating a chirps gives a "fake" Dirac-delta function input wave, which in turn is expected to give a response function that resembles the shape of the absorber $A(z)$.

3.10.2 Piece by Piece integration

The method of calculating pressure response shown in equation (3.70) is by taking the antiderivative of $R_{II}^{approx}(t)$, which is denoted by $Q_{approx}(t)$, and then calculating the response by using the equation $Q_{approx}\left(t+\frac{z}{c_s}+\frac{l}{2c_s}\right)-Q_{approx}\left(t+\frac{z}{c_s}-\frac{l}{2c_s}\right)$. Another method of obtaining the pressure response is to directly integrate in time using the $\int_{t+\frac{z}{c_s}-\frac{l}{2c_s}}^{t+\frac{z}{c_s}+\frac{l}{2c_s}} R_{II}^{approx}(\tau)\,d\tau$. In doing this, we have defined two conditions $\frac{l}{c_s}<\frac{T}{2}$ and $\frac{l}{c_s}>\frac{T}{2}$. That is, for $z<-l/2$ equation (3.70) becomes

$$y_s(z,t)=\frac{p_0}{2}\int_{t+\frac{z}{c_s}-\frac{l}{2c_s}}^{t+\frac{z}{c_s}+\frac{l}{2c_s}} R_{II}^{approx}(\tau)\,d\tau \qquad z<-l/2 \tag{3.77}$$

Performing the integral in (3.77) with a piece-by-piece (interval) approach, several

possible cases need to be considered. The first case is $\frac{l}{c_s} < \frac{T}{2}$, or that the duration of half the input pulse is longer than the transit time of the absorber. In this case, the integration becomes

$$y_s(z,t) = \frac{p_0}{2}\begin{cases} 0 & t < -\frac{T}{2} \\ \int_{t-\frac{l}{c_s}}^{t} R_{II}^{approx}(\tau)d\tau & -\frac{T}{2} < t < \frac{l}{c_s} - \frac{T}{2} \\ \int_{t-\frac{l}{c_s}}^{t} R_{II}^{approx}(\tau)d\tau & \frac{l}{c_s} - \frac{T}{2} < t < 0 \\ \int_{t-\frac{l}{c_s}}^{t} R_{II}^{approx}(\tau)d\tau & 0 < t < \frac{l}{c_s} \\ \int_{t-\frac{l}{c_s}}^{t} R_{II}^{approx}(\tau)d\tau & \frac{l}{c_s} < t < \frac{T}{2} \\ \int_{t-\frac{l}{c_s}}^{\frac{T}{2}} R_{II}^{approx}(\tau)d\tau & \frac{T}{2} < t < \frac{l}{c_s} + \frac{T}{2} \\ 0 & \frac{T}{2} + \frac{l}{c_s} < t \end{cases} \tag{3.78}$$

Since the variable z in $y_s(z,t)$ is the distance between absorber and the transducer, and is fixed when doing the simulation, and it only affects the time delay of the propagating signal, it can be considered that the pressure response $p(z,t)$ and the photoacoustic signal $y_s(z,t)$ are functions of t only.

The result given by Maple is

$$y_s(t) = \frac{p_0}{2}\begin{cases} 0 & -\frac{T}{2} > t \\ \dfrac{T\left(Si(t\Delta\pi) + Si\left(\frac{1}{2}T\Delta\pi\right)\right)}{\Delta\pi} & -\frac{T}{2} < t < \frac{l}{c_s} - \frac{T}{2} \\ \dfrac{T\left(Si(t\Delta\pi) - Si\left(\frac{(c_s t - l)\Delta\pi}{c_s}\right)\right)}{\Delta\pi} & \frac{l}{c_s} - \frac{T}{2} < t < \frac{T}{2} \\ \dfrac{T\left(Si\left(\frac{1}{2}T\Delta\pi\right) - Si\left(\frac{(c_s t - l)\Delta\pi}{c_s}\right)\right)}{\Delta\pi} & \frac{T}{2} < t < \frac{l}{c_s} + \frac{T}{2} \\ 0 & \frac{T}{2} + \frac{l}{c_s} < t \end{cases} \quad (3.79)$$

A plot of equation (3.79) is shown in Figure 17:

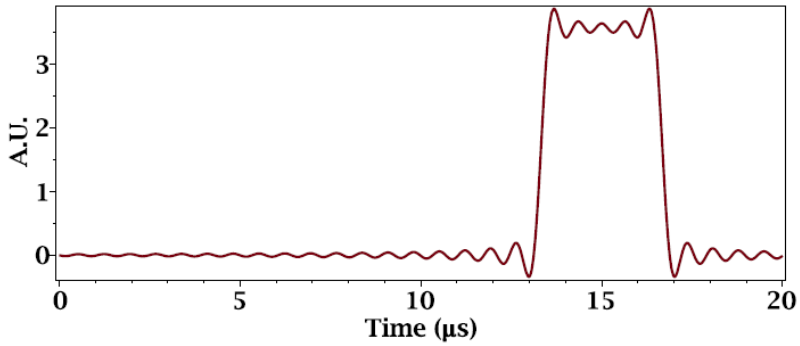

Figure 17 Photoacoustic Signal from Envelope of Autocorrelated Chirp

The second possible case is that $\frac{l}{c_s} > \frac{T}{2}$, or that the duration of half-pulse is smaller than the transit time of the absorber. In this case, the integration becomes

$$y_s(t)=\frac{p_0}{2}\begin{cases} 0 & t<-\dfrac{T}{2} \\ \displaystyle\int_{-\frac{T}{2}}^{t} R_{II}^{approx}(\tau)d\tau & -\dfrac{T}{2}<t<0 \\ \displaystyle\int_{-\frac{T}{2}}^{t} R_{II}^{approx}(\tau)d\tau & 0<t<\dfrac{l}{c_s}-\dfrac{T}{2} \\ \displaystyle\int_{t-\frac{l}{c_s}}^{t} R_{II}^{approx}(\tau)d\tau & \dfrac{l}{c_s}-\dfrac{T}{2}<t<\dfrac{T}{2} \\ \displaystyle\int_{t-\frac{l}{c_s}}^{\frac{T}{2}} R_{II}^{approx}(\tau)d\tau & \dfrac{T}{2}<t<\dfrac{l}{c_s} \\ \displaystyle\int_{t-\frac{l}{c_s}}^{\frac{T}{2}} R_{II}^{approx}(\tau)d\tau & \dfrac{l}{c_s}<t<\dfrac{l}{c_s}+\dfrac{T}{2} \\ 0 & \dfrac{T}{2}+\dfrac{l}{c_s}<t \end{cases} \qquad (3.80)a$$

The result given by Maple is

$$y_s(t)=\frac{p_0}{2}\begin{cases} 0 & t<-\dfrac{T}{2} \\ \dfrac{T\left(Si\left(t\Delta\pi\right)+Si\left(\frac{1}{2}T\Delta\pi\right)\right)}{\Delta\pi} & -\dfrac{T}{2}<t<\dfrac{l}{c_s}-\dfrac{T}{2} \\ \dfrac{T\left(Si\left(t\Delta\pi\right)-Si\left(\frac{\left(c_s t-l\right)\Delta\pi}{c_s}\right)\right)}{\Delta\pi} & \dfrac{l}{c_s}-\dfrac{T}{2}<t<\dfrac{T}{2} \\ \dfrac{T\left(Si\left(\frac{1}{2}T\Delta\pi\right)-Si\left(\frac{\left(c_s t-l\right)\Delta\pi}{c_s}\right)\right)}{\Delta\pi} & \dfrac{T}{2}<t<\dfrac{l}{c_s}+\dfrac{T}{2} \\ 0 & \dfrac{T}{2}+\dfrac{l}{c_s}<t \end{cases} \qquad (3.81)$$

A plot of equation (3.81) is shown in Figure 18:

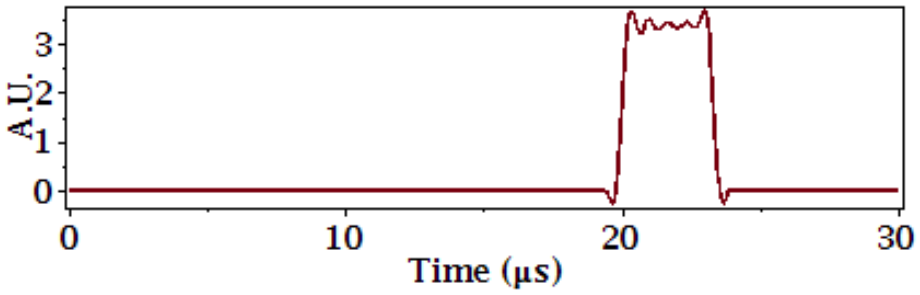

Figure 18 Photoacoustic Signal from Envelope of Autocorrelated Chirp

Figure 17 and Figure 18 show that the method of integrating directly through the designated time interval can also give us the proper pressure response of the simulation.

3.10.3 Autocorrelated cosine chirp pressure response

Figure 16, Figure 17 and Figure 18 are the photoacoustic signal derived from the *envelope* of autocorrelated chirp. The photoacoustic signal for autocorrelated real cosine chirp for the condition $\frac{l}{c_s} < \frac{T}{2}$ is given by

$$y_s(t)=\frac{p_0}{2}\begin{cases}0 & t<-\dfrac{T}{2}\\ \displaystyle\int_{t-\frac{l}{c_s}}^{t} R_{II\_\cos}^{approx}(\tau)d\tau & -\dfrac{T}{2}<t<\dfrac{l}{c_s}-\dfrac{T}{2}\\ \displaystyle\int_{t-\frac{l}{c_s}}^{t} R_{II\_\cos}^{approx}(\tau)d\tau & \dfrac{l}{c_s}-\dfrac{T}{2}<t<0\\ \displaystyle\int_{t-\frac{l}{c_s}}^{t} R_{II\_\cos}^{approx}(\tau)d\tau & 0<t<\dfrac{l}{c_s}\\ \displaystyle\int_{t-\frac{l}{c_s}}^{t} R_{II\_\cos}^{approx}(\tau)d\tau & \dfrac{l}{c_s}<t<\dfrac{T}{2}\\ \displaystyle\int_{t-\frac{l}{c_s}}^{\frac{T}{2}} R_{II\_\cos}^{approx}(\tau)d\tau & \dfrac{T}{2}<t<\dfrac{l}{c_s}+\dfrac{T}{2}\\ 0 & \dfrac{T}{2}+\dfrac{l}{c_s}<t\end{cases} \tag{3.82}$$

where now the autocorrelated chirp response is given by

$$R_{II\_\cos}^{approx}(\tau)=R_{II}^{approx}(\tau)\cdot\cos\left(2\pi f_0\tau\right) \tag{3.83}$$

Equation (3.82) can be rewritten in the form

$$y_s(t)=\frac{p_0}{2}\begin{cases}0 & t<-\dfrac{T}{2}\\ Y_1(t) & -\dfrac{T}{2}<t<\dfrac{l}{c_s}-\dfrac{T}{2}\\ Y_2(t) & \dfrac{l}{c_s}-\dfrac{T}{2}<t<0\\ Y_3(t) & 0<t<\dfrac{l}{c_s}\\ Y_4(t) & \dfrac{l}{c_s}<t<\dfrac{T}{2}\\ Y_5(t) & \dfrac{T}{2}<t<\dfrac{l}{c_s}+\dfrac{T}{2}\\ 0 & \dfrac{T}{2}+\dfrac{l}{c_s}<t\end{cases} \tag{3.84}$$

The components of equation (3.84), $Y_i(t)$, can be found using Maple

$$Y_1(t)=\frac{p_0T}{2\Delta\pi}\left(Si\left(\frac{1}{2}T\Delta\pi-\pi Tf_0\right)+Si\left(\frac{1}{2}T\Delta\pi+\pi Tf_0\right)+Si\left(\Delta\pi t-2\pi f_0t\right)+Si\left(\Delta\pi t+2\pi f_0t\right)\right)$$

(3.85)

$$Y_2(t)=\frac{p_0T}{2\Delta\pi}\left(Si\left(\Delta\pi t-2\pi f_0t\right)+Si\left(\Delta\pi t+2\pi f_0t\right)-Si\left(\Delta\pi t-2\pi f_0t-\Delta\pi\frac{l}{c_s}+2\pi f_0\frac{l}{c_s}\right)\right.$$
$$\left.-Si\left(\Delta\pi t+2\pi f_0t-\Delta\pi\frac{l}{c_s}-2\pi f_0\frac{l}{c_s}\right)\right)$$

(3.86)

$$Y_3(t)=\frac{p_0T}{2\Delta\pi}\left(Si\left(\Delta\pi t-2\pi f_0t\right)+Si\left(\Delta\pi t+2\pi f_0t\right)-Si\left(\Delta\pi t-2\pi f_0t-\Delta\pi\frac{l}{c_s}+2\pi f_0\frac{l}{c_s}\right)\right.$$
$$\left.-Si\left(\Delta\pi t+2\pi f_0t-\Delta\pi\frac{l}{c_s}-2\pi f_0\frac{l}{c_s}\right)\right)$$

(3.87)

$$Y_4(t)=\frac{p_0T}{2\Delta\pi}\left(Si\left(\Delta\pi t-2\pi f_0t\right)+Si\left(\Delta\pi t+2\pi f_0t\right)-Si\left(\Delta\pi t-2\pi f_0t-\Delta\pi\frac{l}{c_s}+2\pi f_0\frac{l}{c_s}\right)\right.$$
$$\left.-Si\left(\Delta\pi t+2\pi f_0t-\Delta\pi\frac{l}{c_s}-2\pi f_0\frac{l}{c_s}\right)\right)$$

(3.88)

$$Y_5(t)=\frac{p_0T}{2\Delta\pi}\left(Si\left(\frac{1}{2}T\Delta\pi-\pi Tf_0\right)+Si\left(\frac{1}{2}T\Delta\pi+\pi Tf_0\right)-Si\left(\Delta\pi t-2\pi f_0t-\Delta\pi\frac{l}{c_s}+2\pi f_0\frac{l}{c_s}\right)\right.$$
$$\left.-Si\left(\Delta\pi t+2\pi f_0t-\Delta\pi\frac{l}{c_s}-2\pi f_0\frac{l}{c_s}\right)\right)$$

(3.89)

A plot of equation (3.84) obtained by Maple is shown in Figure 19:

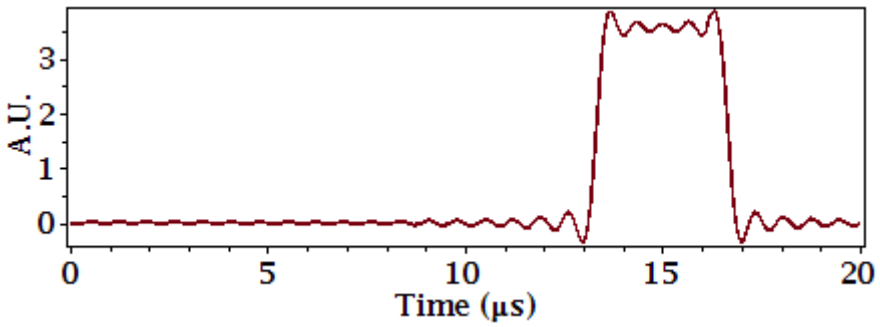

Figure 19 Photoacoustic signal from the autocorrelated cosine chirp

In the second (shorter pulse) condition where $\frac{l}{c_s} > \frac{T}{2}$, the pressure response is

$$y_s(t) = \frac{p_0}{2}\begin{cases} 0 & t < -\frac{T}{2} \\ \int_{-\frac{T}{2}}^{t} R_{II\_\cos}^{approx}(\tau)d\tau & -\frac{T}{2} < t < 0 \\ \int_{-\frac{T}{2}}^{t} R_{II\_\cos}^{approx}(\tau)d\tau & 0 < t < \frac{l}{c_s} - \frac{T}{2} \\ \int_{t-\frac{l}{c_s}}^{t} R_{II\_\cos}^{approx}(\tau)d\tau & \frac{l}{c_s} - \frac{T}{2} < t < \frac{T}{2} \\ \int_{t-\frac{l}{c_s}}^{\frac{T}{2}} R_{II\_\cos}^{approx}(\tau)d\tau & \frac{T}{2} < t < \frac{l}{c_s} \\ \int_{t-\frac{l}{c_s}}^{\frac{T}{2}} R_{II\_\cos}^{approx}(\tau)d\tau & \frac{l}{c_s} < t < \frac{l}{c_s} + \frac{T}{2} \\ 0 & \frac{T}{2} + \frac{l}{c_s} < t \end{cases} \tag{3.90}$$

which can be written as

$$y_s(t)=\frac{p_0}{2}\begin{cases}0 & t<-\dfrac{T}{2}\\ Y_1(t) & -\dfrac{T}{2}<t<0\\ Y_2(t) & 0<t<\dfrac{l}{c_s}-\dfrac{T}{2}\\ Y_3(t) & \dfrac{l}{c_s}-\dfrac{T}{2}<t<\dfrac{T}{2}\\ Y_4(t) & \dfrac{T}{2}<t<\dfrac{l}{c_s}\\ Y_5(t) & \dfrac{l}{c_s}<t<\dfrac{l}{c_s}+\dfrac{T}{2}\\ 0 & \dfrac{T}{2}+\dfrac{l}{c_s}<t\end{cases} \tag{3.91}$$

Again, as above the $Y_i(t)$ can be found via Maple as

$$Y_1(t)=\frac{p_0T}{2\Delta\pi}\left(Si\left(\frac{1}{2}T\Delta\pi-\pi Tf_0\right)+Si\left(\frac{1}{2}T\Delta\pi+\pi Tf_0\right)+Si\left(\Delta\pi t-2\pi f_0t\right)+Si\left(\Delta\pi t+2\pi f_0t\right)\right)$$

(3.92)

$$Y_2(t)=\frac{p_0T}{2\Delta\pi}\left(Si\left(\frac{1}{2}T\Delta\pi-\pi Tf_0\right)+Si\left(\frac{1}{2}T\Delta\pi+\pi Tf_0\right)+Si\left(\Delta\pi t-2\pi f_0t\right)+Si\left(\Delta\pi t+2\pi f_0t\right)\right)$$

(3.93)

$$Y_3(t)=\frac{p_0T}{2\Delta\pi}\left(Si\left(\Delta\pi t-2\pi f_0t\right)+Si\left(\Delta\pi t+2\pi f_0t\right)-Si\left(\Delta\pi t-2\pi f_0t-\Delta\pi\frac{l}{c_s}+2\pi f_0\frac{l}{c_s}\right)\right.$$
$$\left.-Si\left(\Delta\pi t+2\pi f_0t-\Delta\pi\frac{l}{c_s}-2\pi f_0\frac{l}{c_s}\right)\right)$$

(3.94)

$$Y_4(t)=\frac{p_0T}{2\Delta\pi}\left(Si\left(\frac{1}{2}T\Delta\pi-\pi Tf_0\right)+Si\left(\frac{1}{2}T\Delta\pi+\pi Tf_0\right)-Si\left(\Delta\pi t-2\pi f_0t-\Delta\pi\frac{l}{c_s}+2\pi f_0\frac{l}{c_s}\right)\right.$$
$$\left.-Si\left(\Delta\pi t+2\pi f_0t-\Delta\pi\frac{l}{c_s}-2\pi f_0\frac{l}{c_s}\right)\right)$$

(3.95)

$$Y_5(t)=\frac{p_0T}{2\Delta\pi}\left(Si\left(\frac{1}{2}T\Delta\pi-\pi Tf_0\right)+Si\left(\frac{1}{2}T\Delta\pi+\pi Tf_0\right)-Si\left(\Delta\pi t-2\pi f_0t-\Delta\pi\frac{l}{c_s}+2\pi f_0\frac{l}{c_s}\right)\right.$$
$$\left.-Si\left(\Delta\pi t+2\pi f_0t-\Delta\pi\frac{l}{c_s}-2\pi f_0\frac{l}{c_s}\right)\right)$$

(3.96)

A plot of equation (3.91) obtained by Maple is shown in Figure 20

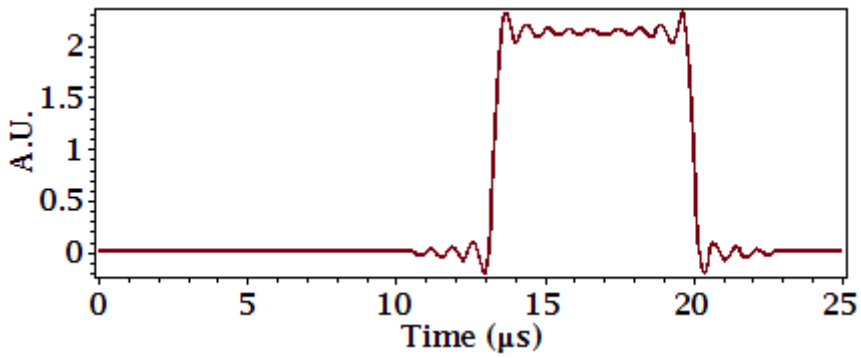

Figure 20 Photoacoustic Signal from Autocorrelated cos Chirp

Figure 19 and Figure 20 obtained by using the full cosine chip expression showed results very similar to those of with Figure 17 and Figure 18, which used the simplified envelope expression. However, in order to test the effects of chirp parameters, we have to use the full cosine chip expression because it is the only expression that contains the chirp center frequency f_0 which is an important controlling parameter.

3.11 Pressure response – autocorrelated chirp with an exponential decay finite absorber

Similar to the previous section, the mathematical expression for the photoacoustic signal $y_s(z,t)$ after the receiver-filter is developed for a finite length exponential decay absorber. The exponential decay absorber is more realistic than a square absorber, since the light decays during the transmission inside the absorber. The purpose of using two different absorber models is to avoid potential coincidental phenomenon that that is specific to only one absorber.

3.11.1 Antiderivative

In the same approach used for the square absorber, the first approach used to calculate the pressure response for the finite exponential absorber was to take the antiderivative of $R_{II}^{approx}(\tau)\cdot\exp(-ac(t-\tau))$, and then obtain the photoacoustic signal by subtracting $Q_{approx}\left(t+\frac{z}{c_s}\right)$ and $Q_{approx}\left(t+\frac{z}{c_s}-\frac{l}{c_s}\right)$. However, this approach proved problematic for Maple and the antiderivative could not be obtained. Hence, the second approach of integrating in time over each appropriate time interval was used.

3.11.2 Piece by Piece Integration

Similar as to the approach used for the square wave absorber, two conditions on the duration of the input signal were defined and the integration was performed piece by piece using Maple. The only difference in the exponential decay absorber case is that when $f_0=\frac{\Delta}{2}$, there is a pole in the expression. So another expression for the exponential decay absorber photoacoustic signal needed to be derived in the special

case of $f_0 = \frac{\Delta}{2}$.

The first condition is $\frac{l}{c_s} < \frac{T}{2}$. When $f_0 \neq \frac{\Delta}{2}$, the equation for pressure response is given by

$$y_s(t) = \frac{p_0}{2}\begin{cases} 0 & t < -\frac{T}{2} \\ Y_1(t) & -\frac{T}{2} < t < \frac{l}{c_s} - \frac{T}{2} \\ Y_2(t) & \frac{l}{c_s} - \frac{T}{2} < t < 0 \\ Y_3(t) & 0 < t < \frac{l}{c_s} \\ Y_4(t) & \frac{l}{c_s} < t < \frac{T}{2} \\ Y_5(t) & \frac{T}{2} < t < \frac{l}{c_s} + \frac{T}{2} \\ 0 & \frac{T}{2} + \frac{l}{c_s} < t \end{cases} \tag{3.97}$$

where

$$\begin{aligned} Y_1(t) = \frac{ip_0 T e^{-ac_s t}}{4\Delta\pi}\Bigg(& -Ei\left(1, \frac{1}{2}ac_s T + \frac{1}{2}i\Delta\pi T + i\pi f_0 T\right) + Ei\left(1, \frac{1}{2}ac_s T - \frac{1}{2}i\Delta\pi T + i\pi f_0 T\right) \\ & - Ei\left(1, \frac{1}{2}ac_s T + \frac{1}{2}i\Delta\pi T - i\pi f_0 T\right) + Ei\left(1, \frac{1}{2}ac_s T - \frac{1}{2}i\Delta\pi T - i\pi f_0 T\right) \\ & + Ei\left(1, -ac_s t - i\Delta\pi t - 2i\pi f_0 t\right) - Ei\left(1, -ac_s t + i\Delta\pi t - 2i\pi f_0 t\right) \\ & + Ei\left(1, -ac_s t - i\Delta\pi t + 2i\pi f_0 t\right) - Ei\left(1, -ac_s t + i\Delta\pi t + 2i\pi f_0 t\right)\Bigg) \end{aligned} \tag{3.98}$$

$$
\begin{aligned}
Y_2(t) = \frac{ip_0 T e^{-ac_s t}}{4\Delta\pi}\Bigg(& -Ei\left(1, -\mathrm{i}\,\Delta\pi t - 2i\pi f_0 t + i\Delta\pi\frac{l}{c_s} + 2i\pi f_0\frac{l}{c_s} - ac_s t + al\right) \\
& + Ei\left(1, \mathrm{i}\,\Delta\pi t - 2i\pi f_0 t - i\Delta\pi\frac{l}{c_s} + 2i\pi f_0\frac{l}{c_s} - ac_s t + al\right) \\
& - Ei\left(1, -\mathrm{i}\,\Delta\pi t + 2i\pi f_0 t + i\Delta\pi\frac{l}{c_s} - 2i\pi f_0\frac{l}{c_s} - ac_s t + al\right) \\
& + Ei\left(1, \mathrm{i}\,\Delta\pi t + 2i\pi f_0 t - i\Delta\pi\frac{l}{c_s} - 2i\pi f_0\frac{l}{c_s} - ac_s t + al\right) \\
& + Ei\left(1, -ac_s t - i\Delta\pi t - 2i\pi f_0 t\right) - Ei\left(1, -ac_s t + i\Delta\pi t - 2i\pi f_0 t\right) \\
& + Ei\left(1, -ac_s t - i\Delta\pi t + 2i\pi f_0 t\right) - Ei\left(1, -ac_s t + i\Delta\pi t + 2i\pi f_0 t\right)\Bigg)
\end{aligned}
\tag{3.99}
$$

$$
\begin{aligned}
Y_3(t) = \frac{ip_0 T e^{-ac_s t}}{4\Delta\pi}\Big(& -\ln\left(ac_s + i\Delta\pi + 2i\pi f_0\right) + \ln\left(ac_s - i\Delta\pi + 2i\pi f_0\right) \\
& - \ln\left(ac_s + i\Delta\pi - 2i\pi f_0\right) + \ln\left(ac_s - i\Delta\pi - 2i\pi f_0\right) \\
& + \ln\left(-ac_s - i\Delta\pi - 2i\pi f_0\right) - \ln\left(-ac_s + i\Delta\pi - 2i\pi f_0\right) \\
& + \ln\left(-ac_s - i\Delta\pi + 2i\pi f_0\right) - \ln\left(-ac_s + i\Delta\pi + 2i\pi f_0\right) \\
& - Ei\left(1, -\mathrm{i}\,\Delta\pi t - 2i\pi f_0 t + i\Delta\pi\frac{l}{c_s} + 2i\pi f_0\frac{l}{c_s} - ac_s t + al\right) \\
& + Ei\left(1, \mathrm{i}\,\Delta\pi t - 2i\pi f_0 t - i\Delta\pi\frac{l}{c_s} + 2i\pi f_0\frac{l}{c_s} - ac_s t + al\right) \\
& - Ei\left(1, -\mathrm{i}\,\Delta\pi t + 2i\pi f_0 t + i\Delta\pi\frac{l}{c_s} - 2i\pi f_0\frac{l}{c_s} - ac_s t + al\right) \\
& + Ei\left(1, \mathrm{i}\,\Delta\pi t + 2i\pi f_0 t - i\Delta\pi\frac{l}{c_s} - 2i\pi f_0\frac{l}{c_s} - ac_s t + al\right) \\
& + Ei\left(1, -ac_s t - i\Delta\pi t - 2i\pi f_0 t\right) - Ei\left(1, -ac_s t + i\Delta\pi t - 2i\pi f_0 t\right) \\
& + Ei\left(1, -ac_s t - i\Delta\pi t + 2i\pi f_0 t\right) - Ei\left(1, -ac_s t + i\Delta\pi t + 2i\pi f_0 t\right)\Big)
\end{aligned}
\tag{3.100}
$$

$$
\begin{aligned}
Y_4(t) = \frac{ip_0 T e^{-ac_s t}}{4\Delta\pi}\Bigg(& -Ei\left(1, -\mathrm{i}\,\Delta\pi t - 2i\pi f_0 t + i\Delta\pi\frac{l}{c_s} + 2i\pi f_0\frac{l}{c_s} - ac_s t + al\right) \\
& + Ei\left(1, \mathrm{i}\,\Delta\pi t - 2i\pi f_0 t - i\Delta\pi\frac{l}{c_s} + 2i\pi f_0\frac{l}{c_s} - ac_s t + al\right) \\
& - Ei\left(1, -\mathrm{i}\,\Delta\pi t + 2i\pi f_0 t + i\Delta\pi\frac{l}{c_s} - 2i\pi f_0\frac{l}{c_s} - ac_s t + al\right) \\
& + Ei\left(1, \mathrm{i}\,\Delta\pi t + 2i\pi f_0 t - i\Delta\pi\frac{l}{c_s} - 2i\pi f_0\frac{l}{c_s} - ac_s t + al\right) \\
& + Ei\left(1, -ac_s t - i\Delta\pi t - 2i\pi f_0 t\right) - Ei\left(1, -ac_s t + i\Delta\pi t - 2i\pi f_0 t\right) \\
& + Ei\left(1, -ac_s t - i\Delta\pi t + 2i\pi f_0 t\right) - Ei\left(1, -ac_s t + i\Delta\pi t + 2i\pi f_0 t\right)\Bigg)
\end{aligned}
\tag{3.101}
$$

$$
\begin{aligned}
Y_5(t) = \frac{ip_0 T e^{-ac_s t}}{4\Delta\pi}\Bigg(& -Ei\left(1, -\mathrm{i}\,\Delta\pi t - 2i\pi f_0 t + i\Delta\pi\frac{l}{c_s} + 2i\pi f_0\frac{l}{c_s} - ac_s t + al\right) \\
& + Ei\left(1, \mathrm{i}\,\Delta\pi t - 2i\pi f_0 t - i\Delta\pi\frac{l}{c_s} + 2i\pi f_0\frac{l}{c_s} - ac_s t + al\right) \\
& - Ei\left(1, -\mathrm{i}\,\Delta\pi t + 2i\pi f_0 t + i\Delta\pi\frac{l}{c_s} - 2i\pi f_0\frac{l}{c_s} - ac_s t + al\right) \\
& + Ei\left(1, \mathrm{i}\,\Delta\pi t + 2i\pi f_0 t - i\Delta\pi\frac{l}{c_s} - 2i\pi f_0\frac{l}{c_s} - ac_s t + al\right) \\
& + Ei\left(1, -\frac{1}{2}ac_s T - \frac{1}{2}i\Delta\pi T - i\pi f_0 T\right) - Ei\left(1, -\frac{1}{2}ac_s T + \frac{1}{2}i\Delta\pi T - i\pi f_0 T\right) \\
& + Ei\left(1, -\frac{1}{2}ac_s T - \frac{1}{2}i\Delta\pi T + i\pi f_0 T\right) - Ei\left(1, -\frac{1}{2}ac_s T + i\Delta\pi T + i\pi f_0 T\right)\Bigg)
\end{aligned}
\tag{3.102}
$$

where $Ei\left(1, f(t)\right) = \int_1^\infty e^{-kf(t)}k^{-1}dk$, and k is a dummy variable.

When $f_0 = \frac{\Delta}{2}$, equation (3.97) remains the same, but the $Y_i(t)$ become

$$
\begin{aligned}
Y_1(t) = \frac{ip_0 T e^{-ac_s t}}{4\Delta\pi}\Bigg(& -Ei\left(1, \frac{1}{2}ac_s T + i\Delta\pi T\right) + Ei\left(1, \frac{1}{2}ac_s T - i\Delta\pi T\right) \\
& + Ei\left(1, -ac_s t - 2i\Delta\pi t\right) + Ei\left(1, -ac_s t + 2i\Delta\pi t\right)\Bigg)
\end{aligned}
\tag{3.103}
$$

$$Y_2(t)=\frac{ip_0Te^{-ac_st}}{4\Delta\pi}\left(-Ei\left(1,-2\,\mathrm{i}\,\Delta\pi t+2i\Delta\pi\frac{l}{c_s}-ac_st+al\right)\right.$$
$$+Ei\left(1,2\,\mathrm{i}\,\Delta\pi t-2i\Delta\pi\frac{l}{c_s}-ac_st+al\right) \tag{3.104}$$
$$\left.+Ei\left(1,-ac_st-2i\Delta\pi t\right)-Ei\left(1,-ac_st+2i\Delta\pi t\right)\right)$$

$$Y_3(t)=\frac{ip_0Te^{-ac_st}}{4\Delta\pi}\left(-\ln\left(ac_s+2i\Delta\pi\right)+\ln\left(ac_s-2i\Delta\pi\right)\right.$$
$$+\ln\left(-ac_s-2i\Delta\pi\right)-\ln\left(-ac_s+2i\Delta\pi\right)$$
$$-Ei\left(1,-2\,\mathrm{i}\,\Delta\pi t+i\Delta\pi\frac{l}{c_s}-ac_st+al\right) \tag{3.105}$$
$$+Ei\left(1,2\,\mathrm{i}\,\Delta\pi t-2i\Delta\pi\frac{l}{c_s}-ac_st+al\right)$$
$$\left.+Ei\left(1,-ac_st-2i\Delta\pi t\right)-Ei\left(1,-ac_st+2i\Delta\pi t\right)\right)$$

$$Y_4(t)=\frac{ip_0Te^{-ac_st}}{4\Delta\pi}\left(-Ei\left(1,-2\,\mathrm{i}\,\Delta\pi t+2i\Delta\pi\frac{l}{c_s}-ac_st+al\right)\right.$$
$$+Ei\left(1,2\,\mathrm{i}\,\Delta\pi t-2i\Delta\pi\frac{l}{c_s}-ac_st+al\right) \tag{3.106}$$
$$\left.+Ei\left(1,-ac_st-2i\Delta\pi t\right)-Ei\left(1,-ac_st+2i\Delta\pi t\right)\right)$$

$$Y_5(t)=\frac{ip_0Te^{-ac_st}}{4\Delta\pi}\left(-Ei\left(1,-2\,\mathrm{i}\,\Delta\pi t+2i\Delta\pi\frac{l}{c_s}-ac_st+al\right)\right.$$
$$+Ei\left(1,2\,\mathrm{i}\,\Delta\pi t-2i\Delta\pi\frac{l}{c_s}-ac_st+al\right) \tag{3.107}$$
$$\left.+Ei\left(1,-\frac{1}{2}ac_sT-i\Delta\pi T\right)-Ei\left(1,-\frac{1}{2}ac_sT+i\Delta\pi T\right)\right)$$

The second condition is the shorter pulse condition of $\frac{l}{c_s}>\frac{T}{2}$. When $f_0\neq\frac{\Delta}{2}$, the equation for pressure response is

$$y_s(t)=\frac{p_0}{2}\begin{cases}0 & t<-\dfrac{T}{2}\\ Y_1(t) & -\dfrac{T}{2}<t<0\\ Y_2(t) & 0<t<\dfrac{l}{c_s}-\dfrac{T}{2}\\ Y_3(t) & \dfrac{l}{c_s}-\dfrac{T}{2}<t<\dfrac{T}{2}\\ Y_4(t) & \dfrac{T}{2}<t<\dfrac{l}{c_s}\\ Y_5(t) & \dfrac{l}{c_s}<t<\dfrac{l}{c_s}+\dfrac{T}{2}\\ 0 & \dfrac{T}{2}+\dfrac{l}{c_s}<t\end{cases} \tag{3.108}$$

where

$$\begin{aligned}Y_1(t)=\frac{ip_0Te^{-ac_st}}{4\Delta\pi}\Bigg(&-Ei\left(1,\frac{1}{2}ac_sT+\frac{1}{2}i\Delta\pi T+i\pi f_0T\right)+Ei\left(1,\frac{1}{2}ac_sT-\frac{1}{2}i\Delta\pi T+i\pi f_0T\right)\\&-Ei\left(1,\frac{1}{2}ac_sT+\frac{1}{2}i\Delta\pi T-i\pi f_0T\right)+Ei\left(1,\frac{1}{2}ac_sT-\frac{1}{2}i\Delta\pi T-i\pi f_0T\right)\\&+Ei\left(1,-ac_st-i\Delta\pi t-2i\pi f_0t\right)-Ei\left(1,-ac_st+i\Delta\pi t-2i\pi f_0t\right)\\&+Ei\left(1,-ac_st-i\Delta\pi t+2i\pi f_0t\right)-Ei\left(1,-ac_st+i\Delta\pi t+2i\pi f_0t\right)\Bigg)\end{aligned}$$

(3.109)

$$\begin{aligned}Y_2(t)=\frac{ip_0Te^{-ac_st}}{4\Delta\pi}\Big(&-\ln\left(ac_s+i\Delta\pi+2i\pi f_0\right)+\ln\left(ac_s-i\Delta\pi+2i\pi f_0\right)\\&-\ln\left(ac_s+i\Delta\pi-2i\pi f_0\right)+\ln\left(ac_s-i\Delta\pi-2i\pi f_0\right)\\&+\ln\left(-ac_s-i\Delta\pi-2i\pi f_0\right)-\ln\left(-ac_s+i\Delta\pi-2i\pi f_0\right)\\&+\ln\left(-ac_s-i\Delta\pi+2i\pi f_0\right)-\ln\left(-ac_s+i\Delta\pi+2i\pi f_0\right)\\&-Ei\left(1,\frac{1}{2}ac_sT+\frac{1}{2}i\Delta\pi T+i\pi f_0T\right)+Ei\left(1,\frac{1}{2}ac_sT-\frac{1}{2}i\Delta\pi T+i\pi f_0T\right)\\&-Ei\left(1,\frac{1}{2}ac_sT+\frac{1}{2}i\Delta\pi T-i\pi f_0T\right)+Ei\left(1,\frac{1}{2}ac_sT-\frac{1}{2}i\Delta\pi T-i\pi f_0T\right)\\&+Ei\left(1,-ac_st-i\Delta\pi t-2i\pi f_0t\right)-Ei\left(1,-ac_st+i\Delta\pi t-2i\pi f_0t\right)\\&+Ei\left(1,-ac_st-i\Delta\pi t+2i\pi f_0t\right)-Ei\left(1,-ac_st+i\Delta\pi t+2i\pi f_0t\right)\Big)\end{aligned}$$

(3.110)

$$
\begin{aligned}
Y_3(t) = \frac{ip_0 T e^{-ac_s t}}{4\Delta\pi}\Big(&-\ln\left(ac_s + i\Delta\pi + 2i\pi f_0\right) + \ln\left(ac_s - i\Delta\pi + 2i\pi f_0\right) \\
&- \ln\left(ac_s + i\Delta\pi - 2i\pi f_0\right) + \ln\left(ac_s - i\Delta\pi - 2i\pi f_0\right) \\
&+ \ln\left(-ac_s - i\Delta\pi - 2i\pi f_0\right) - \ln\left(-ac_s + i\Delta\pi - 2i\pi f_0\right) \\
&+ \ln\left(-ac_s - i\Delta\pi + 2i\pi f_0\right) - \ln\left(-ac_s + i\Delta\pi + 2i\pi f_0\right) \\
&- Ei\left(1, -\mathrm{i}\,\Delta\pi t - 2i\pi f_0 t + i\Delta\pi\frac{l}{c_s} + 2i\pi f_0\frac{l}{c_s} - ac_s t + al\right) \\
&+ Ei\left(1, \mathrm{i}\,\Delta\pi t - 2i\pi f_0 t - i\Delta\pi\frac{l}{c_s} + 2i\pi f_0\frac{l}{c_s} - ac_s t + al\right) \\
&- Ei\left(1, -\mathrm{i}\,\Delta\pi t + 2i\pi f_0 t + i\Delta\pi\frac{l}{c_s} - 2i\pi f_0\frac{l}{c_s} - ac_s t + al\right) \\
&+ Ei\left(1, \mathrm{i}\,\Delta\pi t + 2i\pi f_0 t - i\Delta\pi\frac{l}{c_s} - 2i\pi f_0\frac{l}{c_s} - ac_s t + al\right) \\
&+ Ei\left(1, -ac_s t - i\Delta\pi t - 2i\pi f_0 t\right) - Ei\left(1, -ac_s t + i\Delta\pi t - 2i\pi f_0 t\right) \\
&+ Ei\left(1, -ac_s t - i\Delta\pi t + 2i\pi f_0 t\right) - Ei\left(1, -ac_s t + i\Delta\pi t + 2i\pi f_0 t\right)\Big)
\end{aligned}
\tag{3.111}
$$

$$
\begin{aligned}
Y_4(t) = \frac{ip_0 T e^{-ac_s t}}{4\Delta\pi}\Big(&-\ln\left(ac_s + i\Delta\pi + 2i\pi f_0\right) + \ln\left(ac_s - i\Delta\pi + 2i\pi f_0\right) \\
&- \ln\left(ac_s + i\Delta\pi - 2i\pi f_0\right) + \ln\left(ac_s - i\Delta\pi - 2i\pi f_0\right) \\
&+ \ln\left(-ac_s - i\Delta\pi - 2i\pi f_0\right) - \ln\left(-ac_s + i\Delta\pi - 2i\pi f_0\right) \\
&+ \ln\left(-ac_s - i\Delta\pi + 2i\pi f_0\right) - \ln\left(-ac_s + i\Delta\pi + 2i\pi f_0\right) \\
&- Ei\left(1, -\mathrm{i}\,\Delta\pi t - 2i\pi f_0 t + i\Delta\pi\frac{l}{c_s} + 2i\pi f_0\frac{l}{c_s} - ac_s t + al\right) \\
&+ Ei\left(1, \mathrm{i}\,\Delta\pi t - 2i\pi f_0 t - i\Delta\pi\frac{l}{c_s} + 2i\pi f_0\frac{l}{c_s} - ac_s t + al\right) \\
&- Ei\left(1, -\mathrm{i}\,\Delta\pi t + 2i\pi f_0 t + i\Delta\pi\frac{l}{c_s} - 2i\pi f_0\frac{l}{c_s} - ac_s t + al\right) \\
&+ Ei\left(1, \mathrm{i}\,\Delta\pi t + 2i\pi f_0 t - i\Delta\pi\frac{l}{c_s} - 2i\pi f_0\frac{l}{c_s} - ac_s t + al\right) \\
&+ Ei\left(1, -\frac{1}{2}ac_s T - \frac{1}{2}i\Delta\pi T - i\pi f_0 T\right) - Ei\left(1, -\frac{1}{2}ac_s T + \frac{1}{2}i\Delta\pi T - i\pi f_0 T\right) \\
&+ Ei\left(1, -\frac{1}{2}ac_s T - \frac{1}{2}i\Delta\pi T + i\pi f_0 T\right) - Ei\left(1, -\frac{1}{2}ac_s T + i\Delta\pi T + i\pi f_0 T\right)\Big)
\end{aligned}
$$

(3.112)

$$
\begin{aligned}
Y_5(t) = \frac{ip_0 T e^{-ac_s t}}{4\Delta\pi}\Bigg(& -Ei\left(1, -\mathrm{i}\,\Delta\pi t - 2i\pi f_0 t + i\Delta\pi\frac{l}{c_s} + 2i\pi f_0\frac{l}{c_s} - ac_s t + al\right) \\
& + Ei\left(1, \mathrm{i}\,\Delta\pi t - 2i\pi f_0 t - i\Delta\pi\frac{l}{c_s} + 2i\pi f_0\frac{l}{c_s} - ac_s t + al\right) \\
& - Ei\left(1, -\mathrm{i}\,\Delta\pi t + 2i\pi f_0 t + i\Delta\pi\frac{l}{c_s} - 2i\pi f_0\frac{l}{c_s} - ac_s t + al\right) \\
& + Ei\left(1, \mathrm{i}\,\Delta\pi t + 2i\pi f_0 t - i\Delta\pi\frac{l}{c_s} - 2i\pi f_0\frac{l}{c_s} - ac_s t + al\right) \\
& + Ei\left(1, -\frac{1}{2}ac_s T - \frac{1}{2}i\Delta\pi T - i\pi f_0 T\right) - Ei\left(1, -\frac{1}{2}ac_s T + \frac{1}{2}i\Delta\pi T - i\pi f_0 T\right) \\
& + Ei\left(1, -\frac{1}{2}ac_s T - \frac{1}{2}i\Delta\pi T + i\pi f_0 T\right) - Ei\left(1, -\frac{1}{2}ac_s T + i\Delta\pi T + i\pi f_0 T\right)\Bigg)
\end{aligned}
$$

(3.113)

When $f_0 = \frac{\Delta}{2}$, equation (3.108) remains the same, but the $Y_i(t)$ become

$$
\begin{aligned}
Y_1(t) = \frac{ip_0 T e^{-ac_s t}}{4\Delta\pi}\Bigg(& -Ei\left(1, \frac{1}{2}ac_s T + i\Delta\pi T\right) + Ei\left(1, \frac{1}{2}ac_s T - i\Delta\pi T\right) \\
& + Ei\left(1, -ac_s t - 2i\Delta\pi t\right) - Ei\left(1, -ac_s t + 2i\Delta\pi t\right)\Bigg)
\end{aligned}
\tag{3.114}
$$

$$
\begin{aligned}
Y_2(t) = \frac{ip_0 T e^{-ac_s t}}{4\Delta\pi}\Big(& -\ln\left(ac_s + 2i\Delta\pi\right) + \ln\left(ac_s - 2i\Delta\pi\right) \\
& + \ln\left(-ac_s - 2i\Delta\pi\right) - \ln\left(-ac_s + 2i\Delta\pi\right) \\
& - Ei\left(1, \mathrm{i}\,\Delta\pi t + \frac{1}{2}ac_s T\right) + Ei\left(1, -\mathrm{i}\,\Delta\pi t + \frac{1}{2}ac_s t\right) \\
& + Ei\left(1, -ac_s t - 2i\Delta\pi t\right) - Ei\left(1, -ac_s t + 2i\Delta\pi t\right)\Big)
\end{aligned}
\tag{3.115}
$$

$$
\begin{aligned}
Y_3(t) = \frac{ip_0 T e^{-ac_s t}}{4\Delta\pi}\Big(&-\ln\left(ac_s + 2i\Delta\pi\right) + \ln\left(ac_s - 2i\Delta\pi\right) \\
&+ \ln\left(-ac_s - 2i\Delta\pi\right) - \ln\left(-ac_s + 2i\Delta\pi\right) \\
&- Ei\left(1, -2\,\mathrm{i}\,\Delta\pi t + i\Delta\pi\frac{l}{c_s} - ac_s t + al\right) \\
&+ Ei\left(1, 2\,\mathrm{i}\,\Delta\pi t - 2i\Delta\pi\frac{l}{c_s} - ac_s t + al\right) \\
&+ Ei\left(1, -ac_s t - 2i\Delta\pi t\right) - Ei\left(1, -ac_s t + 2i\Delta\pi t\right)\Big)
\end{aligned}
\tag{3.116}
$$

$$
\begin{aligned}
Y_4(t) = \frac{ip_0 T e^{-ac_s t}}{4\Delta\pi}\Big(&-\ln\left(ac_s + 2i\Delta\pi\right) + \ln\left(ac_s - 2i\Delta\pi\right) \\
&+ \ln\left(-ac_s - 2i\Delta\pi\right) - \ln\left(-ac_s + 2i\Delta\pi\right) \\
&- Ei\left(1, -2\,\mathrm{i}\,\Delta\pi t + 2i\Delta\pi\frac{l}{c_s} - ac_s t + al\right) \\
&+ Ei\left(1, 2\,\mathrm{i}\,\Delta\pi t - 2i\Delta\pi\frac{l}{c_s} - ac_s t + al\right) \\
&+ Ei\left(1, -\frac{1}{2}ac_s t - i\Delta\pi T\right) - Ei\left(1, -\frac{1}{2}ac_s t + i\Delta\pi T\right)\Big)
\end{aligned}
\tag{3.117}
$$

$$
\begin{aligned}
Y_5(t) = \frac{ip_0 T e^{-ac_s t}}{4\Delta\pi}\Big(&-Ei\left(1, -2\,\mathrm{i}\,\Delta\pi t + 2i\Delta\pi\frac{l}{c_s} - ac_s t + al\right) \\
&+ Ei\left(1, 2\,\mathrm{i}\,\Delta\pi t - 2i\Delta\pi\frac{l}{c_s} - ac_s t + al\right) \\
&+ Ei\left(1, -\frac{1}{2}ac_s T - i\Delta\pi T\right) - Ei\left(1, -\frac{1}{2}ac_s T + i\Delta\pi T\right)\Big)
\end{aligned}
\tag{3.118}
$$

In this section and section 3.10, the closed form expression of signals $y_s(t)$ at the output of the receiver-filter $r(t)$ with the input chirp waveform $I(t)$ have been developed. With these expressions for square and exponential decay absorbers, it is now able to test the chirp parameters' effects on SNR and resolution.

3.12 Resolution

In order to quantify the quality of the signal at the output of receiver-filter $y_s(t)$, the concept of resolution is introduced. In this work, the resolution of the signal at the output of the Receiver-Filter is defined as the error between the signal obtained, $y_s(t)$, and the absorber ideal pressure response $y_{ideal}(t)$ in the time interval where $y_{ideal}(t)$ is non-zero. The absorber ideal response is modeled as a perfect square wave, which would be the response to a perfect Dirac-delta, that is, the impulse response. A plot of $y_{ideal}(t)$ for a square absorber with $l = 0.005\,(\text{m}),\ c_s = 1500(\text{m/s})$ is shown in Figure 21.

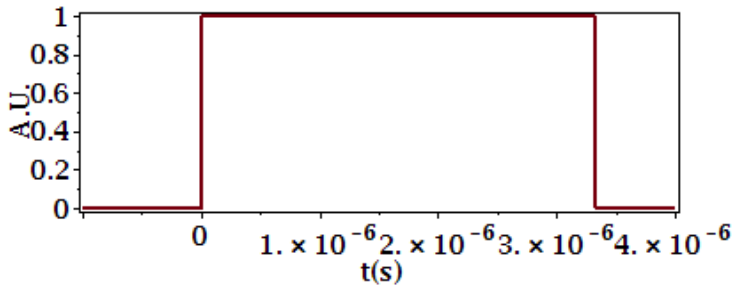

Figure 21 Ideal pressure response for square absorber

A plot of $y_{ideal}(t)$ for an exponential decay absorber with $l = 0.005\,(\text{m}),\ c_s = 1500(\text{m/s}),\ a = 200$ is shown in Figure 22.

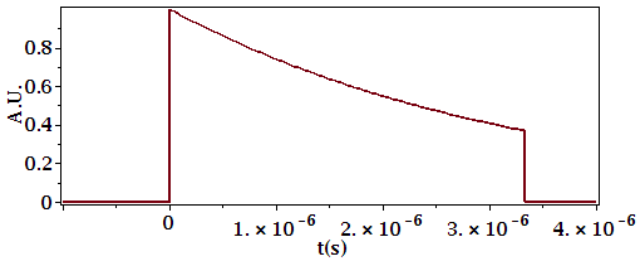

Figure 22 Ideal pressure response for exponential decay absorber

In order to calculate the error between $y_{ideal}(t)$ and $y_s(t)$ after the receiver-filter, we sampled 331 points between $0.03(\mu s)$ and $3.33(\mu s)$ with uniform spacing $0.01(\mu s)$. The equation for calculating the maximum error is given by

$$Err|_{\max} = \max\left|\frac{y_s(t_i) - y_{ideal}(t_i)}{y_{ideal}(t_i)}\right| \qquad i = 1..N \tag{3.119}$$

where *N* is the number of sampling points. In this case, *N* was 331 points.

The equation for calculating the average error is given by

$$Err|_{average} = \frac{1}{N}\sum_{i=1}^{N}\left|\frac{y_s(t_i) - y_{ideal}(t_i)}{y_{ideal}(t_i)}\right| \tag{3.120}$$

Equation (3.119) and equation (3.120) are used to calculate the errors in the simulations shown in Chapter 5.

4 Signal to Noise Ratio

In this section, the expressions for the Signal-to-Noise Ratio (SNR) of the photoacoustic response assuming a bandlimited absorber model and a square shape absorber model will be derived in closed form. As shown in previous sections, the temporal Fourier transform of the pressure response is given by

$$\tilde{p}(z,\omega) = \tilde{G}(z,\omega)\tilde{I}(\omega) \tag{4.1}$$

where

$$\tilde{G}(z,\omega) = \frac{p_0}{2c_s}\begin{cases} \hat{A}(-k)e^{-ikz} & z>0 \\ \hat{A}(k)e^{ikz} & z<0 \end{cases} \tag{4.2}$$

The exponential $e^{-ikz} = e^{-i\omega\frac{z}{c_s}}$ and $e^{ikz} = e^{i\omega\frac{z}{c_s}}$ factors merely represent a time delay without distortion (in other words, a propagating wave), which do not affect the SNR calculation.

The output of receiver-filter is

$$y(z,t) = y_s(z,t) + y_n(t) \tag{4.3}$$

where

$$\begin{aligned} & y_s(z,t) = r(t) * p(z,t) = r(t) * g(z,t) * I(t) \\ \text{or} \quad & \tilde{y}_s(z,\omega) = \tilde{R}(\omega)\tilde{G}(z,\omega)\tilde{I}(\omega) \end{aligned} \tag{4.4}$$

and

$$\begin{aligned} & y_n(t) = r(t) * n(t) \\ \text{or} \quad & \tilde{y}_n(\omega) = \tilde{R}(\omega)\tilde{S}_{nn}(\omega) \end{aligned} \tag{4.5}$$

The maximum signal to noise ratio (SNR) at the output of the receiver-filter occurs at a specific time t_0. The SNR at time t_0 is defined as

$$\left(\frac{S}{N}\right)_{t_0} = \frac{\left|y_s(z,t_0)\right|^2}{E\left|y_n(t_0)\right|^2} \tag{4.6}$$

where $\left|y_s(z,t_0)\right|^2$ is the photoacoustic signal power at time t_0, and $E\left|y_n(t_0)\right|^2$ is

the expectation of noise power at time t_0.

In this thesis, the simplest case will be considered where the noise is additive white Gaussian noise with a two-sided power spectral density $S_{nn}(\omega)=\frac{N_0}{2}$. Substituting equation (4.4) and (4.5) into (4.6), it follows that

$$SNR=\frac{\frac{1}{4\pi^2}\left|\int_{-\infty}^{\infty}\tilde{R}(\omega)\tilde{G}(z,\omega)\tilde{I}(\omega)e^{i\omega t_0}d\omega\right|^2}{\frac{N_0}{4\pi}\int_{-\infty}^{\infty}\left|\tilde{R}(\omega)\right|^2 d\omega} \tag{4.7}$$

Suppose the receiver filter is implemented as a matched filter so that the transfer function of the matched-filter is given by

$$\tilde{R}(\omega)=k\tilde{I}^*(\omega)e^{-i\omega t_0} \tag{4.8}$$

for some constant *k*. Then, the expression for SNR becomes

$$\begin{aligned} SNR&=\frac{\frac{1}{4\pi^2}\left|\int_{-\infty}^{\infty}k\tilde{I}^*(\omega)e^{-i\omega t_0}\tilde{G}(z,\omega)\tilde{I}(\omega)e^{i\omega t_0}d\omega\right|^2}{\frac{N_0}{4\pi}\int_{-\infty}^{\infty}\left|k\tilde{I}^*(\omega)e^{-i\omega t_0}\right|^2 d\omega} \\ &=\frac{1}{\pi N_0}\frac{\left|\int_{-\infty}^{\infty}\tilde{I}^*(\omega)\tilde{I}(\omega)\tilde{G}(z,\omega)d\omega\right|^2}{\int_{-\infty}^{\infty}\left|\tilde{I}^*(\omega)\right|^2 d\omega} \end{aligned} \tag{4.9}$$

For equation (4.9), suppose that $\tilde{I}(\omega)$ is the temporal Fourier transform of the chirp

$$I(\mathrm{t})=rect\left(\frac{t}{T}\right)\cos\left(\omega_0 t+\frac{\pi\Delta t^2}{T}\right) \tag{4.10}$$

Now take the rectangular approximation for the spectrum of the chirp from [50] as

$$\left|\tilde{I}^*(\omega)\right|^2=\tilde{I}^*(\omega)\tilde{I}(\omega)\approx\frac{T}{4\Delta}\quad\text{for }\omega_0-\frac{\Delta}{2}\le\omega\le\omega_0+\frac{\Delta}{2} \tag{4.11}$$

where $\omega_0=2\pi f_0$ is the center frequency of the chirp. Then, it follows that

$$SNR = \frac{1}{\pi N_0} \frac{\left| \int_{f_{LL}}^{f_{UL}} \frac{T}{4\Delta} \tilde{G}(z,\omega) d\omega \right|^2}{\int_{\omega_0 - \frac{\Delta}{2}}^{\omega_0 + \frac{\Delta}{2}} \frac{T}{4\Delta} d\omega} \qquad (4.12)$$

$$= \frac{1}{\pi N_0} \frac{T}{4\Delta^2} \left| \int_{f_{LL}}^{f_{UL}} \tilde{G}(z,\omega) d\omega \right|^2$$

where f_{UL} and f_{LL} represent the integration upper limit and lower limit, respectively. Substituting equation (4.2) without the time delay factor (propagating wave), it follows that

$$SNR = \frac{1}{\pi N_0} \frac{p_0^2 T}{16 c_s^2 \Delta^2} \begin{cases} \left| \int_{f_{LL}}^{f_{UL}} \hat{A}(-k) d\omega \right|^2 & z > 0 \\ \left| \int_{f_{LL}}^{f_{UL}} \hat{A}(k) d\omega \right|^2 & z < 0 \end{cases} \qquad (4.13)$$

Equation (4.13) clearly shows that the SNR is (i) directly proportional to the chirp duration so that a longer duration implies a higher SNR (ii) inversely proportional to the chirp sweep so that a longer sweep implies a smaller SNR and (iii) proportional to the absorber spectrum that lies within the frequency interval bounded by f_{UL} and f_{LL}. In the next subsections, specific examples of the absorber are considered to enable a further analysis of equation (4.13).

4.1 Bandlimited Absorber

Now consider the simple case where the absorber has a finite, flat spatial spectrum. This is a simple approximation to a band-limited absorber. In this case,

$$\hat{A}(\omega) = \begin{cases} A_0 & |\omega| \le \frac{\Delta_a}{2} \\ 0 & otherwise \end{cases} \qquad (4.14)$$

The absorber is considered as a square function in the spatial frequency domain.

Although this kind of absorber does not exist in reality, it is helpful in analyzing the implications of bandlimitedness in the absorber on the SNR trend. For the condition $z < 0$, the SNR becomes

$$SNR = \frac{p_0^2 T}{16\pi N_0 c_s^2 \Delta^2} \begin{cases} \left| \int_{f_{LL}}^{f_{UL}} A_0 d\omega \right|^2 & |\omega| \le \frac{\Delta_a}{2} \\ 0 & otherwise \end{cases}$$
$$= \frac{TC}{\Delta^2} \begin{cases} \left| \int_{f_{LL}}^{f_{UL}} 1 df \right|^2 & |\omega| \le \frac{\Delta_a}{2} \\ 0 & otherwise \end{cases} \quad (4.15)$$

where $C = \frac{p_0^2 A_0^2}{16\pi N_0 c_s^2}$ is constant.

In determining the upper limit and lower limit, three different possibilities are considered. Case 1: the chirp bandwidth is equal to the absorber bandwidth $\Delta = \Delta_a$; Case 2: the chirp bandwidth is smaller than the absorber bandwidth $\Delta < \Delta_a$; Case 3: the chirp bandwidth is bigger than the absorber bandwidth $\Delta > \Delta_a$.

4.1.1 Case 1 – chirp bandwidth equal to absorber bandwidth

It is assumed that the absorber frequency content is fixed with a bandwidth Δ_a and centered at fa_0. The integration in equation (4.15) only has a nonzero value when the chirp spectrum overlaps the absorber spectrum. The upper limit f_{UL} and lower limit f_{LL} will be different according to different overlapping conditions. As shown in Figure 23 A) –E), the chirp gradually sweeps through different frequency ranges from the left of the absorber spectrum to the right. The red rectangle represents the chirp frequency content, and the black rectangle is the absorber frequency content. The overlapped range is shaded in the figure. The integration upper limit f_{UL} and lower

limit f_{LL} will be the right and left edges of the shaded area, respectively.

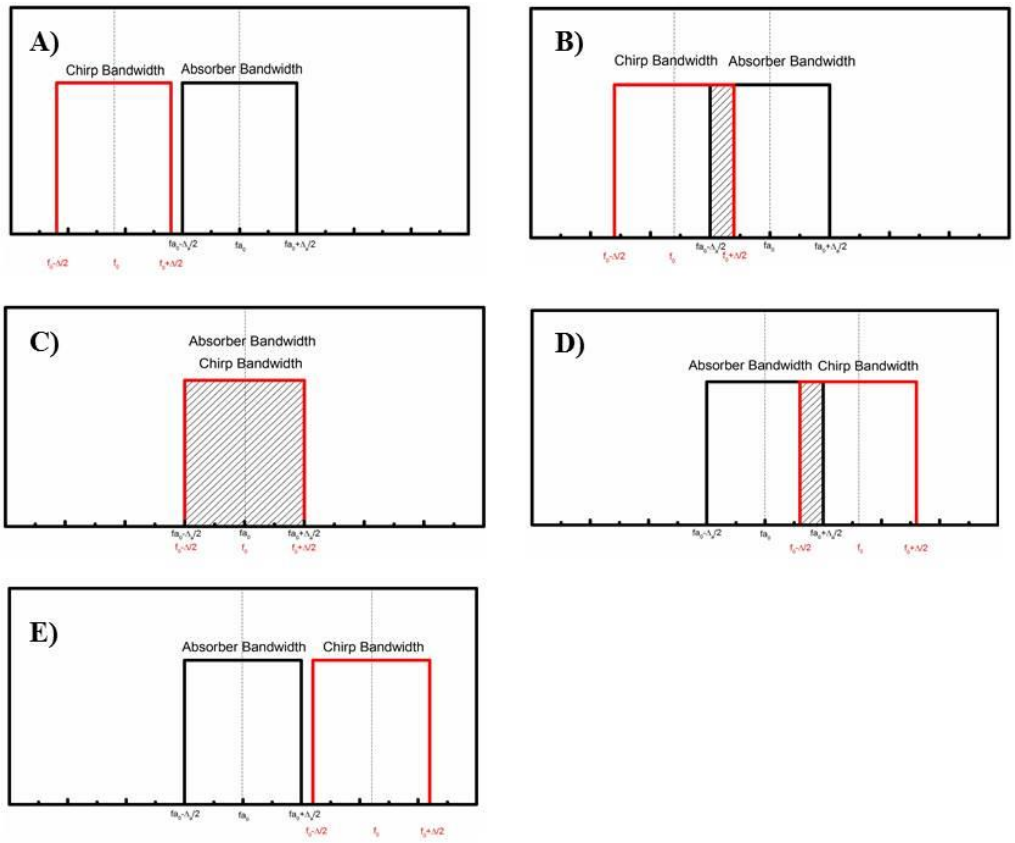

Figure 23 Different chirp sweeping conditions for $\Delta = \Delta_a$

In Figure 23, A) and E) do not have an overlapping area. Hence, the SNR will be 0. For Figure 23 B), equation (4.15) becomes

$$SNR = \frac{TC}{\Delta^2}\left|\int_{fa_0-\frac{\Delta_a}{2}}^{f_0+\frac{\Delta}{2}} 1df\right|^2 \tag{4.16}$$

When Δ and Δ_a are completely overlapped with each other, as shown in Figure 23 C), the SNR will be maximized as

$$SNR = \frac{TC}{\Delta^2}\left|\int_{f_0-\frac{\Delta}{2}}^{f_0+\frac{\Delta}{2}} 1df\right|^2 = TC \tag{4.17}$$

For Figure 23 D), equation (4.15) becomes

$$SNR = \frac{TC}{\Delta^2}\left|\int_{f_0-\frac{\Delta}{2}}^{fa_0+\frac{\Delta_a}{2}} 1df\right|^2 \tag{4.18}$$

4.1.2 Case 2 - chirp bandwidth smaller than absorber bandwidth

When the chirp bandwidth is smaller than the absorber bandwidth, $\Delta < \Delta_a$, the trend in the SNR will be slightly different from the case where $\Delta = \Delta_a$. As shown in Figure 24, all the overlapping conditions are similar to the $\Delta = \Delta_a$ case, except graph C).

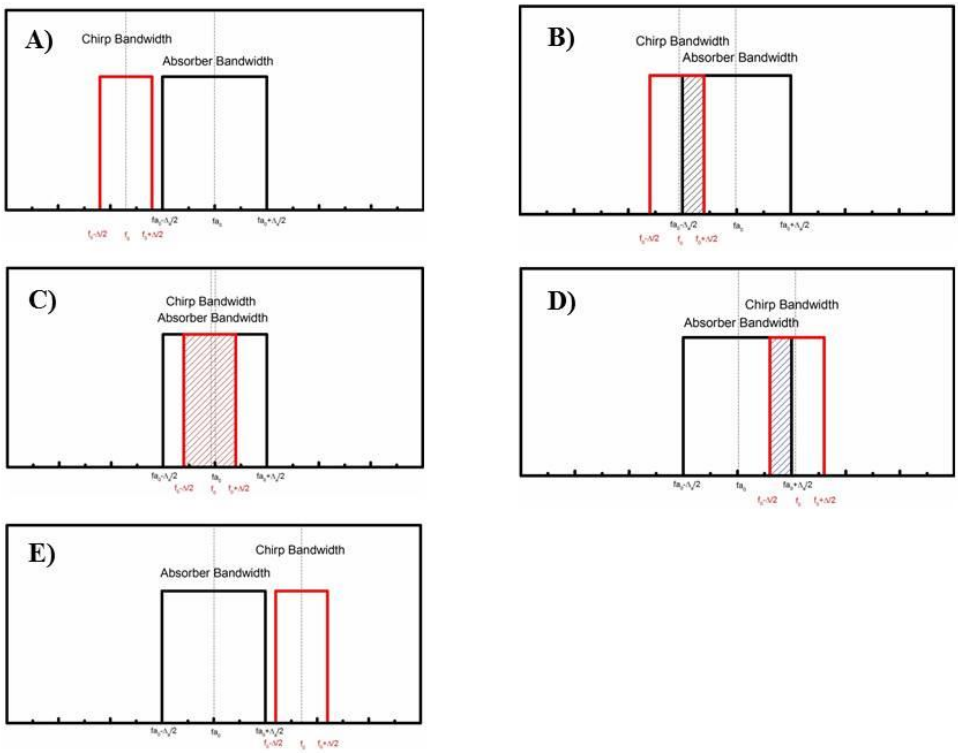

Figure 24 Different chirp sweeping conditions for $\Delta < \Delta_a$

For the overlapping condition shown in Figure 24 C), the integration upper limit and lower limit are both the edges of the chirp sweep. This condition gives the maximum SNR under the case $\Delta < \Delta_a$. The SNR will be given by

$$SNR = \frac{TC}{\Delta^2}\left|\int_{f_0-\frac{\Delta}{2}}^{f_0+\frac{\Delta}{2}} 1df\right|^2 = TC \tag{4.19}$$

Figure 24 A) and E) do not have an overlapping area, therefore the SNR will be 0. Figure 24 B) has the same overlapping condition with Figure 23 B), the SNR is shown in equation (4.16). Figure 24 D) has the same overlapping condition with Figure 23 D), hence the SNR is given by equation (4.18).

4.1.3 Case 3 - chirp bandwidth bigger than absorber bandwidth

When the chirp bandwidth is bigger than the absorber bandwidth, $\Delta > \Delta_a$, the trend in the SNR will still be similar with the case where $\Delta = \Delta_a$. As shown in Figure 25, all the overlapping conditions are similar to the $\Delta = \Delta_a$ case, except for graph C).

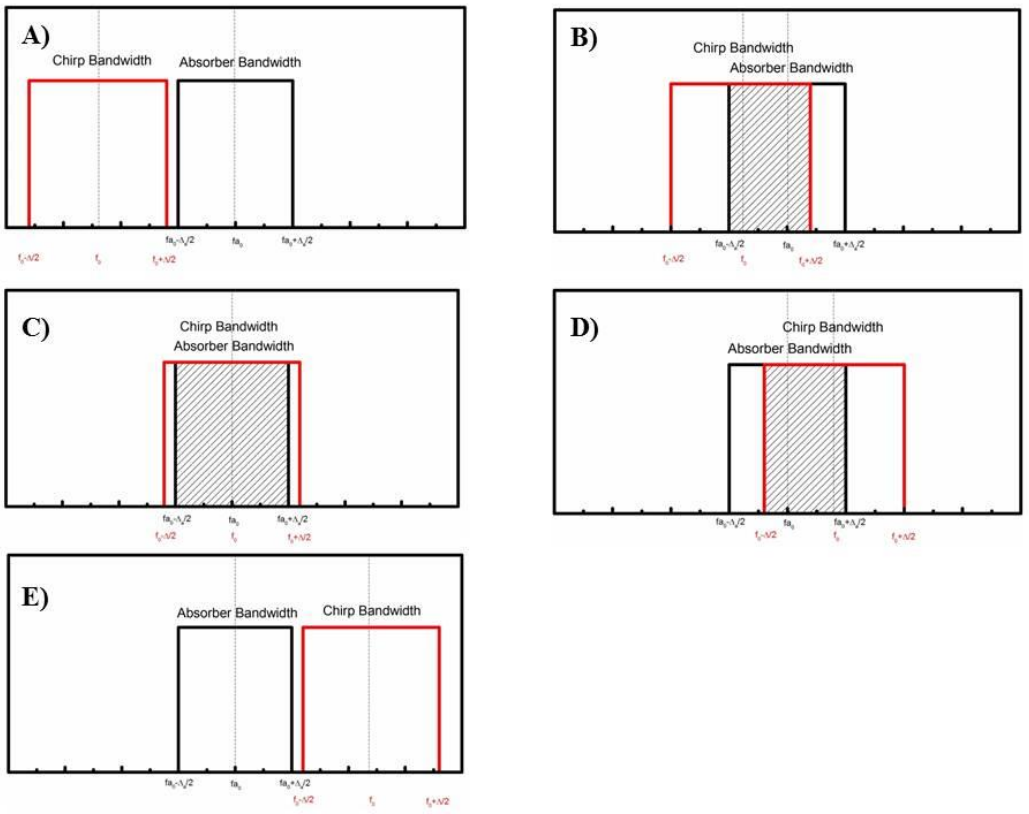

Figure 25 Different chirp sweeping conditions $\Delta > \Delta_a$

For the overlapping condition shown in Figure 25 C), the integration upper limit and lower limit are both the edges of the absorber frequency content. This condition gives the maximum SNR under the case $\Delta > \Delta_a$. The SNR will be given by

$$SNR = \frac{TC}{\Delta^2}\left|\int_{fa_0-\frac{\Delta_a}{2}}^{fa_0+\frac{\Delta_a}{2}} 1 df\right|^2 = TC\frac{\Delta_a^2}{\Delta^2} \tag{4.20}$$

In equation (4.20), since it is assumed in this case that $\Delta > \Delta_a$, then $\frac{\Delta_a^2}{\Delta^2} < 1$ and the SNR is smaller than for the cases where the chirp sweep was equal to or smaller than the absorber bandwidth. Hence, interestingly the result follows that making the chirp bandwidth larger than necessary only serves to reduce the SNR.

Figure 25 A) and E) do not have overlapping area, hence the SNR will be 0. Figure 25 B) has the same overlapping condition with Figure 23 B), so the SNR is given by equation (4.16). Figure 25 D) has the same overlapping condition as with Figure 23 D), so the SNR is given by equation(4.18).

4.1.4 The Effect of Chirp Bandwidth

Consider the case where the chirp center frequency is fixed at the center frequency of the absorber at $f_0 = 0$, and the absorber frequency content Δ_a is constant. The following section will discuss the SNR's relation with the chirp bandwidth Δ.

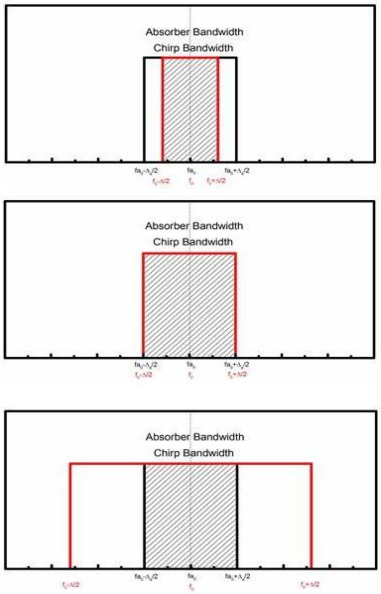

Figure 26 Absorber frequency content remains constant

Figure 26 shows the relation of the chirp sweeping range and the absorber frequency range. From top to bottom of Figure 26, the absorber frequency content remains constant, shown as the black square, but the chirp sweeping area becomes larger and larger, as represented by the red box. When the chirp sweeping range increases, the overlapping area will also increase until $\Delta = \Delta_a$. After that, the overlapping area remains constant as the chirp bandwidth increases. The SNR is

$$SNR = \frac{TC}{\Delta^2} \times \left(Overlapping\ Bandwidth \right)^2 \tag{4.21}$$

As long as $\Delta < \Delta_a$, SNR will be constant and has a maximum value given by

$$SNR_{\max} = \frac{TC}{\Delta^2} \times \left(\Delta \right)^2 = TC \tag{4.22}$$

After this period, SNR will *decrease* due to the constant overlapping area and increasing Δ in the denominator. The expression for SNR will then be given by

$$SNR = \frac{TC}{\Delta^2} \times \left(\Delta_a \right)^2 \tag{4.23}$$

4.2 Square Function Absorber in Space

In this section, the SNR for an absorber that is a square function in space will be considered. For a square absorber in space, the absorber is a sinc function in the frequency domain. In space, the absorber can be modeled as

$$A(z)=\begin{cases} a & |z|<\dfrac{l}{2} \\ 0 & |z|>\dfrac{l}{2} \end{cases} \tag{4.24}$$

where a is a constant that indicated the height of the 'step' and l is the width of the absorber. The transfer function for this kind of absorber is given by

$$\tilde{G}(z,\omega)=\frac{p_0 a}{2i\omega}\begin{cases} e^{i\frac{\omega}{c_s}\left(z+\frac{l}{2}\right)}-e^{i\frac{\omega}{c_s}\left(z-\frac{l}{2}\right)} & z<-l/2 \\ -e^{-i\frac{\omega}{c_s}\left(z+\frac{l}{2}\right)}+e^{-i\frac{\omega}{c_s}\left(z-\frac{l}{2}\right)} & z>l/2 \end{cases} \tag{4.25}$$

Similar to the prior simplification, the exponential factor $e^{i\omega\frac{z}{c_s}}$ only represents a propagating wave, which can be neglected. Substituting into equation (4.12), gives

$$\begin{aligned} SNR &= \frac{1}{\pi N_0}\frac{T}{4\Delta^2}\left|\int_{f_0-\frac{\Delta}{2}}^{f_0+\frac{\Delta}{2}}\tilde{G}(z,\omega)d\omega\right|^2 \\ &= \frac{1}{\pi N_0}\frac{Tp_0^2a^2}{16\Delta^2}\left|\int_{f_0-\frac{\Delta}{2}}^{f_0+\frac{\Delta}{2}}\frac{e^{i\omega\frac{l}{2c_s}}-e^{-i\omega\frac{l}{2c_s}}}{i\omega}d\omega\right|^2 \\ &= \frac{TC}{\Delta^2}\left|\int_{f_0-\frac{\Delta}{2}}^{f_0+\frac{\Delta}{2}}\frac{e^{i\omega\frac{l}{2c_s}}-e^{-i\omega\frac{l}{2c_s}}}{i\omega}d\omega\right|^2 \end{aligned} \tag{4.26}$$

where $C=\dfrac{p_0^2a^2}{16\pi N_0}$ is a constant scaling factor. The upper limit and lower limit of the integral are now fixed to $f_0+\dfrac{\Delta}{2}$ and $f_0-\dfrac{\Delta}{2}$, which belong to the edges of the chirp sweep, because the total frequency content of absorber ranges from $-\infty$ to ∞. The

frequency content of the absorber $\frac{e^{i\omega\frac{l}{2c_s}}-e^{-i\omega\frac{l}{2c_s}}}{i\omega}$ inside the integral is a sinc function as shown in Figure 27, where the first zero crossing is given by $2\pi c_s / l$. Hence, c_s / l (the inverse of the transit time through the absorber) controls the width of the main lobe of the sinc, which in turn determines which frequency range the majority of the energy of the absorber is located. The parameters used for plotting Figure 27 are $l = 0.005(\text{m}), c_s = 1500(\text{m/s})$.

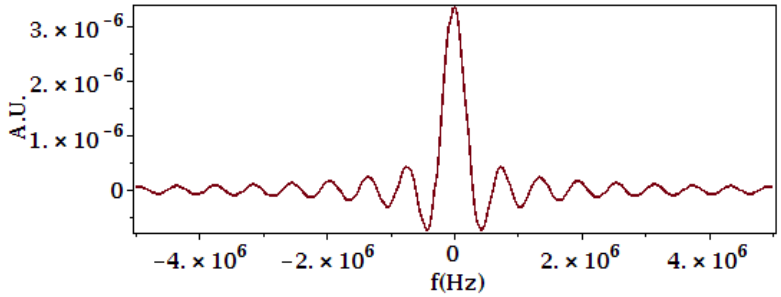

Figure 27 Frequency content of square absorber

As can be seen in Figure 27, most of the energy of the sinc is concentrated around the zero frequency, with the bulk of the energy contained in the main lobe of the sinc function. The overall trend of SNR will still be similar to a bandlimited absorber, in the sense that the sinc can be considered "somewhat" bandlimited with the band limit defined by the size of the main lobe of the sinc, which is in turn determined by c_s / l, the inverse of the transit time through the absorber. Therefore, smaller absorber will have smaller transit times and hence larger main lobes in their frequency domain sinc. Hence, larger chirp sweeps will be required to 'cover' the bandwidth of a smaller absorber. Detailed simulation results are shown in the following chapter.

5 Output of the Receiver-Filter - Resolution and SNR

This chapter shows several simulations of the signal at the output of the receiver-filter. The square and exponential decay absorbers are modeled with parameter $l = 0.005\,(\mathrm{m})$. The transducer is assumed at position $z = -0.03\,(\mathrm{m})$. The exponential decay absorber is assumed with an exponential decay factor $a = 200\,(\mathrm{m}^{-1})$. The speed of sound in the scattering material and absorber are assumed to be the same, $c_s = 1500\,(\mathrm{m/s})$. The values of parameters l, z, c_s, a for absorbers are taken to be close or equal to the experimental parameters used in recent researches [13], [18], [19], [41]. The initial pressure p_0, which merely serves as a scaling factor for simulations of the response, is arbitrarily chosen in Arbitrary Units (AU) as $p_0 = 10^{10}\,(\mathrm{A.U.})$.

5.1 Effect of chirp parameters effect on absorber profilometric information and SNR

In this section, several important parameters of the incident chirp will be discussed. This will provide a guide on how to choose the proper parameters of the chirp for the goal of obtaining a pressure response that will resemble the absorber shape (impulse response), or in other words, a better resolution (a response that better reproduces what would be obtained with an input Dirac delta pulse). Furthermore, the chirp parameters' effects on the SNR at the output of the receiver-filter will also be considered.

5.1.1 Effect of Chirp duration T

Chirp duration is one of the most important parameters which define a chirp. As discussed earlier, the chirp compression ratio is given by $\frac{\Delta T}{2}$. The compressed pulse duration is $\frac{2}{\Delta}$, which shall be referred to as the effective pulse duration.

First, several chirp parameter sets were tested with only chirp duration T changing. The parameters are shown in Table 1.

Table 1 Parameter Table with T changing

Chirp parameter sets No.	**Chirp duration T (s)**	**Chirp bandwidth Δ (Hz)**	**Chirp center frequency f_0 (Hz)**
1	1×10^{-2}	3×10^{6}	0
2	1×10^{-3}	3×10^{6}	0
3	1×10^{-4}	3×10^{6}	0
4	1×10^{-5}	3×10^{6}	0

Since the bandwidth remains unchanged, the effective pulse duration $\frac{2}{\Delta}$ does not change, so it would be expected that there should not be any difference in resolution between the simulation results using these parameters. However, the signal to noise ratio SNR is proportional to chirp duration. So, it would be expected that the SNR should decrease from parameter set 1 to 4 as *T* decreases. The simulation results are shown in Table 2. The SNR is obtained with equation (4.26), the maximum error and average error is calculated using equation (3.119) and (3.120) respectively.

The same SNR and resolution calculation processes are taken for all the simulations

in this chapter.

Table 2 Chirp duration effect

Data No. & Chirp duration	**Square absorber pressure response signal after filtering**	**Exponential decay absorber pressure response signal after filtering**	**SNR**	**Maximum Error (%)**	**Average Error (%)**
1 $T=1\times10^{-2}$ (s)	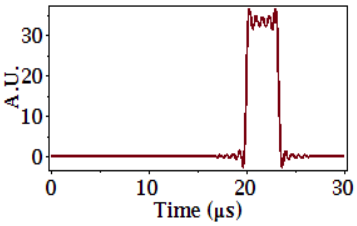	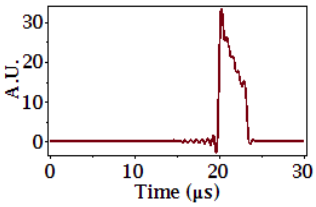	1.2×10^{10}	48	7
2 $T=1\times10^{-3}$ (s)	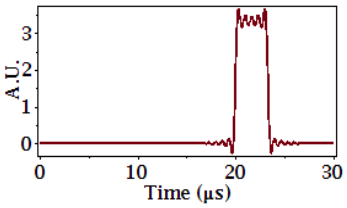	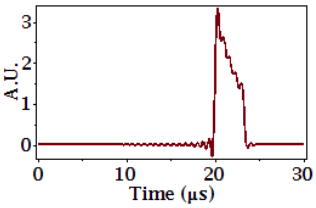	1.2×10^{9}	48	7
3 $T=1\times10^{-4}$ (s)	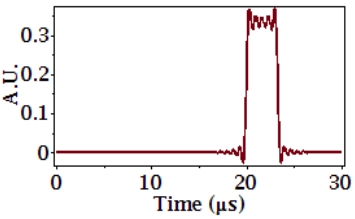	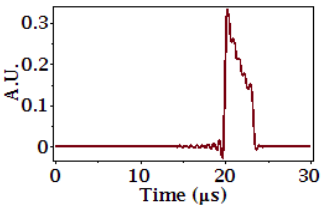	1.2×10^{8}	48	7
4 $T=1\times10^{-5}$ (s)	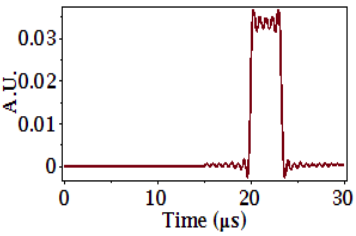	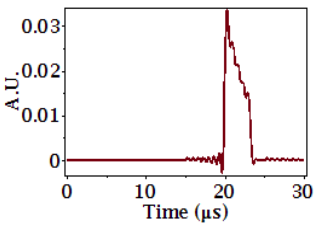	1.2×10^{7}	48	7

As expected, changing only the chirp duration T does not affect the shape of the pressure response, and so the maximum errors are the same for all 4 sets of data. As can be seen from the graphs, the only difference is the magnitude of the response. The larger T will give a higher magnitude, because the impulse chirp contains more energy. As a result of the energy difference, the larger chirp duration gives a better SNR, as shown in Table 2.

Second, several sets of parameters were tested with constant time-bandwidth product $T\Delta$. In this case, as T gets larger, Δ becomes smaller, but the time-bandwidth product (compression ratio) is held constant. Hence, the effective pulse duration will be increased, which is expected to give a pressure response that may blur the shape of the absorber, or in other words, a worse resolution. The parameter sets are shown in Table 3.

Table 3 Parameter Table with effective pulse duration changing

Parameter sets No.	**Chirp duration T (s)**	**Bandwidth Δ (Hz)**	**Effective pulse duration (s)**	**Chirp center frequency f_0 (Hz)**
1	1×10^{-5}	3×10^{7}	6.67×10^{-8}	0
2	1×10^{-4}	3×10^{6}	6.67×10^{-7}	0
3	1×10^{-3}	3×10^{5}	6.67×10^{-6}	0
4	1×10^{-2}	3×10^{4}	6.67×10^{-5}	0

The simulation results are shown in Table 4.

Table 4 Chirp effective duration effect

Data No. & Effective duration	Square absorber pressure response signal after filtering	Exponential decay absorber pressure response signal after filtering	SNR	Maximum Error (%)	Average Error (%)
1 $6.67\times10^{-8}\,(s)$	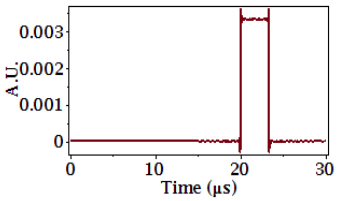	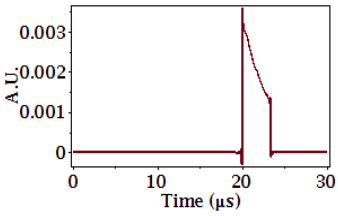	8.92×10^{-5}	37	5
2 $6.67\times10^{-7}\,(s)$	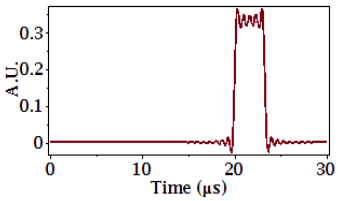	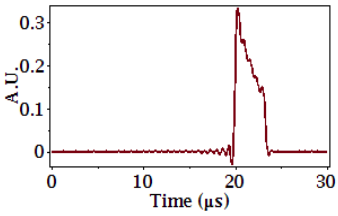	8.92	48	7
3 $6.67\times10^{-6}\,(s)$	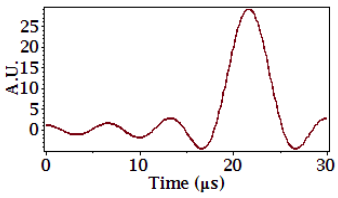	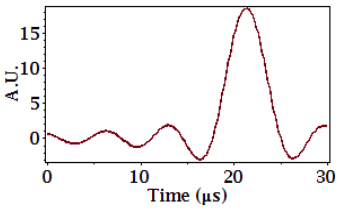	3.59×10^{5}	54	19
4 $6.67\times10^{-5}\,(s)$	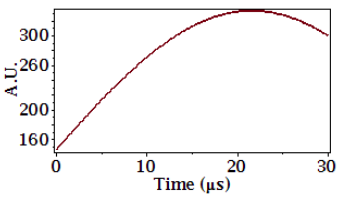	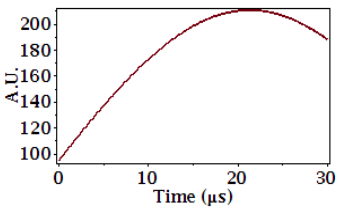	2.83×10^{11}	93	90

As can be seen from Table 4, the pressure response blurs the shape of the absorber when the effective pulse duration became large and can no longer be considered ‘short enough’ to represent a short pulse. When the maximum error goes beyond around 50 percent, the shape of the absorber is completed lost from the response. However, losing resolution does not imply losing SNR. In fact, the SNR increases dramatically as Δ becomes smaller and T becomes larger.

5.1.2 Effect of Frequency

5.1.2.1 Effect of chirp sweep

In this subsection, the effects of the chirp frequency parameters on the pressure response are examined. The parameter sets that were used for the simulations are listed in Table 5. The bandwidth (chirp sweep) Δ is the only changing parameter, and the chirp duration is kept constant.

Table 5 Parameter table with Δ changing

Parameter No.	Chirp duration T (s)	Bandwidth Δ (Hz)	Chirp center frequency f_0 (Hz)
1	1×10^{-3}	3×10^{9}	0
2	1×10^{-3}	3×10^{7}	0
3	1×10^{-3}	3×10^{6}	0
4	1×10^{-3}	3×10^{5}	0
5	1×10^{-3}	3×10^{4}	0

Simulation results are shown in Table 6.

Table 6 Chirp bandwidth effect

Data No. & Chirp bandwidth	Square absorber pressure response signal after filtering	Exponential decay absorber pressure response signal after filtering	SNR	Max Error (%)	Average Error (%)
1 $\Delta = 3\times10^{9}$ (Hz)	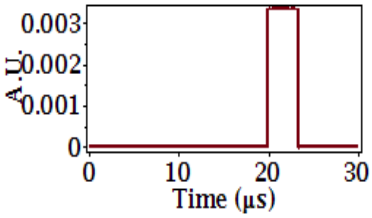	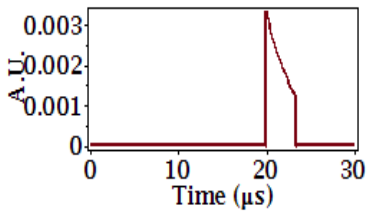	1111	5	5
2 $\Delta = 3\times10^{7}$ (Hz)	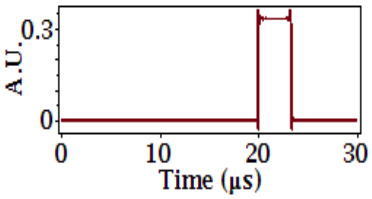	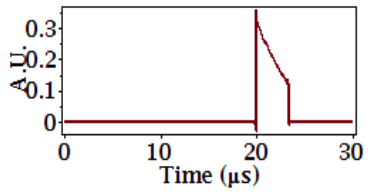	1.1×10^{7}	37	5
3 $\Delta = 3\times10^{6}$ (Hz)	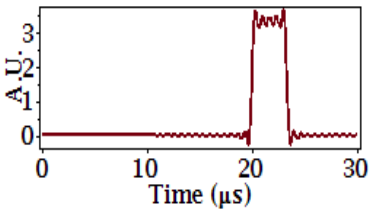	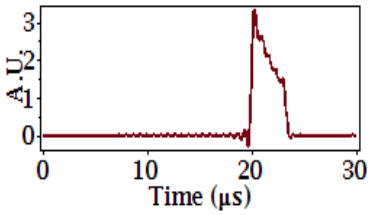	1.2×10^{9}	48	7
4 $\Delta = 3\times10^{5}$ (Hz)	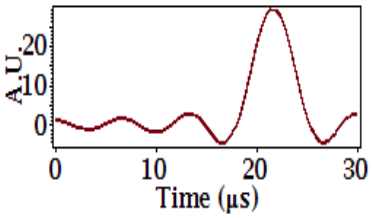	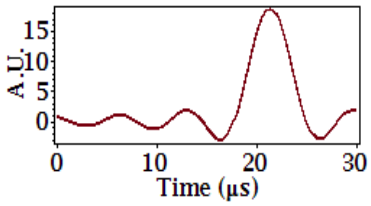	8.5×10^{10}	54	16
5 $\Delta = 3\times10^{4}$ (Hz)	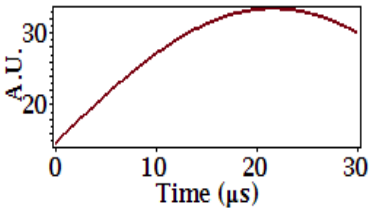	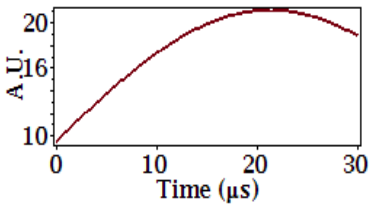	1.1×10^{11}	93	90

From Table 6, it can be observed that when Δ is big enough, such as the 1st parameter set, the pressure response resembles the absorber shape well. The resolution is good with a maximum error 5%. As the bandwidth Δ becomes smaller, the pressure response starts to lose the shape. This follows because the smaller bandwidth gives us

a longer effective pulse, since the effective pulse duration is given by $\frac{2}{\Delta}$. This result is consistent with the previous theory which states that a "fake" Dirac-Delta function input pulse will excite a pressure response which has the same shape with the absorber but the fake pulse needs to have a sufficiently short duration to resemble an effective Dirac-delta pulse. Hence, larger bandwidths are desirable in order to obtain smaller effective pulses and hence better resolutions. However, the larger bandwidth Δ will result in a lower SNR. So the parameters need to be chosen to obtain an acceptable resolution and not lose too much SNR.

5.1.2.2 Effect of chirp center frequency

The other important parameter which affects the pressure response is the choice of chirp center frequency f_0. Several parameter sets have been tested with all the parameters the same, except for f_0. To analyze the effect of center frequency, the parameters chosen for the next set of simulations are listed in Table 7.

Table 7 Parameter table with f_0 changing

Parameter No.	Chirp duration T (s)	Bandwidth Δ (Hz)	Chirp center frequency f_0 (Hz)
1	1×10^{-3}	3×10^{7}	-3×10^{7}
2	1×10^{-3}	3×10^{7}	-1×10^{7}
3	1×10^{-3}	3×10^{7}	0
4	1×10^{-3}	3×10^{7}	1×10^{7}
5	1×10^{-3}	3×10^{7}	3×10^{7}

The simulation results are shown in Table 8.

Table 8 Chirp center frequency effect

Data No. & Center frequency	Square absorber pressure response signal after filtering	Exponential decay absorber pressure response signal after filtering	SNR	Maximum Error (%)	Average Error (%)
1 $f_0 = -3\times10^7$ (Hz)	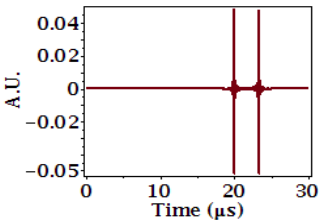	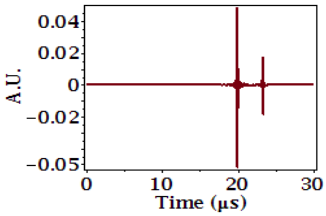	20.3	104	100
2 $f_0 = -1\times10^7$ (Hz)	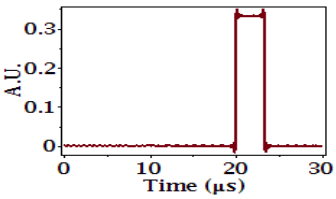	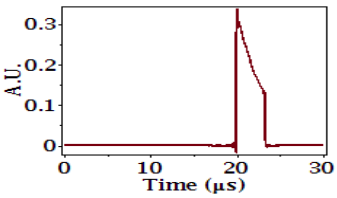	1.1×10^7	37	5
3 $f_0 = 0$ (Hz)	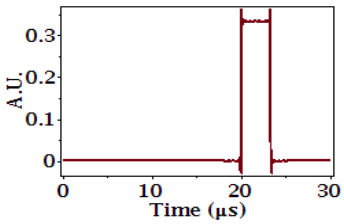	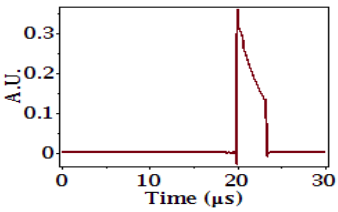	1.1×10^7	37	5
4 $f_0 = 1\times10^7$ (Hz)	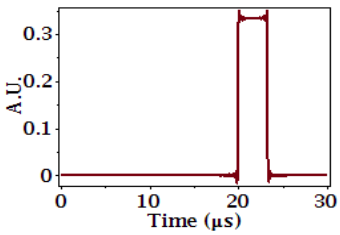	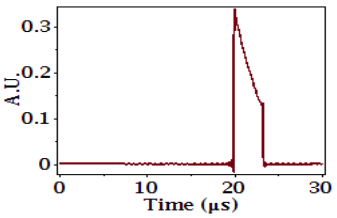	1.1×10^7	37	5
5 $f_0 = 3\times10^7$ (Hz)	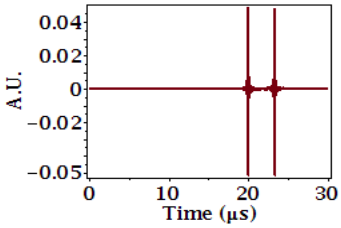	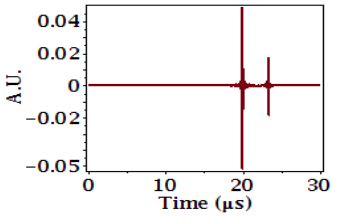	20.3	104	100

In Table 8, bandwidth used for all the plots are the same. The only difference is the center frequency. From parameter sets 1 to 5, the chirp is sweeping the same bandwidth but in a different frequency range (from the left to the right of the absorber frequency content). As can be seen from the plots, in order to obtain a pressure

response that resembles the absorber shape, choosing only a wide frequency bandwidth is not enough. The entire frequency sweep should be in a certain range. Choosing a sweep that gives a sufficiently small effective pulse duration via $\frac{2}{\Delta}$ does not yield good results if the center frequency puts the entire frequency range away from the spectrum of the absorber. In other words, the frequency sweep should cover as much frequency content of the absorber as it can. Designing the chirp so that the entire frequency range that is swept is away from the spectrum of the absorber may result in a sufficiently short compressed pulse, however the result will be poor resolution and poor SNR.

5.1.3 Conclusion

In this section, the effect of the parameters of the incident laser chirp have been analyzed for their effect on the photoacoustic signal at the output of the receiver-filter in terms of resolution and SNR.

Chirp duration T is one of the key parameters that need to be controlled. The chirps with larger T will generate a higher energy signal which will deliver a better SNR. However, a larger T will not give better resolution, and a longer duration chirp means more energy in the chirp which may be limited by safety regulations. The duration of chirp cannot be increased indefinitely.

The chirp frequency bandwidth Δ controls the duration of compressed pulse, when Δ becomes larger, the compressed effective pulse duration is shorter, which in turn gives a signal with a better resolution and a response that can better resemble the absorber shape (impulse response). However, according to equation (4.26) and the simulations above, the larger Δ gives a worse SNR. Hence, there needs to be a balance between resolution and SNR and this is highly affected by controlling the chirp sweep.

The center frequency f_0 is another important parameter. When the frequency bandwidth Δ is fixed, the chirp sweeping range should cover the most energy of the absorber. Under this condition, improved SNR and resolution can be obtained.

5.2 Signal to Noise Ratio Trends

The effect of chirp parameters on resolution and SNR have been investigated in the previous sections. However, the overall trend of the SNR is still not clear. In this section, another view of how SNR changes with different parameters will be examined.

5.2.1 Bandlimited Absorber

Although a true bandlimited absorber does not exist in reality, examining the implication of absorber bandlimitedness can help to obtain a rough picture about the trend in the SNR. Consider the bandlimited absorber shown in equation (4.14), the equation for SNR is given by

$$\begin{aligned} SNR &= \frac{p_0^2 T}{16\pi N_0 c_s^2 \Delta^2} \begin{cases} \left| \int_{f_{LL}}^{f_{UL}} A_0 d\omega \right|^2 & |\omega| \le \frac{\Delta_a}{2} \\ 0 & otherwise \end{cases} \\ &= \frac{TC}{\Delta^2} \begin{cases} \left| \int_{f_{LL}}^{f_{UL}} 1 df \right|^2 & |\omega| \le \frac{\Delta_a}{2} \\ 0 & otherwise \end{cases} \end{aligned} \tag{5.1}$$

where $C = \frac{p_0^2 A_0^2}{16\pi N_0 c_s^2}$ is a constant scaling factor which was chosen as an arbitrary value of $C = 10^{15}$ in the simulations.

5.2.1.1 Effect of Chirp sweep location

Figure 28 shows the three different cases as categorized in section 4.1. Figure 28 A) shows case 1, where the chirp bandwidth is equal to the absorber bandwidth, with parameters $\Delta = \Delta_a = 3\times10^5(\text{Hz}), T = 10^{-3}(\text{s})$. As shown in the corresponding case of Figure 23 A) to E), the chirp sweeps from left to right with center frequency f_0 moving from $-6\times10^5(\text{Hz})$ to $-6\times10^5(\text{Hz})$. The SNR first increases in accordance with the increasing overlapping area until the maximum value is obtained where Δ exactly matches Δ_a. Then, the SNR decreases because of the decreasing overlapping area.

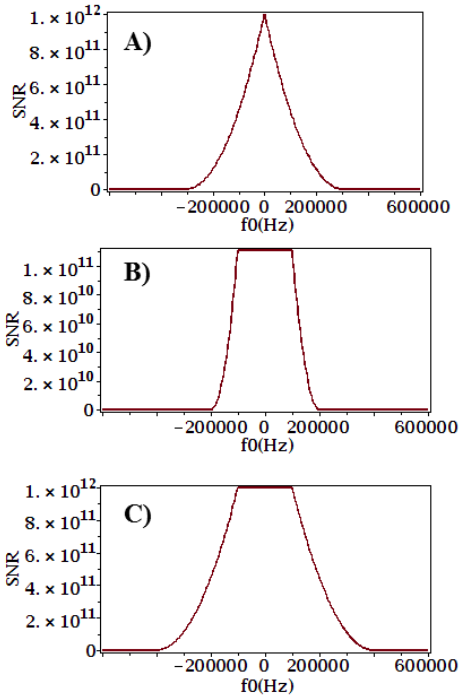

Figure 28 SNR of bandlimited absorber with chirp sweeping different frequency range A) $\Delta = \Delta_a = 3\times10^5(Hz)$***, chirp center frequency moving from*** $-6\times10^5(Hz)$ ***to*** $6\times10^5(Hz)$***; B)*** $\Delta = 3\times10^5(Hz), \Delta_a = 1\times10^5(Hz)$***, chirp center frequency moving from*** $-6\times10^5(Hz)$ ***to*** $6\times10^5(Hz)$***; C)*** $\Delta = 3\times10^5(Hz), \Delta_a = 5\times10^5(Hz)$***, chirp center frequency moving from*** $-6\times10^5(Hz)$ ***to*** $6\times10^5(Hz)$

Figure 28 B) shows case 3, where the chirp bandwidth is bigger than the absorber bandwidth, with parameters $\Delta = 3\times10^5\left(Hz\right), \Delta_a = 1\times10^5\left(Hz\right), T = 10^{-3}\left(s\right)$. As shown in Figure 25 A) to E), the chirp is sweeping from left to right with center frequency f_0 moving from $-6\times10^5(\text{Hz})$ to $-6\times10^5(\text{Hz})$. The SNR first increases according to the increasing overlapping area until the maximum value is reached where Δ_a is completely inside Δ and lasts for a certain period of frequency. Then, the SNR will decrease because of the decreasing overlapping area.

Figure 28 C) shows case 2, where the chirp bandwidth is smaller than the absorber bandwidth, with parameters $\Delta = 3\times10^5(\text{Hz}), \Delta_a = 5\times10^5, T = 10^{-3}(\text{s})$. As shown in Figure 24 A) to E), the chirp is sweeping from left to right with center frequency f_0 moving from $-6\times10^5(\text{Hz})$ to $-6\times10^5(\text{Hz})$. The SNR first increases according to the increasing overlapping area until the maximum value where Δ is completely inside Δ_a and lasts for a certain period of frequency. Then the SNR will decrease because the overlapping area decreases.

From Figure 28 A), B) and C), the conclusion can be drawn that in order to obtain a higher SNR, the chirp sweep must fit as much as possible within the absorber frequency content. Comparing the maximum SNR in Figure 28 A), B) and C), the maximum SNR will be determined by the minimum of Δ_a and Δ, $\min\left(\Delta, \Delta_a\right)$.

If $\Delta > \Delta_a$, the maximum SNR occurs when $f_0 = 0$ and is given by

$$SNR_{\max} = TC\frac{\Delta_a^2}{\Delta^2} \tag{5.2}$$

If $\Delta \le \Delta_a$, the maximum SNR occurs when $f_0 = 0$ and is given by

$$SNR_{\max} = TC \tag{5.3}$$

5.2.1.2 Effect of Chirp bandwidth on SNR

As discussed in Chapter 4, suppose that the absorber bandwidth remains constant and the chirp sweep is centered at $f_0 = 0$ where the absorber center frequency is also located. If the chirp bandwidth is increased, the SNR will be constant and maximized at first and then will decrease.

Figure 29 shows a simulation of the relation between SNR and chirp bandwidth. The parameters used in the simulation are given by $C = 10^{15}, T = 10^{-3}(\text{s})$ and $f_0 = fa_0 = 0, \Delta_a = 10^5(\text{Hz})$. The chirp bandwidth increases from 0 to 3×10^5 (Hz). The flat top in Figure 29 is when the chirp bandwidth is completely inside the absorber bandwidth, $\Delta \le \Delta_a$. The SNR will be given by $TC = 10^{15}$. When $\Delta > \Delta_a$, the overlapping area will be fixed to Δ_a no matter how Δ changes, so the SNR starts to drop as Δ increases.

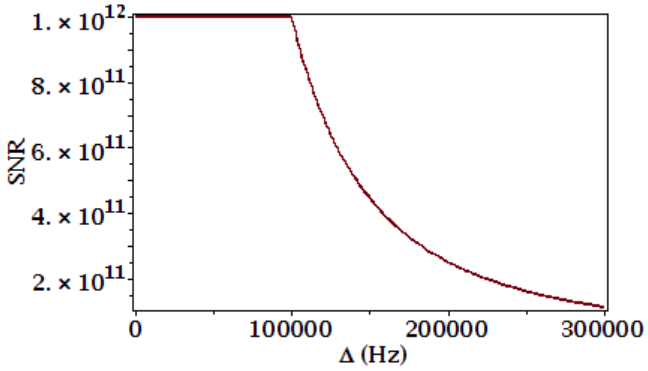

Figure 29 SNR vs. Chirp Bandwidth

5.2.2 Square Absorber

In this section, the SNR trends for a more realistic absorber, the square absorber will be examined.

5.2.2.1 Absorber Frequency Content

Before analyzing the SNR, the frequency content of the absorber must be examined. A square wave absorber in space is a sinc function in the spatial frequency domain. The translation from spatial frequency to frequency is done by the speed of sound c_s. The mathematical expression of a square wave absorber in the frequency domain is given by

$$\frac{\sin\left(\pi f \frac{l}{c_s}\right)}{\pi f} \tag{5.4}$$

A plot of equation (5.4) with parameters $l = 0.005(\text{m}),\ c_s = 1500(\text{m/s})$ is shown in Figure 30.

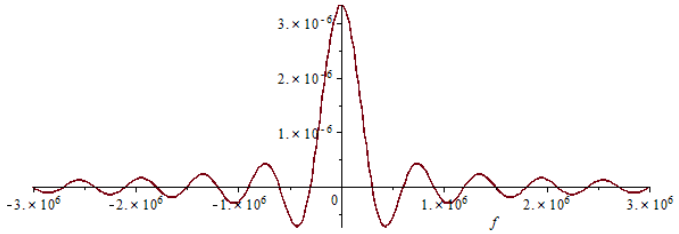

Figure 30 Square absorber in frequency domain

The energy spectrum of this absorber is

$$\left(\frac{\sin\left(\pi f \frac{l}{c_s}\right)}{\pi f}\right)^2 \tag{5.5}$$

as shown in Figure 31.

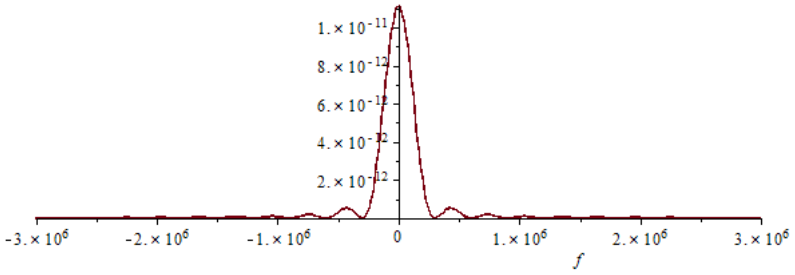

Figure 31 Energy spectrum of square absorber

We define the idea of energy concentration percentage as the percentage of the total energy of the sinc (which has energy at all frequencies) that is contained within the bandwidth $\left[-\Delta_a/2, \Delta_a/2\right]$. Mathematically, this can be written as

$$percentage = \frac{\int_{-\frac{\Delta_a}{2}}^{\frac{\Delta_a}{2}} \left(\frac{\sin\left(\pi f \frac{l}{c_s}\right)}{\pi f} \right)^2 df}{\int_{-\infty}^{\infty} \left(\frac{\sin\left(\pi f \frac{l}{c_s}\right)}{\pi f} \right)^2 df} = \frac{c_s}{l} \int_{-\frac{\Delta_a}{2}}^{\frac{\Delta_a}{2}} \left(\frac{\sin\left(\pi f \frac{l}{c_s}\right)}{\pi f} \right)^2 df \tag{5.6}$$

This approach allows us to determine what the frequency range needs to be to capture "most" of the energy of the absorber. Through equation (5.6), frequency ranges can be determined where the energy of the absorber is 95% concentrated or 99% concentrated. Specifically, 95% of the absorber energy is concentrated in the range given by $\Delta_a = 1.24\times10^6 \left(Hz\right)$ and 99% of the absorber energy is concentrated in the range $\Delta_a = 6.17\times10^6 \left(Hz\right)$. Hence, although the absorber is not strictly speaking bandlimited, band limits can be determined where 'most' of the energy is concentrated within and the idea of 'most' can easily be specified to any desired value.

5.2.2.2 Effect of Chirp Sweep Location

In section 4.2, it was predicted that the absorber which is a square function in space will have an SNR trend that is similar to that of a bandlimited absorber. In this section, simulations are presented to demonstrate this claim.

Figure 32 is a simulation plot of SNR as it changes with chirp center frequency f_0 while the other chirp parameters are given by $T = 10^{-3}(\text{s}), C = 10^{15}, l = 0.005\,(\text{m})$ $c_s = 1500(\text{m/s}),\ \Delta = 3\times10^6(\text{Hz})$. The chirp center frequency moves from $-3\times10^6(\text{Hz})$ to $3\times10^6(\text{Hz})$. As can be seen from the figure, the SNR first increases and remains around a constant value and then decreases with some oscillations. Figure 30 shows that most of the energy of the absorber concentrates in a certain range (approximately 97% energy concentrates in $-1\times10^6(\text{Hz})$ to $1\times10^6(\text{Hz})$) centered at 0 (Hz). The increase in SNR in Figure 32 before $-1\times10^6(\text{Hz})$ is because the chirp is approaching the absorber concentrated frequency range, the upper limit of the chirp sweeping range $f_0 + \frac{\Delta}{2}$ is inside the absorber concentrated frequency range. Between $-1\times10^6(\text{Hz})$ and $1\times10^6(\text{Hz})$, the SNR remains almost constant because the absorber's concentrated frequency range is smaller than the chirp bandwidth, similar to case 3 as discussed in Figure 25. Finally, the decrease in SNR is due to the decrease of overlapping areas of their spectrums.

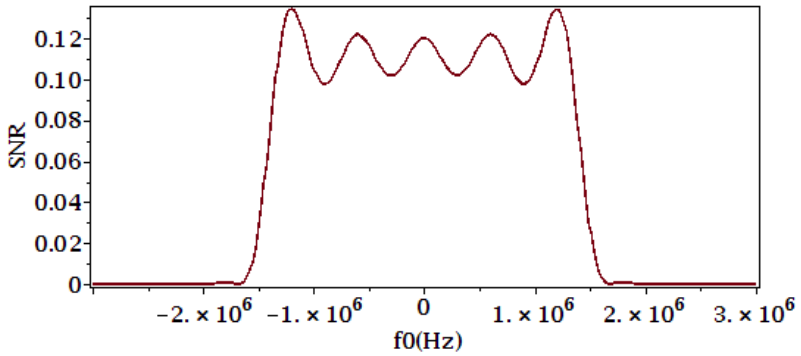

Figure 32 SNR changes with chirp center frequency

5.2.2.3 Effect of Chirp Bandwidth

Figure 33 is the simulation plot to show the relationship between the chirp bandwidth and SNR. Same as for the case of the bandlimited absorber, the chirp center frequency

remains at 0 (Hz), only the chirp bandwidth is the independent variable. The parameters used in this plot are $T = 10^{-3}(\text{s}), C = 10^{15}, l = 0.005(\text{m}), c = 1500(\text{m/s})$.

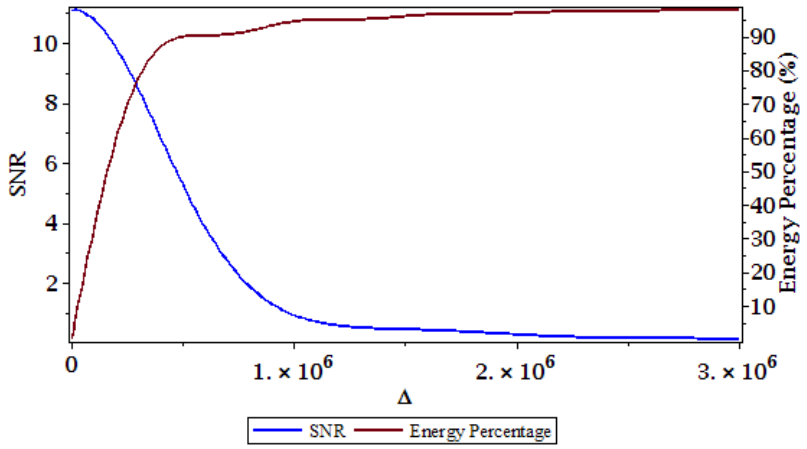

Figure 33 SNR vs. Chirp Bandwidth for square absorber

In Figure 33, the blue line represents the SNR, the red line represents the percentage of the absorber energy covered by the chirp sweep. As can be seen from Figure 33, the trend in SNR is similar to that in Figure 29 for the case of the bandlimited absorber, that is SNR decreases with increasing chirp bandwidth. There is no flat constant range in Figure 33, because the magnitude of the absorber frequency content is not constant in that range. In the SNR expression

$$SNR = \frac{TC}{\Delta^2} \times \left(Overlapping\ Area\right)^2 \tag{5.7}$$

the overlapping area squared, $\left(Overlapping\ Area\right)^2$, increases slower than the squared chirp bandwidth Δ^2. However, the decrease in SNR is relatively small up to a certain value of Δ. As Δ becomes too large, (beyond about 1×10^6 Hz in these simulations), increasing Δ will not deliver more energy quickly, but rather the Δ^2 in equation (5.7) still increases quickly. Hence, the SNR beyond that range becomes very small.

5.2.3 Conclusion

The key parameters of the chirp have very important effects on the SNR at the output of the receiver-filter. The center frequency determines the sweeping location. When the chirp bandwidth is fixed, putting the chirp center frequency at 0 frequency (or wherever the absorber bandwidth center frequency is located) gives the best SNR and a better resolution. When the chirp center frequency is fixed, it is necessary to manipulate the chirp bandwidth to cover most of the frequency range where the absorber energy is concentrated in order to obtain a better resolution. However, increasing the chirp bandwidth when detecting the square absorber will be costly in terms of a decrease in SNR. It is necessary to adjust the bandwidth to a certain value so that an acceptable resolution (absorber depth profile) can be obtained and at the same time not lose too much in SNR.

6 Comparison of Theory to Experimental Results

Telenkov and Mandelis [19] used the autocorrelated chirp to experimentally obtain pressure response signals. In this section, their experimental results will be compared to simulations using the theory developed in this thesis.

Telenkov and Mandelis used a sinusoidal chirp with the frequency sweep $500kHz \sim 2.5MHz$ which implies in simulations chirp parameters of $\Delta = 2\times10^6\,Hz,\ f_0 = 1.5\times10^6\,Hz$. They used a PVC absorber which is $5\ mm$ thick, being placed in clear water, which implies that l is $0.005\,m$. The absorption coefficient $\mu_a = 2cm^{-1}$ indicates a light absorption attenuation coefficient a for the exponential decay absorber in the simulations given by $a = 200$. The chirp duration is $T = 1\,ms$. Their transducer was placed at a distance of $3\,cm$ away from the absorber on the reflection side, hence in the simulations, the parameter $z = -0.03\,m$. The speed of sound in water is around $1500\ m/s$, and it is assumed that the speed of sound in scattering and absorbing material are similar (the variation of speed of sound in different tissue is less than 10% [51]). Hence, in the simulations, $c_s = 1500\ m/s$ was used.

The experimental pressure response they obtained is shown by line 1 in Figure 34. Line 2 and line 3 are responses of a square shaped chirp and a train of pulses, neither of which are considered in this thesis.

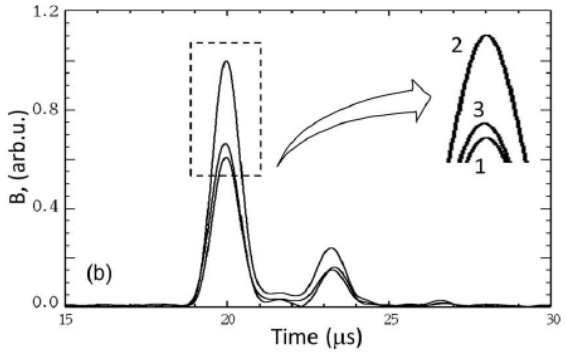

Figure 34 Experimental Pressure Response (Line 1) from [19]

The simulation of the pressure response using their parameters with the theory developed in this thesis is shown in Figure 35

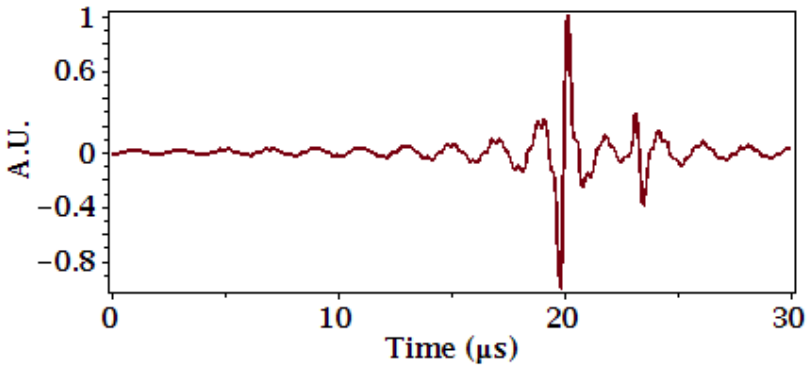

Figure 35 Simulation result of pressure response

As can be seen from Figure 34, the experimental result mainly contains two peaks. In Figure 35, the simulation also shows a pressure response which only has two peaks – these actually represent the two edges of the absorber. This follows because the frequency sweep only covers the high frequency part of the absorber spectrum. As discussed in the previous chapter, the chirp center frequency is too high so that the overlapping area between the chirp bandwidth and the absorber bandwidth is too small, resulting in a low resolution. In particular, only high frequency absorber features (the edges of the absorber) are detected since the frequency sweep is only over high frequencies.

The primary differences between the simulation and their experimental result are the sharper peaks and negative pressure in the simulation. The reason why the experimental results have a smooth curve is due to the noise and averaging method they employed. They sent 79 signals and received 79 pressure responses which contain some noise, and then used an averaging method to reduce the noise. Since the simulation does not have noise, their averaging process cannot be replicated directly. The negative pressure in the simulation result follows because a true sinusoidal chirp as shown in Figure 9 was used (not a DC-offset chirp), which implies a negative intensity illumination in the simulations. However, the salient feature of both simulations and experimental results match – that is both theory and experiment indicate that only the edges of the absorber are detected, rather than the full absorber profile, which is in keeping with the frequency sweep area being too high to sweep over the full absorber bandwidth.

7 Summary and Conclusions

7.1 Thesis overview

In this thesis, photoacoustic imaging for biomedical applications was introduced and briefly reviewed. Both pulsed and continuous wave photoacoustics have been used. Much theoretical and experimental research has been done to date on the pulsed laser photoacoustic modality. Recently, researchers have become more interested in the continuous wave laser excitation photoacoustic modality, especially in using a linear frequency modulated sinusoidal laser chirp, because of the benefits accorded by pulse compression signal processing methods and the cheap and compact laser sources that can be used with a continuous wave approach. However, to date the studies on linear frequency modulated sinusoidal laser chirp photoacoustics have not provided any understanding of how the chirp parameters can affect the corresponding response signal and SNR.

In order to achieve the goal of acquiring a photoacoustic signal which carries acceptable absorber profilometric information (resolution), using a linear frequency modulated sinusoidal laser chirp, mathematical expressions of the pressure response signal obtained from square and exponential decay absorbers after filtering with a receiver-filter were developed in this thesis. Subsequently, mathematical expressions of SNR for a bandlimited absorber and a square absorber were also developed.

The simulations in Chapter 5 gave a clear pattern of how the chirp parameters affect the corresponding photoacoustic signal. Three key parameters of the chirp were identified as important in obtaining a better resolution. The longer chirp duration will give a better SNR but does not affect resolution much. Furthermore, chirp duration cannot be increased too much because of safety limitations in application to in-vivo imaging. The chirp bandwidth is a critical controlling parameter for both resolution

and SNR. A larger chirp bandwidth implies a shorter effective pulse duration after pulse compression, so a better resolution can be obtained. However, a larger bandwidth will result in a lower SNR. The chirp bandwidth needs to be adjusted to a value appropriate for obtaining an acceptable resolution but not losing too much SNR in the process. In order to obtain a better resolution, the bandwidth of chirp is not the only parameter that needs to be considered. It is important to ensure that the chirp is sweeping the right range in frequency where most of the absorber energy is concentrated. The chirp center frequency is the parameter that controls the sweeping position in the frequency domain.

Finally, the chirp parameters from Mandelis and Telenkov's paper [19] were used in simulations and results similar to their experimental results were obtained. Their two-peak experimental pressure response result may be explained by the chirp sweep being in the wrong place, or in other words, chirp center frequency was not well chosen and did not cover the bandwidth where most of the absorber energy was located.

7.2 Contributions of the thesis

In this thesis, the following contributions were made:

1. Two different types of absorber were considered and their corresponding mathematical photoacoustic pressure response signals obtained after the implementation of a receiver-filter were derived.

2. Mathematical expressions of the SNR for pulse-compressed photoacoustic signals obtained from two different types of absorber were developed.

3. Several simulations were performed to test the chirp parameters' effects on

corresponding photoacoustic signals. The simulation results showed very clear trends for signal resolution and SNR when the parameters were changed.

4. Guidelines of how to choose the parameters of the chirp in order to obtain a photoacoustic signal with acceptable absorber profilometric information and better SNR were proposed.

5. A simulation using the chirp parameters from Mandelis and Telenkov [19] was performed and compared with their experimental results. The comparison showed that the guidelines developed in this thesis for choosing chirp parameters predict a similar result as to that obtained from their experimental results.

7.3 Future work

Some examples of future research directions based the work developed in this thesis are as follows:

1. In this thesis, only linear frequency modulated sinusoidal chirps were used as an illumination source. The guideline on choosing chirp parameters only applies for this specific kind of chirp. Future work may need to be done on other types of chirps, such as square wave chirp or a train of chirped pulses.

2. In this thesis, only two simple kinds of absorbers were analyzed. The closed form expression of the photoacoustic signal for other kinds of absorbers may need to be found in future work.

3. In future studies, further experimental testing may better prove the theory proposed in this thesis.

References

[1] A. G. Bell, “The Production of Sound by Radiant Energy,” *Science*, vol. 2, no. 48, pp. 242–253, 1881.

[2] A. A. Oraevsky *et al.*, “Laser optoacoustic imaging of the breast: detection of cancer angiogenesis,” 1999, vol. 3597, pp. 352–363.

[3] V. G. Andreev *et al.*, “Optoacoustic tomography of breast cancer with arc-array transducer,” presented at the Biomedical Optoacoustics, 2000, vol. 3916, pp. 36–48.

[4] C. Li and L. V. Wang, “Photoacoustic tomography and sensing in biomedicine,” *Phys. Med. Biol.*, vol. 54, no. 19, pp. R59–R97, 2009.

[5] R. A. Kruger, D. R. Reinecke, and G. A. Kruger, “Thermoacoustic computed tomography–technical considerations,” *Med. Phys.*, vol. 26, no. 9, pp. 1832–1837, Sep. 1999.

[6] R. A. Kruger, K. K. Kopecky, A. M. Aisen, D. R. Reinecke, G. A. Kruger, and W. L. Kiser, “Thermoacoustic CT with Radio Waves: A Medical Imaging Paradigm,” *Radiology*, vol. 211, no. 1, pp. 275–278, Apr. 1999.

[7] G. Ku and L. V. Wang, “Scanning thermoacoustic tomography in biological tissue,” *Med. Phys.*, vol. 27, no. 5, pp. 1195–1202, May 2000.

[8] M. Xu and L. V. Wang, “Time-domain reconstruction for thermoacoustic tomography in a spherical geometry,” *Med. Imaging IEEE Trans. On*, vol. 21, no. 7, pp. 814–822, 2002.

[9] M. Xu, Y. Xu, and L. V. Wang, “Time-domain reconstruction algorithms and numerical simulations for thermoacoustic tomography in various geometries,” *IEEE Trans. Biomed. Eng.*, vol. 50, no. 9, pp. 1086–1099, Sep. 2003.

[10] A. A. Karabutov, N. B. Podymova, and V. S. Letokhov, “Time-resolved optoacoustic measurement of absorption of light by inhomogeneous media,” *Appl. Opt.*, vol. 34, no. 9, pp. 1484–1487, Mar. 1995.

[11] Y. Fan, A. Mandelis, G. Spirou, I. A. Vitkin, and W. M. Whelan, “Laser

photothermoacoustic heterodyned lock-in depth profilometry in turbid tissue phantoms," *Phys. Rev. E*, vol. 72, no. 5, p. 051908, Nov. 2005.

[12] S. A. Telenkov and A. Mandelis, "Photothermoacoustic imaging of biological tissues: maximum depth characterization comparison of time and frequency-domain measurements," *J. Biomed. Opt.*, vol. 14, no. 4, pp. 044025-044025-12, 2009.

[13] S. Telenkov and A. Mandelis, "Signal-to-noise analysis of biomedical photoacoustic measurements in time and frequency domains," *Rev. Sci. Instrum.*, vol. 81, no. 12, p. 124901, Dec. 2010.

[14] B. Lashkari and A. Mandelis, "Linear frequency modulation photoacoustic radar: Optimal bandwidth and signal-to-noise ratio for frequency-domain imaging of turbid media," *J. Acoust. Soc. Am.*, vol. 130, no. 3, pp. 1313–1324, Sep. 2011.

[15] B. Lashkari and A. Mandelis, "Comparison between pulsed laser and frequency-domain photoacoustic modalities: Signal-to-noise ratio, contrast, resolution, and maximum depth detectivity," *Rev. Sci. Instrum.*, vol. 82, no. 9, p. 094903, Sep. 2011.

[16] B. Lashkari and A. Mandelis, "Photoacoustic radar imaging signal-to-noise ratio, contrast, and resolution enhancement using nonlinear chirp modulation," *Opt. Lett.*, vol. 35, no. 10, pp. 1623–1625, May 2010.

[17] Y. Fan, A. Mandelis, G. Spirou, I. A. Vitkin, and W. M. Whelan, "Three-dimensional photothermoacoustic depth-profilometric imaging by use of a linear frequency sweep lock-in heterodyne method," 2004, vol. 5320, pp. 113–127.

[18] S. Telenkov, A. Mandelis, B. Lashkari, and M. Forcht, "Frequency-domain photothermoacoustics: Alternative imaging modality of biological tissues," *J. Appl. Phys.*, vol. 105, no. 10, p. 102029, May 2009.

[19] S. A. Telenkov, R. Alwi, and A. Mandelis, "Photoacoustic correlation signal-to-noise ratio enhancement by coherent averaging and optical waveform optimization," *Rev. Sci. Instrum.*, vol. 84, no. 10, p. 104907, Oct. 2013.

[20] A. G. Bell, "The photophone," *J. Frankl. Inst.*, vol. 110, no. 4, pp. 237–248,

1880.

[21] D. Betteridge and P. J. Meylor, “Analytical Aspects of Photoacoustic Spectroscopy,” *C R C Crit. Rev. Anal. Chem.*, vol. 14, no. 4, pp. 267–295, Jan. 1984.

[22] “Ultralow Gas Concentration Infrared Absorption Spectroscopy,” *J. Appl. Phys.*, vol. 42, no. 7, pp. 2934–2943, Jun. 1971.

[23] T. H. Maugh, “Photoacoustic Spectroscopy: New Uses for an Old Technique,” *Science*, vol. 188, no. 4183, pp. 38–39, Apr. 1975.

[24] J. R. Klauder, A. C. Price, S. Darlington, and W. J. Albersheim, “The Theory and Design of Chirp Radars,” *Bell Syst. Tech. J.*, vol. 39, no. 4, pp. 745–808, 1960.

[25] B. R. Friedman, J. P. Jones, G. Chavez-Munoz, A. P. Salmon, and C. R. B. Merritt, “Principles of MRI,” 1989.

[26] P. N. T. Wells, “Ultrasonic imaging of the human body,” *Rep. Prog. Phys.*, vol. 62, no. 5, pp. 671–722, 1999.

[27] K. Suzuki, Y. Yamashita, K. Ohta, M. Kaneko, M. Yoshida, and B. Chance, “Quantitative measurement of optical parameters in normal breasts using time-resolved spectroscopy: in vivo results of 30 Japanese women,” *J. Biomed. Opt.*, vol. 1, no. 3, p. 330, 1996.

[28] T. Liu, J. Wang, G. I. Petrov, V. V. Yakovlev, and H. F. Zhang, “Photoacoustic generation by multiple picosecond pulse excitation,” *Med. Phys.*, vol. 37, no. 4, pp. 1518–1521, Apr. 2010.

[29] D.-K. Yao and L. V. Wang, “Measurement of Grüneisen parameter of tissue by photoacoustic spectrometry,” 2013, vol. 8581, pp. 858138-858138–5.

[30] X. Wang, D. L. Chamberland, and G. Xi, “Noninvasive reflection mode photoacoustic imaging through infant skull toward imaging of neonatal brains,” *J. Neurosci. Methods*, vol. 168, no. 2, pp. 412–421, Mar. 2008.

[31] G. Ku and L. V. Wang, “Scanning microwave-induced thermoacoustic tomography: Signal, resolution, and contrast,” *Med. Phys.*, vol. 28, no. 1, pp. 4–10, Jan. 2001.

[32] G. Xu, I. A. Dar, C. Tao, X. Liu, C. X. Deng, and X. Wang, “Photoacoustic

spectrum analysis for microstructure characterization in biological tissue: A feasibility study," *Appl. Phys. Lett.*, vol. 101, no. 22, p. 221102, Nov. 2012.

[33] D. Brandwood, *Fourier Transforms in Radar and Signal Processing*. Norwood, Boston: Artech House, 2003.

[34] M. Soumekh, *Synthetic aperture radar signal processing with MATLAB algorithms*. New York: JWiley, 1999.

[35] D. C. Schleher, *MTI and pulsed doppler radar*. Boston: Artech House, 1991.

[36] H. Schmitt, "Pulse Compression Radar System Analysis," *Microw. J. Int. Ed Dedham*, vol. 59, no. 1, p. 106,108,110,112, Jan. 2016.

[37] E. N. Fowle, D. R. Carey, R. E. Vander Schuur, and R. C. Yost, "A pulse compression system employing a linear FM Gaussian signal," *Proc. IEEE*, vol. 51, no. 2, pp. 304–312, 1963.

[38] B. Lashkari and A. Mandelis, "Features of the Frequency- and Time-Domain Photoacoustic Modalities," *Int. J. Thermophys.*, vol. 34, no. 8–9, pp. 1398–1404, 2013.

[39] N. Baddour and A. Mandelis, "The Effect of Acoustic Impedance on Subsurface Absorber Geometry Reconstruction using 1D Frequency-Domain Photoacoustics," *Photoacoustics*, vol. 3, no. 4, pp. 132–142, Dec. 2015.

[40] S. A. Telenkov and A. Mandelis, "Fourier-domain biophotoacoustic subsurface depth selective amplitude and phase imaging of turbid phantoms and biological tissue," *J. Biomed. Opt.*, vol. 11, no. 4, pp. 044006-044006-10, 2006.

[41] S. A. Telenkov and A. Mandelis, "Fourier-domain methodology for depth-selective photothermoacoustic imaging of tissue chromophores," *Eur. Phys. J. Spec. Top.*, vol. 153, no. 1, pp. 443–448, Jan. 2008.

[42] S. P. Davis, *Fourier Transform Spectrometry*. Burlington, San Diego: Academic Press, 2001.

[43] V. Saptari, *Fourier transform spectroscopy instrumentation engineering*. Bellingham, Wash, Bellingham, Wash. (1000 20th St. Bellingham WA 98225-6705 USA): SPIE, 2004.

[44] A. Papoulis, *Signal analysis*. New York: McGraw-Hill, 1977.

[45] GeraldJ Diebold, “Photoacoustic Monopole Radiation,” in *Photoacoustic Imaging and Spectroscopy*, 0 vols., CRC Press, 2009, pp. 3–17.

[46] “Multidimensional wave field signal theory: Mathematical foundations,” *AIP Adv.*, vol. 1, no. 2, p. 022120, May 2011.

[47] N. Baddour, “Multidimensional wave field signal theory: Mathematical foundations,” *AIP Adv.*, vol. 1, no. 2, p. 022120, 2011.

[48] P. M. Woodward, *Probability and information theory: with applications to radar.* New York, London: McGraw-Hill, Pergamon Press, 1955.

[49] J. R. Klauder, A. C. Price, S. Darlington, and W. J. Albersheim, “The Theory and Design of Chirp Radars,” *Bell Syst. Tech. J.*, vol. 39, no. 4, pp. 745–808, Jul. 1960.

[50] B. Lashkari, “Photoacoustic Imaging Using Chirp Technique: Comparison with Pulsed Laser Photoacoustics,” Ph.D dissertation, University of Toronto, 2011.

[51] M. Xu and L. V. Wang, “Photoacoustic imaging in biomedicine,” *Rev. Sci. Instrum.*, vol. 77, no. 4, 2006.

Appendix - Shifted Chirp Autocorrelation

The autocorrelation of a shifted cosine chirp is

$$R_{II}^{shifted}(t)=\begin{cases}0 & T<t \\ R_{II\_1}^{shifted}(t) & 0<t<T \\ R_{II\_2}^{shifted}(t) & -T<t<0 \\ 0 & t<-T\end{cases} \tag{A.1}$$

with $R_{II\_i}^{shifted}(t)$ shown as

$$
\begin{aligned}
R_{II\_1}^{shifted}(t) = \frac{1}{4\pi K^{\frac{3}{2}} t}\Big[& -4\sqrt{K}\cos\left(\pi f_0 t\right)^2 \sin\left(\pi K t^2\right)\cos\left(\pi K T t\right) \\
& + 4\sqrt{K}\cos\left(\pi f_0 t\right)^2 \cos\left(\pi K t^2\right)\sin\left(\pi K T t\right) \\
& + 4\pi K^{\frac{3}{2}} t + 2\sqrt{K}\cos\left(\pi K T t\right)\sin\left(\pi K t^2\right) \\
& - 2\sqrt{K}\sin\left(\pi K T t\right)\cos\left(\pi K t^2\right) - 4\pi K^{\frac{3}{2}} t^2 \\
& + 2\pi K\sqrt{2}\cos\left(\frac{\pi f_0^2}{K}\right) FresnelC\left(\frac{\sqrt{2}}{2}\frac{KT - 2Kt - 2f_0}{\sqrt{K}}\right) t \\
& + 2\pi K\cos\left(\frac{1}{2}\pi K t^2\right)\cos\left(\frac{\pi f_0^2}{K}\right)^2 FresnelC\left(\frac{KT - Kt - 2f_0}{\sqrt{K}}\right) t \\
& - 2\pi K\sin\left(\frac{1}{2}\pi K t^2\right)\cos\left(\frac{\pi f_0^2}{K}\right)^2 FresnelS\left(\frac{KT - Kt - 2f_0}{\sqrt{K}}\right) t \\
& + 2\pi K t\cos\left(\frac{1}{2}\pi K t^2\right)\cos\left(\frac{\pi f_0^2}{K}\right)^2 FresnelC\left(\frac{KT - Kt + 2f_0}{\sqrt{K}}\right) \\
& - 2\pi K\sin\left(\frac{1}{2}\pi K t^2\right)\cos\left(\frac{\pi f_0^2}{K}\right)^2 FresnelS\left(\frac{KT - Kt + 2f_0}{\sqrt{K}}\right) t \\
& + 2\sqrt{2}\pi K\sin\left(\frac{\pi f_0^2}{K}\right)^2 FresnelS\left(\frac{\sqrt{2}}{2}\frac{KT - 2Kt + 2f_0}{\sqrt{K}}\right) t \\
& + 2\pi\sqrt{2}K\cos\left(\frac{\pi f_0^2}{K}\right)^2 FresnelC\left(\frac{\sqrt{2}}{2}\frac{KT - 2Kt + 2f_0}{\sqrt{K}}\right) t \\
& + 2\pi\sqrt{2}K\cos\left(\frac{\pi f_0^2}{K}\right)^2 FresnelC\left(\frac{\sqrt{2}}{2}\frac{KT + 2f_0}{\sqrt{K}}\right) t \\
& + 2\pi\sqrt{2}K\sin\left(\frac{\pi f_0^2}{K}\right)^2 FresnelS\left(\frac{\sqrt{2}}{2}\frac{KT + 2f_0}{\sqrt{K}}\right) t \\
& + 2\pi\sqrt{2}K\sin\left(\frac{\pi f_0^2}{K}\right)^2 FresnelS\left(\frac{\sqrt{2}}{2}\frac{KT - 2f_0}{\sqrt{K}}\right) t \\
& - \pi K\cos\left(\frac{1}{2}\pi K t^2\right) FresnelC\left(\frac{KT - Kt - 2f_0}{\sqrt{K}}\right) t \\
& + \pi K\sin\left(\frac{1}{2}\pi K t^2\right) FresnelS\left(\frac{KT - Kt - 2f_0}{\sqrt{K}}\right) t \\
& - \pi K\cos\left(\frac{1}{2}\pi K t^2\right) FresnelC\left(\frac{KT - Kt + 2f_0}{\sqrt{K}}\right) t \\
& + \pi K\sin\left(\frac{1}{2}\pi K t^2\right) FresnelS\left(\frac{KT - Kt + 2f_0}{\sqrt{K}}\right) t \Big]
\end{aligned}
\tag{A.2}
$$

$$
\begin{aligned}
R_{II\_2}^{shifted}(t) = \frac{1}{4\pi K^{\frac{3}{2}} t}\Big[& 4\sqrt{K}\cos(\pi f_0 t)^2 \sin(\pi K t^2)\cos(\pi K T t) \\
& + 4\sqrt{K}\cos(\pi f_0 t)^2 \cos(\pi K t^2)\sin(\pi K T t) \\
& + 4T\pi K^{\frac{3}{2}} t - 2\sqrt{K}\cos(\pi K T t)\sin(\pi K t^2) \\
& - 2\sqrt{K}\sin(\pi K T t)\cos(\pi K t^2) - 4\pi K^{\frac{3}{2}} t^2 \\
& + 2\pi K\sqrt{2}\sin\left(\frac{\pi f_0^2}{K}\right) FresnelC\left(\frac{\sqrt{2}}{2}\frac{KT+2Kt+2f_0}{\sqrt{K}}\right) t \\
& + 2\pi K\sin\left(\frac{1}{2}\pi K t^2\right)\sin\left(\frac{\pi f_0^2}{K}\right)\cos\left(\frac{\pi f_0^2}{K}\right) FresnelC\left(\frac{KT+Kt-2f_0}{\sqrt{K}}\right) t \\
& + 2\pi K\cos\left(\frac{1}{2}\pi K t^2\right)\sin\left(\frac{\pi f_0^2}{K}\right)\cos\left(\frac{\pi f_0^2}{K}\right) FresnelS\left(\frac{KT+Kt-2f_0}{\sqrt{K}}\right) t \\
& + 2\pi K t\sin\left(\frac{1}{2}\pi K t^2\right)\sin\left(\frac{\pi f_0^2}{K}\right)\cos\left(\frac{\pi f_0^2}{K}\right) FresnelC\left(\frac{KT+Kt+2f_0}{\sqrt{K}}\right) \\
& - 2\pi K\cos\left(\frac{1}{2}\pi K t^2\right)\sin\left(\frac{\pi f_0^2}{K}\right)\cos\left(\frac{\pi f_0^2}{K}\right) FresnelS\left(\frac{KT+Kt+2f_0}{\sqrt{K}}\right) t \\
& - 2\sqrt{2}\pi K\sin\left(\frac{1}{2}\pi K t^2\right)\cos\left(\frac{\pi f_0^2}{K}\right)^2 FresnelS\left(\frac{\sqrt{2}}{2}\frac{KT+2Kt+2f_0}{\sqrt{K}}\right) t \\
& + 2\pi\sqrt{2}K\cos\left(\frac{\pi f_0^2}{K}\right) FresnelC\left(\frac{\sqrt{2}}{2}\frac{KT+2Kt+2f_0}{\sqrt{K}}\right) t \\
& + 2\pi\sqrt{2}K\cos\left(\frac{\pi f_0^2}{K}\right) FresnelC\left(\frac{\sqrt{2}}{2}\frac{KT+2f_0}{\sqrt{K}}\right) t \\
& + 2\pi\sqrt{2}K\sin\left(\frac{\pi f_0^2}{K}\right) FresnelS\left(\frac{\sqrt{2}}{2}\frac{KT-2f_0}{\sqrt{K}}\right) t \\
& + 2\pi\sqrt{2}K\cos\left(\frac{\pi f_0^2}{K}\right) FresnelC\left(\frac{\sqrt{2}}{2}\frac{KT-2f_0}{\sqrt{K}}\right) t \\
& - \pi K\cos\left(\frac{1}{2}\pi K t^2\right) FresnelC\left(\frac{KT+Kt+2f_0}{\sqrt{K}}\right) t \\
& + \pi K\sin\left(\frac{1}{2}\pi K t^2\right) FresnelS\left(\frac{KT+Kt+2f_0}{\sqrt{K}}\right) t \\
& - \pi K\cos\left(\frac{1}{2}\pi K t^2\right) FresnelC\left(\frac{KT+Kt-2f_0}{\sqrt{K}}\right) t \\
& + \pi K\sin\left(\frac{1}{2}\pi K t^2\right) FresnelS\left(\frac{KT+Kt-2f_0}{\sqrt{K}}\right) t \Big]
\end{aligned}
$$

(A.3)